

Assessing the Impacts of Natural Hazards on Road Infrastructure Using Multi-Source Geoinformation

Janine Natalie Florath

Doctoral Thesis 2024

Assessing the Impacts of Natural Hazards on Road Infrastructure Using Multi-Source Geoinformation

Zur Erlangung des akademischen Grades einer

DOKTORIN DER INGENIEURWISSENSCHAFTEN (Dr.-Ing.)

von der KIT-Fakultät für
Bauingenieur-, Geo- und Umweltwissenschaften
des Karlsruher Instituts für Technologie (KIT)

genehmigte

DISSERTATION

von

Janine Natalie Florath

aus Freiburg i. Br.

Tag der mündlichen Prüfung:	20.02.2024
Referentin:	PD Dr. rer. nat. Sina Keller Institute of Photogrammetry and Remote Sensing Karlsruhe Institute of Technology
Korreferent:	Prof. Jocelyn Chanussot Inria, CNRS, Grenoble INP, LJK Université Grenoble Alpes
Korreferent:	Prof. Dr.-Ing. Stefan Hinz Institute of Photogrammetry and Remote Sensing Karlsruhe Institute of Technology

Karlsruhe (2024)

Abstract

Natural hazards present a significant risk to road infrastructure, which constitutes a fundamental component of the transportation infrastructure. Especially during emergency situations, society heavily relies on the functionality of its road infrastructure to facilitate evacuation and access to emergency facilities. Several existing studies conduct road network accessibility analysis during natural hazards. However, the transferability is often not given, as these studies rely on specified data curated by the authors oftentimes in commercial, non-freely accessible transport modelling software. These data are available for selected case studies only, specific hazard types only or specific road network types. Therefore, there remains a gap for a complete comprehensive framework, which is complete from the acquisition of openly accessible data about hazard impacts to road network analysis and is designed to be easily applicable for any hazard and road network type. In this thesis, a versatile, generic framework designed to analyze accessibility within road networks during natural hazard scenarios is introduced and applied to various case study hazards.

The first module of the framework focuses on assessing the impact of natural hazards. It relies on openly and cost-effective accessible geoinformation data, provided by high-resolution Remote Sensing (RS) data and citizen science through Volunteered Geographic Information (VGI) data, often in near real-time. The determination of natural hazards' impacts on road infrastructure are separated into two major impact investigations, hazard impact zone estimation and direct road impact extraction. The results indicate that VGI and RS data are valuable data sources for hazard impact zone estimation. Furthermore, using VGI text information, impacted roads can be identified. The combination of RS and VGI data enhances the accuracy and availability of hazard impact determination in near-real time.

The second module conducts road network analysis based on freely available Open Street Map (OSM) data, differentiating between intact and degraded road networks. The degraded road network is constructed using the directly impacted roads and the hazard impact zones determined in the first module. Four accessibility measures are calculated, including two well-established road network analysis measures, betweenness centrality and closeness centrality, an adapted free-flow assumption index, and a novel alternative routing assumption measure that considers congestion scenarios. The results indicate that a network accessibility based on the openly accessible network data (OSM) and the hazard impact information based on openly accessible geoinformation data (VGI and RS)

is feasible. Furthermore, all investigated accessibility measures are valuable for network analysis and complement each other focusing on different network attributes.

This thesis showcases various exemplary applications for different hazard types like floods and wildfires in a variety of regions like the United States of America (US) and France for the components of the framework. This demonstrates its versatility and effectiveness in diverse environmental contexts. The complete framework composed of all components is applied on a case study hazard of the Bobcat wildfire in the US to demonstrate their transferability. In conclusion, this study successfully addresses the challenges of developing a generic, complete framework from hazard impact determination to road network analysis independently of scale and characteristics of hazards and road network types.

Kurzfassung

Naturgefahren können ein erhebliches Risiko für Straßennetze darstellen, die ein wichtiger Bestandteil der Verkehrsinfrastruktur sind. Vor allem in Notsituationen ist die Gesellschaft in hohem Maße auf die Funktionsfähigkeit der Straßeninfrastruktur angewiesen, um Evakuierungen und den Zugang zu Notfalleinrichtungen zu gewährleisten. In einigen Studien wird die Erreichbarkeit des Straßennetzes während Naturgefahren analysiert. Die Übertragbarkeit auf andere Gegebenheiten ist jedoch oft nicht möglich, da sich die Studien auf Daten stützen, die nur für bestimmte Arten von Gefahren oder bestimmte Straßennetze (z. B. nur städtische Netze) verfügbar sind. Daher besteht nach wie vor eine Lücke für ein komplettes generisches Rahmenkonzept, das den Einfluss von Naturgefahren auf die Straßeninfrastruktur abschätzen und bewerten kann. Dieser Ansatz muss so konzipiert sein, dass er für jede Art von Naturgefahr und jeden Straßennetzwerktyp anwendbar ist. In dieser Arbeit wird ein generisches Konzept zur Analyse der Erreichbarkeit von Straßennetzen bei Naturkatastrophen vorgestellt.

Das erste Modul des Ansatzes konzentriert sich auf die Auswirkungen von Naturgefahren. Es stützt sich auf offen und kostengünstig zugängliche Geoinformationsdaten, die nahezu in Echtzeit verfügbar sind. Diese sind durch hochauflösende Fernerkundungs (RS)-Daten und Citizen Science-Daten, die durch Volunteered Geographic Information (VGI)-Daten bereitgestellt werden. Die Abschätzung der Auswirkungen von Naturgefahren auf die Straßeninfrastruktur wird in zwei Untersuchungen unterteilt: die Abschätzung der Gefahrenzonen und die Analyse der direkten Auswirkungen auf Straßen. Die Ergebnisse zeigen, dass die RS- und VGI-Daten für die Abschätzung der Gefahrenzonen verwendbar sind. Außerdem sind die VGI-Textinformationen für die Identifizierung, der von der Naturgefahren betroffenen Straßen, verwendbar. Die Kombination von RS- und VGI-Daten verbessert die Genauigkeit und Verfügbarkeit der Gefahrenanalyse.

Das zweite Modul führt eine Straßennetzwerkanalyse auf der Grundlage frei verfügbarer Open Street Map (OSM)-Daten durch. Dabei wird zwischen intakten und beschädigten Straßennetzen unterschieden. Das von der Naturgefahr betroffene Straßennetz wird dabei aus dem intakten Netz konstruiert, indem Straßen entfernt werden, die im ersten Modul als beeinträchtigt oder möglicherweise beeinträchtigt identifiziert worden sind. Es werden vier Erreichbarkeitsmaße verwendet, darunter zwei bewährte Netzanalysemaße, die Betweenness Centrality und die Closeness Centrality, ein angepasster Index unter der Annahme freien Verkehrsflusses und ein neu eingeführtes Maß unter der Annahme von Stauszenarien und einer alternativen Streckenführung. Die Ergebnisse zeigen, dass eine Erreichbarkeitsanalyse auf der Grundlage von offen zugänglichen Straßennetzdaten

(OSM) und der Information über Gefahrenauswirkungen auf der Grundlage von offen zugänglichen Geoinformationsdaten (VGI und RS) machbar ist. Darüber hinaus sind alle untersuchten Zugänglichkeitsmaße für die Netzanalyse wertvoll.

In dieser Arbeit werden verschiedene Anwendungen, anhand von Beispielen, für unterschiedliche Arten von Gefahren, wie Überschwemmungen und Waldbrände, in mehreren Regionen, wie den USA und Frankreich, für die Teile des Konzepts vorgestellt. Dies dient dazu die Vielseitigkeit und Wirksamkeit in verschiedenen Bereichen zu demonstrieren. Das Gesamtkonzept mit all seinen Modulen und Komponenten wird auf die Fallstudie des Bobcat-Waldbrandes in den USA angewendet, um die Übertragbarkeit aller Komponenten zu zeigen. Insgesamt konnte diese Studie mit der Entwicklung eines generischen, modularen Gesamtkonzeptes von der Abschätzung der Gefahrenauswirkungen bis hin zur Straßennetzanalyse erfolgreich zur Risikofolgenabschätzung von Naturgefahren für die Straßeninfrastruktur beitragen.

Contents

1	Introduction	1
1.1	Motivation	1
1.2	Main Objective and Research Goals	2
1.3	Thesis Contributions and Outline	4
2	Introducing Heterogeneous Geoinformation Data and the Natural Hazard Scenario Selection	7
2.1	Introducing Geoinformation Data	8
2.1.1	Geoinformation Data for Natural Hazard Impact Determination	9
2.1.2	Geoinformation Data for Network Accessibility Assessment	19
2.1.3	Synthesis on RS and VGI Data and Integration in Framework	20
2.2	Natural Hazard Scenario Selection	21
3	Natural Hazard Impact Determination with Geoinformation Data	23
3.1	Natural Hazard Impact Zone Estimation with Remote Sensing Data	25
3.1.1	Introduction	25
3.1.2	Data	27
3.1.3	Methodology	30
3.1.4	Results	37
3.1.5	Discussion	40
3.1.6	Conclusion and Integration in Framework	41
3.2	Natural Hazard Impact Zone Estimation with Volunteered Geographic Information Data	42
3.2.1	Introduction	43
3.2.2	Data	46
3.2.3	Methodology	51
3.2.4	Results	58
3.2.5	Discussion	63
3.2.6	Conclusion and Integration in Framework	67
3.3	Road Impact Extraction from Volunteered Geographic Information Data	68
3.3.1	Introduction	68
3.3.2	Data	69
3.3.3	Methodology	70
3.3.4	Results	71
3.3.5	Discussion	72

3.3.6	Conclusion and Integration in Framework	73
3.4	Synthesis on the First Module	74
4	Road Network Accessibility Assessment during Natural Hazards	77
4.1	Introduction	78
4.2	Data	80
4.3	Methodology	81
4.3.1	Road Network Basics	81
4.3.2	Degraded Road Network Construction based on Hazard-Induced Impact	82
4.3.3	Road Network Accessibility	83
4.4	Results	86
4.5	Discussion	90
4.6	Conclusion and Integration in Framework	94
4.7	Synthesis on the Second Module	94
5	Complete Framework: Application to Bobcat Wildfire	97
5.1	Application Scenario	97
5.2	Module 1	99
5.2.1	Natural Hazard Impact Zone Estimation with Remote Sensing Data	99
5.2.2	Natural Hazard Impact Zone Estimation with Volunteered Geo- graphic Information Data	100
5.2.3	Road Impact Extraction from Volunteered Geographic Information Data	101
5.3	Module 2	102
5.3.1	Road Network Data	103
5.3.2	Degraded Road Network Construction based on Hazard-Induced Impact	103
5.3.3	Road Network Accessibility Analysis	105
5.4	Discussion	108
5.4.1	Applicability of Framework on Bobcat Fire	108
5.4.2	Transferability of Framework	110
5.5	Conclusion	111
6	Synopsis and Outlook	113
6.1	Synoptical Discussion and Conclusion	113
6.2	Outlook	116
	Bibliography	119
	List of Figures	139
	List of Tables	143

List of Abbreviations	145
A Appendix	149
A Supplementary Material of Natural Hazard Impact Zone Estimation with Remote Sensing Data	149
A.1 Hyperparameters	149
A.2 Confusion Matrices	149
B Supplementary Material of Natural Hazard Impact Zone Estimation with Volunteered Geographic Information Data - Moving Hazards	151
B.1 Hyperparameters	151
B.2 Evaluation Metrics	151
C Supplementary Material of Network Accessibility Assessment during Natural Hazards	152
C.1 Result Presentation Rationale	152

Introduction

This chapter includes elements from

[1] J. Florath, J. Chanussot, and S. Keller. “Road Accessibility during Natural Hazards Based on Volunteered Geographic Information Data and Network Analysis”. In: *ISPRS International Journal of Geo-Information* 13.4 (2024), p. 107

marked with a [green line](#).

1.1 Motivation

Recently, there has been an increase in the frequency and intensity of hydrological and meteorological natural hazard events [2]. Their numbers have tripled worldwide in the period from 2005 to 2014 in comparison to the period from 1975 to 1984 [3] based on the Emergency Events Database (EM-DAT [4]) data. Such natural hazards pose a significant risk to the physical and socio-economic well-being of humans, as well as to natural ecosystems [5, 6]. Critical infrastructures, which comprise multi-level technical and organizational structures necessary to maintain social functions, are also at risk from natural hazards [7]. Their failure can have severe consequences for human life. The road infrastructure is one of the most crucial parts of the transportation network and is frequently damaged during natural hazards (e.g., [8, 9]). This damage has various impacts, including restricted access to emergency facilities, delayed emergency management response, but also preventing evacuations.

Considering the increasing frequency and intensity of natural hazards and their substantial impact on critical infrastructures, particularly the road network, many previous studies employed detailed road network analysis in natural hazard contexts (e.g., [8, 9, 10, 11]). However, these studies usually concentrate on a single case study hazard in a single location and have limited applicability to other contexts. As it is especially difficult to access complex degraded road datasets after a natural hazard, proposed advanced models or simulations are often not transferable. Consequently, there is a lack of a generic framework that can tackle the challenge of restricted global data availability and directly analyze the impact of natural hazards on critical road infrastructure. To deal with this identified gap,

a generic framework which is complete from the impacted road data analysis during the hazard to the network analysis is introduced.

In such a framework, the effects of the natural hazard on the road infrastructure need to be investigated first (e.g., [12, 13]). Initially, the geolocation and extent of the hazard in question need to be determined. Subsequently, the evaluation of the operability and functionality of road infrastructure during a natural hazard can be conducted. Valuable information regarding potential impacts on roads can be gathered by considering natural hazard impact areas. When these hazard areas overlap with the road network, it suggests that the roads are likely to be affected in some way and might suffer at least implicit impacts. Once the impact of the hazard on the road infrastructure is elaborated, the road accessibility and therefore its functionality can be assessed with a road network analysis. A road network analysis can be carried out before and during/after a hazard to estimate the hazard impact on it as a change in accessibility of the respective road network. The construction of a generic framework, applicable to a variety of hazards in different scenarios, is facilitated by the use of only freely and openly available geoinformation data [14, 15, 16] for both hazard impact analysis and network analysis.

1.2 Main Objective and Research Goals

A complete framework from the impacted road data extraction during the hazard to the network analysis is constructed. In a first step, the assessment of natural hazards' locations and impacts is necessary. Estimating hazard locations for various hazards in different scenarios benefits from the analysis of geoinformation data that play a crucial role for the development of spatial models and risk assessments. A complete concept that accumulates the information gain from various geoinformation data for the determination of natural hazards' impacts has not been developed yet. Various geoinformation data can be used for natural hazard analysis [17, 18]. RS imagery and VGI data are oftentimes open, free data with global coverage [19, 20, 21].

Although there exist many data sources in the VGI category, this work focuses on Twitter (now X) data, as it proves to be a valuable source of real-time information (e.g., [22, 23, 24]). RS imagery can provide high spatial resolution data for detailed hazard mapping, while VGI data contributes real-time, on-the-ground insights on the hazard location. Furthermore, VGI text information can be used to extract road specific information, which can help to analyze impacts on critical road infrastructure directly [1, 25]. However, disadvantages of both data sources like limited temporal resolution in RS imagery and lack of VGI data validation could limit their suitability for one or the other hazard scenario and need to be carefully investigated [26, 27]. Therefore, techniques are required that improve the information extraction for hazards from both data sources for hazard impact determination purposes. Only few studies combine the use of different geoinformation

data (e.g., [28, 29, 30]) for natural hazard analysis. Employing such data to evaluate the influence of hazard impacts on the road network, as a basis for a road network analysis, is still missing.

The assessment of critical road infrastructure during natural hazards is an interdisciplinary research domain including various methodologies (e.g., [31, 32, 33]), traffic models (e.g., [34]), and advanced simulations (e.g., [35]). Most approaches concentrate on specific case studies (e.g., [36, 37]), often in exclusively urban or rural contexts and frequently lacking broad applicability. Moreover, many previously reported approaches lack transferability and universal usability. Additionally, the advantages of the availability of global data has been often overlooked. Consequently, there remains a gap for a generic framework that comprises the extraction of hazard-related road information to analyze the immediate impacts on road infrastructure. To overcome the mentioned gaps, the main objective of this thesis is to develop a generic, multiscale framework to assess critical road infrastructure in a natural hazard context using various freely and openly available geoinformation data sources.

Two consecutive major research goals are identified on the basis of the above-identified gaps to develop a complete framework for hazard impact assessment on road networks:

Goal I: Natural Hazard Impact Determination with Multi-Source Geoinformation Data.

Goal II: Road Network Accessibility Assessment during Natural Hazards.

The developed framework comprises two independent modules (**Module I** and **Module II**), each addressing one of these specific research goal. The generic framework should be suitable to assess the hazard's impact on road networks for various hazard scenarios. However, this framework is designed with a specific focus on wildfire hazards as a selected overall application scenario. The decision to prioritize fire hazards within this framework is based on these hazards' potential to cause severe impacts on road infrastructure [38]. Furthermore, wildfire hazards are rarely analysed in related studies as a majority of investigations are centered around the impacts of flooding (e.g., [39]), landslides (e.g., [10]), earthquakes (e.g., [40]), or tropical cyclones (TCs) (e.g., [41]). In addition, the need to focus on one single hazard in depth is necessary as a variety of data and methods exist for hazard impact analysis and not all can be investigated for all hazards in the scope of this work. However, to illustrate the adaptability of the framework's developed components, specific application scenarios of TC and flood hazards are also examined.

1.3 Thesis Contributions and Outline

This dissertation is structured into six chapters. Figure 1.1 illustrates an overview of the structure.

Chapter 2 introduces the heterogeneous geoinformation data, that will be used as data sources for different approaches to achieve the two major research objectives of this thesis. Geoinformation data for the location and extent estimation of natural hazards vary much and are often neither accurately mapped nor available in near-real time [42, 26]. However, to implement a system that could be used for first responders or government officials to evaluate the situation, the near-real time information of the hazard is necessary to conduct a proper network analysis. RS and VGI data are selected as a valuable source for the task. Furthermore, this chapter introduces the hazards that are used throughout the thesis as application scenarios for developed methodologies. Various hazard scenarios are selected to demonstrate the complexities and necessities for the development of suitable frameworks to achieve the task of assessment of natural hazards' impacts on road infrastructure with multi-source geoinformation data.

Chapter 3 - Module I focuses on the first research goal; the natural hazard impact determination with multi-source geoinformation data. The determination of natural hazards' impacts on road infrastructure can be separated into two major impact investigations, hazard impact zone and direct impact extraction. The combination of hazard impact zones and directly extractable road impacts defines the total impact of the hazard on the road network. By identifying areas where hazard impact zones overlap with roadways, planners can anticipate the potential for direct and indirect impacts on the road infrastructure (e.g., [12, 10, 39]). For instance, a wildfire's proximity to roads might lead to road closures due to fire blocking the road directly or due to fallen trees or visibility issues indirectly. Furthermore, the direct effects of known hazard-induced road degradation can be evaluated (e.g., [40]). Accordingly, this section is split in three subsections: Frameworks for the natural hazard impact zone estimation with RS data (1) and VGI (2) data are developed. Furthermore, a road impact extraction framework from VGI data (3) is developed. Module I's established hazard impact knowledge serves as the basis for the subsequent module.

Chapter 4 - Module II addresses the second research goal by focusing on road network accessibility assessment during natural hazards' impacts on road infrastructure. Thereby, this module builds upon Module I and its extracted hazard impact (zones) by overlaying them with the road network to be investigated. During this process, roads of the network that intersect with the hazard impact zone are categorized as *degraded*. Road sections lying within the hazard impact zone may be indirectly affected by the hazard, directly affected at a later time, or directly affected even though information about direct impact is not available. Furthermore, roads in the network that experience direct impacts as extracted in Module I are categorized as *degraded*, too. This resulting *degraded road*

network then becomes the basis for conducting a network accessibility analysis on the intact and degraded road network. The change in network accessibility by the hazard's influence is evaluated.

In [Chapter 5](#) the developed methodology comprising of [Module I](#) and [Module II](#) for the assessment of natural hazards' impacts on road infrastructure is applied exemplary for the scenario of the Bobcat wildfire hazard. This application demonstrates the adequacy of the two combined modules as a complete and generic framework to assess natural hazards' impacts on road infrastructure. Furthermore, this demonstration also provides valuable insights into potential practical implementation of this framework.

The final section, [Chapter 6](#), provides a comprehensive summary and conclusions of the entire dissertation together with an outlook for future improvements.

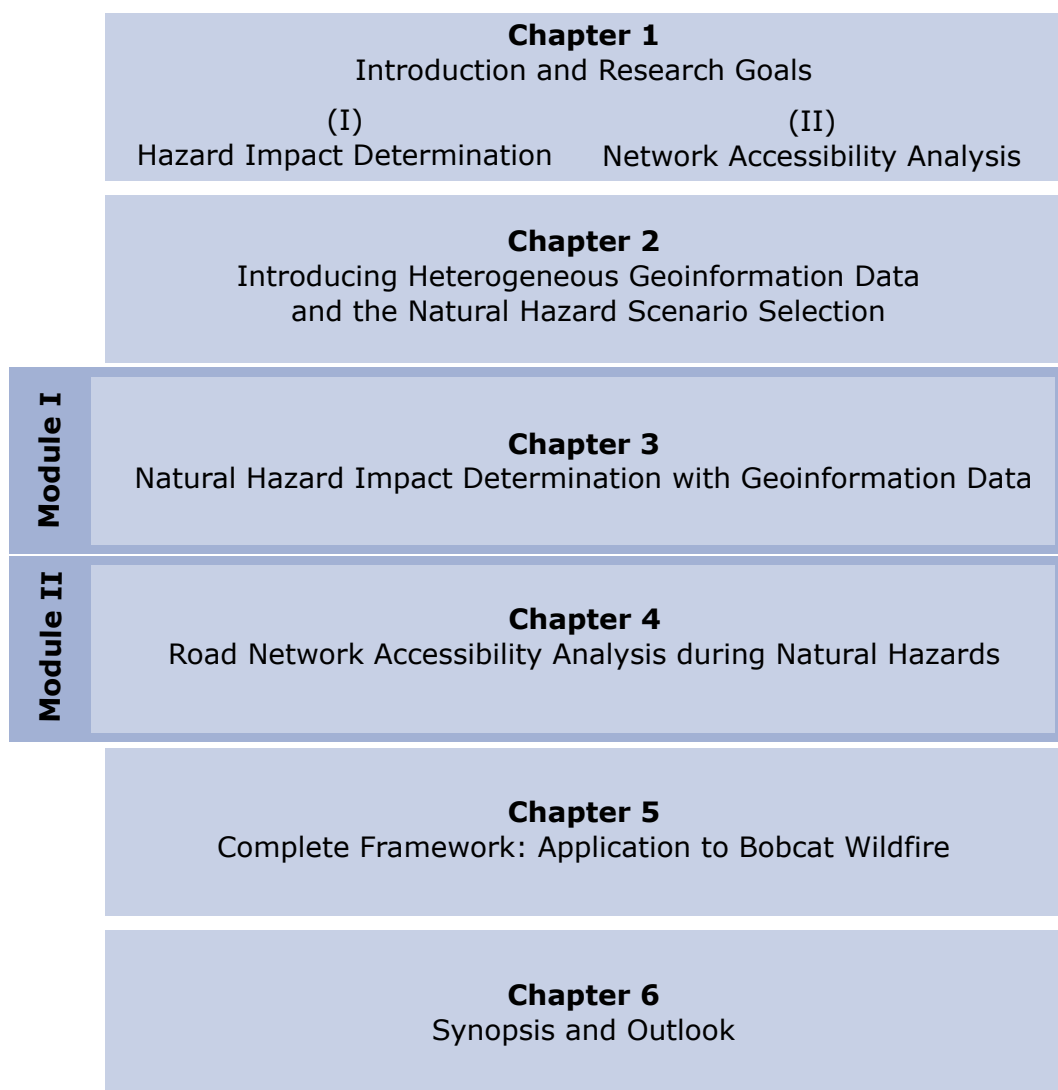


Figure 1.1.: Structure of this thesis.

Introducing Heterogeneous Geoinformation Data and the Natural Hazard Scenario Selection

This chapter includes elements from

[14] J. Florath and S. Keller. “Supervised Machine Learning Approaches on Multi-spectral Remote Sensing Data for a Combined Detection of Fire and Burned Area”. In: *Remote Sensing* 14.3 (2022), p. 657

marked with a [blue line](#). This chapter also includes elements from

[43] J. Florath, J. Chanussot, and S. Keller. “Utilizing Volunteered Geographic Information for Real-Time Analysis of Fire Hazards: Investigating the Potential of Twitter Data in Assessing the Impacted Areas”. In: *Fire* 7.1 (2023), p. 6

marked with an [orange line](#). This chapter also includes elements from

[44] J. Florath, J. Chanussot, and S. Keller. “Rapid natural hazard extent estimation from twitter data: investigation for hurricane impact areas”. In: *Natural Hazards* (2024), pp. 1–22

marked with a [purple line](#). This chapter also includes elements from

[1] J. Florath, J. Chanussot, and S. Keller. “Road Accessibility during Natural Hazards Based on Volunteered Geographic Information Data and Network Analysis”. In: *ISPRS International Journal of Geo-Information* 13.4 (2024), p. 107

marked with a [green line](#).

This chapter serves as an introduction to geoinformation data, which provide the basis for the subsequent investigations. It introduces heterogeneous geoinformation data that can be used as data sources for the different approaches to achieve the two major research objectives of this thesis. Furthermore, this chapter introduces the hazards that are used throughout the thesis as application scenarios for the developed methodologies.

2.1 Introducing Geoinformation Data

Geoinformation data capture information with spatial references about geographical phenomena. By integrating multiple data sources, existing information gaps in one data source can be filled by others. Examples of geoinformation data are satellite images, GPS, and cadastral data that can be employed in various applications like geostatistical modeling, spatial pattern recognition or event prediction. A variety of geoinformation sensors like RS sensors, aircraft surveys, cameras, Global Positioning System (GPS) and ground surveys exist.

For the framework to conduct hazard impact analysis on road infrastructure, the use of freely and openly available geoinformation data sources is necessary. Therefore, the choice of suitable data that guarantee the transferability of the framework is a crucial component. Geoinformation data provide the spatial context that is crucial for understanding natural hazards. Furthermore, geoinformation data have several benefits for analyzing road network accessibility [14, 15, 16]. Suitable geoinformation data should provide the following benefits for the analysis of the impacts of natural hazards on the road network:

1. **Universal Applicability:** The data should be applicable globally. They should be available preferably for any region worldwide and different types of geographical settings.
2. **Scalability:** The data should be usable on any scale, e.g., whether investigating city-level or regional areas.
3. **Temporal Dynamics:** The data should capture temporal changes in the respective investigated regions to allow the analysis of development of hazards over time.

Due to these advantages of appropriate geoinformation data the framework can be developed based on these data. Therefore, in the following, geoinformation data suitable for natural hazard area estimation and network accessibility assessment are reviewed. These are RS and VGI data for natural hazard impact determination (Section 2.1.1) and OSM data for network accessibility assessment (Section 2.1.2).

2.1.1 Geoinformation Data for Natural Hazard Impact Determination

Two important geoinformation datasets that provide valuable insights into spatial natural hazard characteristics are RS and VGI. Note, that the focus lies on satellite RS in the following. Compared to other sources of geoinformation data, RS imagery and VGI data have several advantages:

1. **Spatial Coverage:** Both data sources provide wide spatial coverage compared to other geoinformation data like, e.g., GPS measurements. RS sensors can capture large spatial areas that they overpass. VGI data are mostly available worldwide.
2. **Temporal Resolution:** Both data sources have comparatively high temporal resolutions. RS data are updated during each satellite's overpass time mostly every few days. VGI data are updated whenever information is posted by a user in real-time.
3. **Accessibility and Cost:** RS data can be obtained online from the satellite providers and some type of data are freely accessible. VGI data are easily accessible through Application Programming Interfaces (APIs) and usually free of charge.

Therefore, these freely and openly available data sources can be easily used for spatial analysis workflows that need to guarantee transferability and generic applicability on different hazards and study regions. Figure 2.1 summarizes the advantages and disadvantages of using the two different sources VGI and RS for natural hazard analysis. On the one hand, RS technology enables detailed mapping of natural hazards with high resolutions, making it possible to detect even small variations in the environment. This level of detail is crucial for understanding hazards like wildfires, floods, and landslides. Furthermore, RS offers the main advantage of objectivity. The data are collected systematically, ensuring the reliability of information at a large geographic scale.

On the other hand, VGI data rely on citizen knowledge that can provide detailed, real-time information. VGI can contribute data on critical factors such as the status of local infrastructure. These localized data provide insights that may not be available through traditional data sources. The integration of the two datasets offers unique advantages and has the potential to improve the accuracy of geospatial hazard analyses. While RS data provide complete, objective data on a large scale, VGI data offer localized, real-time insights. Consequently, these data are used for the near-real-time natural hazard impact determination framework in this work. In the following, studies using these suitable geoinformation data for the natural hazard impact determination are presented. A variety of hazards are covered to demonstrate the usability of these data for any hazards. These types of RS and VGI data can be replaced as necessary in the framework to adapt it to various hazards and therefore guarantee its transferability.

Aspect	RS	VGI
Data Accessibility	+ Frequently openly accessible	+ Frequently openly accessible
Data Availability	- Depends on sensor capabilities and orbit	+ Collection by crowdsourcing - Depends on user participation
Data Consistency	+ Repeated coverage, sensor capabilities	- Large variations
Timeliness	- Limited to satellite revisit time	+ Real-time updates and quick responses
Information Gain	- Mostly spatial information	+ Spatial, sentimental, trend, etc information
Spatial Resolution	+ High for some sensors - Low for some sensors	- Data sparse in remote areas + Data dense in urban areas
Reliability	+ Sensors calibrated & validated with groundtruth	- Lack of data - Potential for misinformation
Atmospheric Interference	- Some sensors affected by atm. conditions	+ Lesser susceptibility to weather conditions

+ Advantages - Disadvantages

Figure 2.1.: Overview of the advantages (+) and disadvantages (-) of Volunteered Geographic Information (VGI) data and remote sensing (RS) data by relevant aspects for spatial analysis of natural hazards.

Remote Sensing Data

Remote sensors monitor the Earth's surface, capturing various information about, e.g., its vegetation, land cover, topography, or climate. RS data have become a valuable source of information for analyzing and assessing various natural hazards [45]. The related work is structured into two parts: a short overview of studies using RS data for the mapping, damage assessment and/or prediction of various natural hazards other than the ones employed in this work, and a more detailed examination of studies specifically focused on flood, TC and wildfire analysis. These studies are organized according to the instruments used for recording reflection in different band lengths within different sections of the electromagnetic spectrum. Bands in certain electromagnetic spectrum sections were used in the analysis of the respective studies, while other bands provided by the same mission instrument were not used in some cases. This overlap may lead to sensors, e.g., the Moderate Resolution Imaging Spectroradiometer (MODIS), being named in the *Thermal*

and *Optical* categories in this overview. Table 2.1 summarizes the satellite sensors and exemplary studies and their employed satellite data for the respective natural hazards.

RS can be effectively used for mapping and monitoring landslides. Various RS techniques provide valuable information for landslide analysis. Commonly used approaches include: optical sensors to detect changes in land cover [46, 47], Synthetic Aperture Radar (SAR) [48, 49, 50] and Interferometric Synthetic Aperture Radar (InSAR) sensors to detect ground surface displacement [51, 52, 53], and the combination of these [54].

RS data are used to assess earthquake-induced damage in affected regions. These data sources help in identifying collapsed buildings, infrastructure damage, and changes in land cover that occurred due to seismic events. RS contributes to earthquake research using the following sensors: optical sensors for damage assessment [18, 55], InSAR sensors to generate displacement maps [56, 57, 58], thermal [59, 60], and gravity sensors [61, 62].

Various RS sensors can be employed for volcano monitoring, including thermal sensors measuring emitted heat [63, 64], gas sensors for sulfur dioxide and carbon dioxide measurement [65, 66, 67], SAR [68] and InSAR sensors for ground deformation measurement [69, 70], and optical sensors to map lava flows [71], or combinations of these [72, 73, 74].

RS data play a crucial role in analyzing drought conditions and their impacts on affected regions. RS technology contributes to drought research through various sensors, including optical sensors for vegetation health assessment [75, 76], SAR sensors to monitor soil moisture [77], thermal sensors for detecting temperature variations [78], meteorological sensors for assessing climatic conditions [79], and combinations of these [80, 81].

RS data are used for flood mapping and monitoring. By analyzing the changes in water extent, RS helps in understanding flood dynamics and estimating flood extent. Various RS sensors can be employed for flood mapping, including optical, SAR and thermal sensors, or combinations of these. Optical data have been used mostly in older studies [82, 83]. Recently, Sentinel-1 SAR [84, 15] data allowing the detection of floodwaters regardless of cloud cover and combinations of Sentinel-1 SAR data and Sentinel-2 optical data have been used extensively [85, 86]. Furthermore, thermal sensors measure the emitted infrared radiation, which can be used to identify temperature differences and anomalies associated with flooding [87, 88].

Satellite data are used to track and monitor TCs. Data obtained by the following sensors can be used for mapping TCs: SAR, atmosphere sensors, thermal, and optical sensors, and combinations of these. SAR sensors can penetrate cloud cover and provide detailed imaging of cyclones. SAR images are particularly useful for wind structure and intensity analysis of TCs [89, 90]. Weather satellites monitor the Earth's atmosphere and their data are used in the prediction of TCs in addition with other data [91, 92, 93]. Thermal sensors

measure the difference of microwave emissions from the Earth's surface before and after the occurrence of TCs. Change observations in microwave emissions allow the detection of cyclones and their characteristics [94]. Optical sensor imagery can be used for the detection of TCs. Furthermore, optical images acquired after the passing of TCs enable the analysis of their impacts on the ground [95, 96, 97]. Combinations of different sensors have been used for impact analysis [98].

Fire detection and monitoring can be conducted with satellite-based RS data, including thermal imagery or optical sensors. Currently, existing studies cover either the topic of active fire detection or burned area mapping. Therefore, the related work is structured in two parts: an overview of studies dealing with active fire detection and studies dealing with burned area mapping. While thermal data are an obvious choice for fire detection, it is not helpful for burned areas after cooling down. Thermal sensors measure the emitted radiation, which can be used to identify temperature differences and anomalies associated with wildfires (e.g., [99, 100]). To evaluate data acquired from thermal sensors with regard to fire detection, two main approaches are applied: contextual algorithms and the use of thresholds for thermal data [101, 102, 103]. Optical sensors can help identify fire areas by analyzing changes, e.g., in vegetation reflectance patterns. Optical data have been used mostly to exploit the higher resolution compared to thermal data (e.g., [104, 105]). For mapping burned areas, an even wider variety of different data are used. Several types of RS data can be used for mapping burned areas, these are: SAR, thermal, optical, and combinations of these. SAR is particularly useful in burned area mapping as it can penetrate smoke emitted by fires and clouds [106]. Thermal sensors can detect thermal radiation still emitted by recently burned areas [107]. Optical sensors can also detect post-fire changes in vegetation cover [108, 109]. Combinations of different sensors have been also used for burned area analysis [110]. When focusing on methodological approaches for detecting burned areas based on optical satellite data, a variety of different approaches exist (see, for example, most recently [111, 112, 108, 109]). Very few studies focus on the detection of active fires and burned areas in one go using the same sensor data and detection technique. Barducci et al. [113] rely on the spectral reflectance in the bands of the Multispectral Infrared and Visible Imaging Spectrometer for the detection of active fires and burned areas. Cicala et al. [114] use several indices for both fire and burned area detection.

Overall, satellite RS data are highly suitable for studying and monitoring a variety of natural hazards. The combination of wide area coverage and oftentimes cost-effective data usage makes RS a good tool for natural hazard analysis. Especially in areas that would be dangerous to access otherwise during a hazard, RS data play a crucial role. Finally, the timely and high-resolution insights gained from RS data can be used widely in a natural hazard context.

Table 2.1.: Overview of the related work concerning natural hazard investigations with satellite remote sensing (RS) sensors.

Hazard	Sensor	Satellite Data and Exemplary Studies
Landslides	SAR	Sentinel (S)-1 [48, 49], European Remote Sensing Satellite (ERS) [50]
	InSAR	S-1 [51, 52], ERS [53]
	Optical	Satellite Pour l'Observation de la Terre (SPOT)-5 [46], Landsat, SPOT 1-5, Advanced Spaceborne Thermal Emission and Reflection Radiometer (ASTER), Indian Remote Sensing (IRS)-1C LISS III & RapidEye [47]
	Combination	ERS1/2 & ENVISAT & Shuttle Radar Topography Mission (SRTM) [54]
Earthquakes	Optical	QuickBird [18], WorldView-3 [55]
	InSAR	S-1 [56, 57], ERS, ENVISAT, RADARSAT-2 (RSAT2) & S-1 [58]
	Thermal	Global Change Observation Mission (GCOM)-W1 [59], Moderate-resolution Imaging Spectroradiometer (MODIS) [60]
	Gravity Field	Gravity Recovery And Climate Experiment (GRACE) [61, 62]
Volcanos	Gas/Atmosphere	S-5 Precursor [65], Aura [66, 67]
	Thermal	Terra/MODIS, Aqua/MODIS, Terra/ASTER & Landsat Thermal Infrared (TIR) [63], MODIS [64]
	SAR	RSAT2 [68]
	InSAR	S-1 [69], COSMO-SkyMed, TerraSAR-X & S-1 [70]
	Optical	Landsat 1, Landsat 4, Landsat 5, Landsat 7, ASTER & Landsat 8 [71]
	Combination	S-1/2 [72], MODIS, Spinning Enhanced Visible and InfraRed Imager (SEVIRI), Visible Infrared Imaging Radiometer Suite (VIIRS)& S-1 [73], Pleiades satellite, TerraSAR-X, TanDEM-X, MODIS, S-2 & Landsat 8 [74]
Droughts	Optical	MODIS [75], Landsat [76]

Continued on Next Page

Table 2.1 Continued from Previous Page

Hazard	Sensor	Satellite Data and Exemplary Studies
Droughts	SAR	S-1 [77]
	Thermal	Geostationary Operational Environmental Satellite (GOES), Landsat 5& 7, MODIS, Advanced Very High Resolution Radiometer (AVHRR) & ASTER [78]
	Meteorological	Tropical Rainfall Measuring Mission (TRMM) [79]
	Combination	S-1, S-2 & Landsat 8 [80], GOES & MODIS [81]
Floods	Optical	Landsat [82], MODIS [83]
	SAR	S-1 [84, 15]
	Thermal	Suomi-National Polar-orbiting Partnership (NPP), VIIRS & GOES-R Advanced Baseline Imager (ABI) [88], Scanning Multichannel Microwave Radiometer (SMMR) [87]
	Combination	S-1 & 2 [85, 86]
Cyclones	SAR	RSAT2 [89], RSAT2 & S-1 [90]
	Weather/Atmosphere	KALPANA-I [91], COSMIC, Meteorological Operational Satellite (MetOp), FengYun (FY)-3 [92], Aqua, MetOp-A/ -B/ -C, Suomi NPP & National Oceanic and Atmospheric Administration (NOAA)-20 [93]
	Thermal	FY-4B [94]
	Optical	Landsat 8 & S-2 [95], Landsat [96], Landsat 7 [97]
	Combination	S-1/2 [98]
Wildfires	Thermal	ASTER [99], VIIRS [100], MODIS [115, 116, 107]
	Optical	Landsat [104, 105], ASTER [117], S-2 [108, 109], Landsat [118], Landsat/S [114]
	SAR	RSAT2 [106], Envisat [119], S-1 [120], PAL-SAR [121]
	Combination	MODIS & Landsat [110], Multispectral Infrared and Visible Imaging Spectrometer (MIVIS) [113]

Volunteered Geographic Information Data

VGI data consist of various georeferenced data voluntarily contributed by non-expert individuals. Non-experts can contribute intentionally or passively to the creation of the geoinformation data. VGI data have been used for a variety of tasks like environmental monitoring [122], disaster response [123], urban planning [124], transportation management [125], and social studies [126]. Furthermore, the integration with traditional geoinformation data can enable additional advantages for near-real-time analyses. In natural hazard assessments, VGI data can greatly contribute with its on-site observations and local knowledge information. Among others, Social Media Data (SMD) data and OSM data are combined under the VGI concept.

This section focuses on SMD data, while OSM data are reviewed in Section 2.1.2. Social media platforms, such as Twitter (now X), Facebook, and Instagram, provide user-generated content that includes, e.g., geotagged posts, photos, and videos. However, the reliability of VGI data remains a critical concern, as it is generated by non-experts and can be subject to various biases and limitations. Studies have explored this reliability issue, primarily for Twitter data, revealing both accurate real-time updates during large-scale events and inaccuracies for less prominent events [127, 128, 129, 23]. Sociodemographic biases of Twitter users can skew interpretations, and efforts to understand and adjust for these biases have been made [126, 130]. Geospatial factors like population density impact tweet distribution patterns [131, 132], while detailed sociodemographic factors (as investigated by Adnan et al. [126]) might not be crucial for hazard-related spatial analysis. To enhance reliability, e.g., credible accounts with metadata should be considered, re-tweets avoided, and government agency accounts should be accorded a higher level of trustworthiness.

In this section, previously published studies using SMD for natural hazard impact determination are reviewed. Mainly, the focus is placed on the use of Twitter data as it has proven a valuable source of real-time information and insights (e.g., [22, 23, 24]). OSM data which can be used for network accessibility analysis are reviewed in Section 2.1.2. The related work is structured into two major parts: first, the extraction of locations from Twitter data, which only then classifies Twitter data as VGI data, and an overview of studies dealing with the analysis of natural hazards from VGI data.

In order to use Twitter data as VGI data, the extraction of the locations of tweets is necessary. Geolocation accuracy of tweet points is vital for spatial hazard analysis. A variety of techniques is used for location extraction from Twitter data. The choice of these extraction techniques mainly determines the accuracy of locations. Four main categories for location extraction can be constituted:

- Inference from the user location [133, 134]: These approaches make use of the assumptions that a user's location is strongly related to their social network location.

- Location extraction from the posted text [135, 136, 137]: These studies extract names of places from the text of the messages. This task is well-known as Named Entity Recognition (NER) as a sub-category of Natural Language Processing (NLP). Few studies [138] also use pattern recognition with Regular Expressions (RegEx) for specific location name extraction. In a final step, the extracted names of places are geocoded by geoparsing.
- Direct location extraction: Locations can be directly extracted from metadata obtained with the text data when accessing VGI, e.g., via an API. Twitter, for example, delivers a Java Script Object Notation file that provides the `coordinates` or a `place` field, with information where the tweets were created [23]. However, the user can voluntarily fill these fields, so the information is rarely available. Studies suggest that coordinates are given in about 0.2 % to 1.5 % of posted tweets, while the place is given in about 2 % of the tweets [139, 140].
- Combinations of all of the above: Some studies use a combined methodology of the possibilities mentioned above for geolocation extraction [141, 142].

The use of VGI data, and Twitter data more specifically, in a natural hazard context can be categorized into three major topics: event detection, information retrieval for a specific event and spatial analysis for approximate hazard location estimation.

A brief overview of studies concerning event detection and information retrieval is provided, while a comprehensive analysis is conducted for spatial analysis derived from VGI. Table 2.2 summarizes exemplary studies for different hazards and different applications. One main application of geolocated VGI data is detecting so-called events. An 'event' hereby refers to an incident that engages a lot of VGI data creation in a given location at a specific time. The common idea of these studies is that an unusually high number of tweets in an area might be a sign for the happening of a natural hazard event. Event detection has been carried out mostly for floods [143, 144, 123], landslides [145, 122], earthquakes [146, 147] and fires [148, 149] using VGI data, mostly Twitter data. Some studies investigate VGI data for event detection in general or for multiple hazards [150, 151, 152, 153, 20, 154]. Another main application of VGI data in a natural hazard context is information extraction from VGI. Information extraction mainly relies on text classification via NLP of the VGI data to extract valuable event-related information. Furthermore, also VGI images associated with text can be evaluated for valuable information. Many studies pursue this approach for damage or hazard severity analysis [21, 155, 156] or information categorization [24]. Information extraction has been carried out for many different hazards, like floods [157, 156, 158, 159, 160], tsunamis [161], earthquakes [162, 163], TCs [164, 165] and fires [166, 167, 168, 169]. Some studies investigate VGI data for information retrieval for multiple hazards [170, 171, 24, 172, 173].

Spatial analyses for more precise natural hazard extent estimation have not been applied frequently. However, a wide variety of methodological approaches exists for spatial analysis

Table 2.2.: Overview of the related work concerning the use of Volunteered Geographic Information (VGI) and Twitter data during natural hazard scenarios. The following abbreviation is used: TC - tropical cyclone.

Topic	Hazard	Exemplary Studies
Event Detection	Flood	[143, 144, 123]
	Landslide	[145, 122]
	Earthquake	[146, 147]
	Fire	[148, 149]
	Various	[150, 151, 152, 153, 20, 154]
Information Retrieval	Flood	[157, 156, 158, 159, 160]
	Tsunami	[161]
	Earthquake	[162, 163]
	TC	[164, 165]
	Fire	[166, 167, 168, 169]
	Various	[170, 171, 24, 172, 173]
Spatial Analysis	Flood	[132, 158, 174, 175]
	Rainstorm	[21]
	TC	[131, 176]
	Fire	[22, 177, 178]

of VGI data (see Table 2.2). Some studies rely on kernel density estimation for hurricane and fire hazards [131, 22, 176, 178]. Furthermore, Voronoi tessellation has been applied to a rainstorm hazard [21]. A third approach is a triangulation for a fire hazard [177]. In this approach, VGI images are also used, enhancing the triangulation results as the shooting angles can be included. De Albuquerque et al. [158] use a generalized additive model to provide evidence for the association between the relevance of VGI data and the proximity to and the severity of flood events. Ponukumati et al. [132] conduct a Twitter based flood inventory, whose accuracy is quantified through a hit ratio compared to inventories conducted from different data sources. The values 0.86, 0.94, and 0.84 were obtained for the three events, suggesting that the Twitter-based inventory is highly accurate. The crisis mapping service invented by Middleton et al. [174] applies a standard hierarchical clustering algorithm to compute clusters of hazard related tweets from the location geometry. The flood area results correspond well with expert post-event assessed hazard area. Alyaqout et al. [175] investigate flood depth based on VGI information.

Overall, VGI data in the form of SMD data provide real-time, geotagged, on site information during hazard events, which make them very valuable for hazard analysis. The spatial and temporal structure of these data allow for mapping and tracking of evolving hazard situations. However, although the data have mostly been used for event detection and information retrieval before, they also shows a great potential for spatial analyses of natural hazards. SMD offer invaluable insights that complement traditional data sources and offer the possibility to improve disaster response strategies.

Combination of RS and VGI Data

The combined use of RS and VGI data has emerged as a powerful approach for geospatial analysis. Studies on the integration of RS and VGI for the spatial analysis of natural hazards are reviewed in the following.

Table 2.3 summarizes the satellite sensors used in approaches combined with VGI and exemplary studies for the respective natural hazards. Jongman et al. [26] compare flood areas identified from RS data with those based on Twitter activity, noting Type II Errors in RS (missed floods) and Type I Errors in Twitter data (false positives). Sadiq et al. [28] combine S-1 RS data and VGI data for flood hazards, finding confirmatory, complementary, and novel signals when comparing both sources. Cervone et al. [179] use VGI to task RS data collection in a flood case study. Similarly, Andreadis et al. [30] use Twitter data to detect earthquake locations and to task RS data collection. Mast et al. [29] discuss the correlation between online attention (VGI) and physical impact of floods (RS) in general. Wang et al. [16] demonstrate that the addition of real-time Twitter information to satellite images after a flood helps to assess water retreat. Integrating social media data and satellite imagery promises higher potential to identify ashfall following volcanic eruptions [27]. Bischke et al. [180] present a system for the contextual enrichment of satellite images with VGI information for wildfires. Boulton et al. [181] show that social media activity about wildfires is both temporally and spatially correlated with wildfire events.

Table 2.3.: Overview of the related work concerning the use of Volunteered Geographic Information (VGI) data in combination with remote sensing (RS) data during natural hazard scenarios.

Hazard	Satellite Data and Exemplary Studies
Flood	Global Flood Detection System (GFDS) [26], S-1 [28], WorldView2 & Landsat 8 [179], Global Flood Monitoring (GFM) [29], Earth Observing (EO)-1 & Landsat 8 [16]
Earthquakes	S-1 [30]
Volcanoes	Duwata-2 [27]
Fire	Landsat 8 [180], MODIS [181]

In conclusion, several studies combine VGI information with other information sources like RS data for natural hazard analysis. The combination of RS and VGI has proved to be meaningful primarily in the context of spatial analysis of hazards. Furthermore, the integration also improves the findings made by one data source through adding further information. However, the integration of RS and VGI has mostly been used only for the mutual evaluation of these datasets not for actively using the combination of both for higher accuracy spatial analyses.

2.1.2 Geoinformation Data for Network Accessibility Assessment

Network data are required for the network accessibility assessment of degraded road networks during natural hazards. OSM data are a good source of geoinformation data for network accessibility assessment due to their crowd-sourced nature and comprehensive coverage. OSM data provide detailed and up-to-date information about roads, transportation networks, and points of interest. This makes them highly useful for analyzing transportation infrastructure and assessing accessibility to various locations.

Open Street Map Data

In this thesis, OSM are used for road network analysis. The OSM project is widely recognized as the most popular and prominent VGI mapping initiative [182]. Launched in 2004, its primary objective is to generate and offer freely accessible geographic data. For a road network accessibility analysis, road networks of OSM data are employed. OSM street networks are represented as graphs, which are mathematical representations of networks [183]. In general, a graph, denoted as G , comprises a collection of nodes, represented by the set N , connected by edges, represented by the set E . In a street network, intersections and dead-ends are depicted as nodes, whereas the street segments connecting them are represented by edges. An edge establishes a connection between two nodes or, in the case of self-loops, within a single node. In a directed graph, each edge indicates a specific direction, pointing from one node to another. In a street network, directed edges represent the driving direction. Furthermore, street network graphs allow for parallel edges representing several lanes or of one lane [31].

Connected graph models favorably without errors in the data are necessary for correct road network analysis. In contrary to most authoritative road data, OSM data do not contain road names in full detail. On the other hand, many additional tags are available for each road segment, adding attributes like `travel speed` or `maximum number of lanes` to the edges [12]. OSMnx [184] is a python package that allows users to retrieve geospatial data from OSM. These data are subjected to a cleaning process, followed by the creation of graph-theoretic models [185]. OSMnx retrieves speed limits from OSM data where available and allows to impute missing speed data (e.g., using default speeds based on the functional class of the road). Furthermore, it allows to calculate travel times, respectively, for all edges.

2.1.3 Synthesis on RS and VGI Data and Integration in Framework

The use of geoinformation data (compare Section 2.1), and within this category, the use of RS and VGI (compare Section 2.1.1 and Section 2.1.2) data, provide several benefits for the development of a complete and generic framework for the analysis of road network accessibility under the influence of natural hazards' impacts.

Firstly, RS and VGI data in the form of SMD present effective data sources for the spatial analysis of natural hazards separately. While RS data provide complete, objective data on a large scale, VGI data offer localized, real-time insights. The combination of the two datasets offers unique advantages through the balancing of negative and positive characteristics of each data source. This combination has the potential to improve the accuracy of geospatial hazard analyses. Secondly, OSM data, which offer detailed insights in road networks on a global scale, are highly valuable for network accessibility assessments. As they are continually updated and include useful attribute information, e.g., on road types, they provide a highly dynamic and up-to-date data source.

By combining the strengths of RS and VGI, a complete and detailed understanding of the hazards' impacts and their influence on road infrastructure can be obtained. Furthermore, these data provide specific advantages compared to other geoinformation data. In contrast, e.g., examining the impact of natural hazards on the road network by directly studying the road network and its properties [186, 187] like traffic flow has several disadvantages. These disadvantages include its complexity, often only punctual data collection, accessibility restrictions, and costs. Moreover, meteorological data that comply mostly with the requirements of spatial coverage, temporal resolution, and open accessibility, are also less valuable for hazard impact estimation and conducting network analysis based on them. Meteorological data, like precipitation and wind speed data, are valuable for the prediction of locations at risk and possible hazard extents (e.g., [188, 189]). However, they are less suitable for the retrospective precise estimation of the actual hazard extent. RS and VGIs' open and easy accessibility enhance their suitability for actual hazard estimation. Overall, these data provide an alternative and potentially more comprehensive way to analyze the post-hazard impacted extent. Their scalable spatial coverage and high temporal resolution ensure the use in a generic, multi-scale framework at different levels of investigation area sizes. However, challenges related to data quality, integration, and interpretation must be carefully considered.

2.2 Natural Hazard Scenario Selection

In this section, an overview of the selected natural hazard scenarios for the development of a suitable framework to achieve the task of assessment of natural hazards' impacts on road infrastructure with multi-source geoinformation data is given. Flood, wildfire, and TC hazard scenarios are used during the development of different components of the framework. The framework is designed with an emphasis on wildfire hazards, due to the need of focusing on one single hazard in depth. However, by adopting the approaches, this research intends to offer a generic framework that can be transferred to other hazard types. In total, eleven application scenarios are selected, which are used for the development of methodologies over the course of this thesis.

These hazards have been selected for the following reasons:

1. **Relevance:** All selected hazard events were relevant events in their respective regions, influencing the society. Therefore, these hazards would have been important to be analysed at that time to improve the management of hazard impacts on road infrastructure.
2. **Timeliness:** All hazards occurred between 2017 and 2023. The choice of recent hazards ensures that the selected hazards correspond to the actual state of road infrastructure data and general hazard management practices.
3. **Diversity (Hazards):** The use of a variety of hazard types ensures that the developed methodology is robust and adaptable. Each hazard type has different characteristics and poses different challenges that need to be accounted for.
4. **Diversity (Regions):** The hazards are chosen in a diverse range of regions and therefore landscapes, e.g., densely forested areas, mountainous terrain, grasslands and Maquis shrubland, and urban areas. This choice allows the development of methodologies that are independent of these diversities.
5. **Data Availability:** The necessary data need to be available openly and freely for the respective scenarios. Selected types of RS data which are available globally and freely, a high amount of available VGI data, and a well-documented OSM road network in the regions ensure the coverage of the respective events.
6. **Hazard Information Accuracy:** Information about the occurrence and approximate location of the hazards should be available for the scenarios to perform data crawling. Additionally, preliminary information about the hazard location are necessary to be used as reference data for some methodologies.
7. **Road Infrastructure Exposure:** Regions where road infrastructure is at risk of hazard impacts need to be selected to assess the impact on road network accessibility to improve hazard management.

8. Transferability: The methodologies developed for the selected scenarios should be transferable to other scenarios. To ensure this transferability, scenarios covering a wide spectrum of hazards and regions are selected.

These selection criteria ensure that the methodology developed in this thesis can effectively address the challenges posed by natural hazards on road infrastructure in diverse settings. Figure 2.2 visualizes all locations of the selected scenarios that are used throughout this thesis, numbered in the order they appear in. Hazards are referred to with their names, if given, or their occurrence location as the name in the absence of a universally recognized proper name for the hazard, marked in **bold** in the following text. The selected hazards are: wildfires in **California** (I), wildfires in **south-east Australia** (II), a wildfire in **central Spain** (III), **Camp** wildfire (IV) in California (CA), wildfires in **Landiras** (V) and **Var** (VI), France, TCs **Ida** (VII) and **Irma** (VIII), US, a flood in the **San Francisco Bay Area** (IX) and a subset of this flooded region, **Oakland** (X), CA, and the **Bobcat** (XI) fire, CA. Short explanations of the selection criteria for these hazards for the specific methodology development are provided in the respective sections (Section 3.1.2, Section 3.2.2, Section 3.3.2, Section 4.2, Section 5.1).



Figure 2.2.: Overview of cases study hazard locations in this thesis (I-XI). **California** (I), **south-east Australia** (II) and **central Spain** (III) fires, **Camp** (IV), **Landiras** (V) and **Var** (VI) fires, **Ida** (VII) and **Irma** (VIII) tropical cyclones, **San Francisco Bay Area** (IX) flood with subset of **Oakland** (X) and **Bobcat** (XI) fire. Data basis: © 2018 Global Administrative Areas Database (GADM). World Map Projection: Times; California Projection: World Geodetic System 1984 (WGS84).

Natural Hazard Impact Determination with Geoinformation Data

This chapter includes elements from

[14] J. Florath and S. Keller. “Supervised Machine Learning Approaches on Multi-spectral Remote Sensing Data for a Combined Detection of Fire and Burned Area”. In: *Remote Sensing* 14.3 (2022), p. 657

marked with a [blue line](#). This chapter also includes elements from

[43] J. Florath, J. Chanussot, and S. Keller. “Utilizing Volunteered Geographic Information for Real-Time Analysis of Fire Hazards: Investigating the Potential of Twitter Data in Assessing the Impacted Areas”. In: *Fire* 7.1 (2023), p. 6

marked with an [orange line](#). This chapter also includes elements from

[44] J. Florath, J. Chanussot, and S. Keller. “Rapid natural hazard extent estimation from twitter data: investigation for hurricane impact areas”. In: *Natural Hazards* (2024), pp. 1–22

marked with a [purple line](#). This chapter also includes elements from

[1] J. Florath, J. Chanussot, and S. Keller. “Road Accessibility during Natural Hazards Based on Volunteered Geographic Information Data and Network Analysis”. In: *ISPRS International Journal of Geo-Information* 13.4 (2024), p. 107

marked with a [green line](#).

In [Module I - Natural Hazard Impact Determination with Geoinformation Data](#) the first part of the framework for the assessment of natural hazards’ impacts on road infrastructure is developed. When assessing the impact of hazards on road networks, a nuanced approach is used to differentiate between two primary types of possible impacts: affected areas and direct impacts on roads.

- **Affected Areas:** Affected areas, in the following called impact zones, describe the spatial region influenced by a hazard. The specific impact of the hazard on the road network is not yet determined here, but subsequent analysis can estimate it. The use

of affected areas is based on the idea that the area has been exposed to the hazard, and further assessment will reveal the actual impacts on road infrastructure.

- **Direct Road Impacts:** Direct road impacts refers to the immediate consequences of a hazard’s impacts on the specified object of the road infrastructure. Instead of relying only on the hazard’s spatial extent, this approach analyzes how the hazard directly affects road conditions. This assessment includes any factors that directly obstruct or compromise road usability. By detecting where the hazard directly affects roads, road network impacts can be determined.

While direct road impact evaluations provide a more certain assessment of immediate hazard consequences, affected areas estimation offers a broader view on the potential indirect consequences that might occur within this area. Both are critical for effective hazard management. In hazard scenarios, complete information on direct road impacts may not be immediately available during and shortly after the hazard [190]. Citizens and road agencies can only evaluate and report on small parts of the entire road network and give information about specified road segments [191]. Although data may be incomplete, predicting the impact zone of a hazard helps to understand the possible influence on the road network in a next step (Module 2, see Chapter 4). Figure 3.1 displays the steps developed in Module I to determine the natural hazard’s influence using various geoinformation data. In addition to the impact zone, information about direct impacts on roads can be extracted from VGI data (Section 3.3). This chapter focuses solely on the extraction of possible hazard location and influences. Their specific impact on the road network is investigated and discussed in Chapter 4.

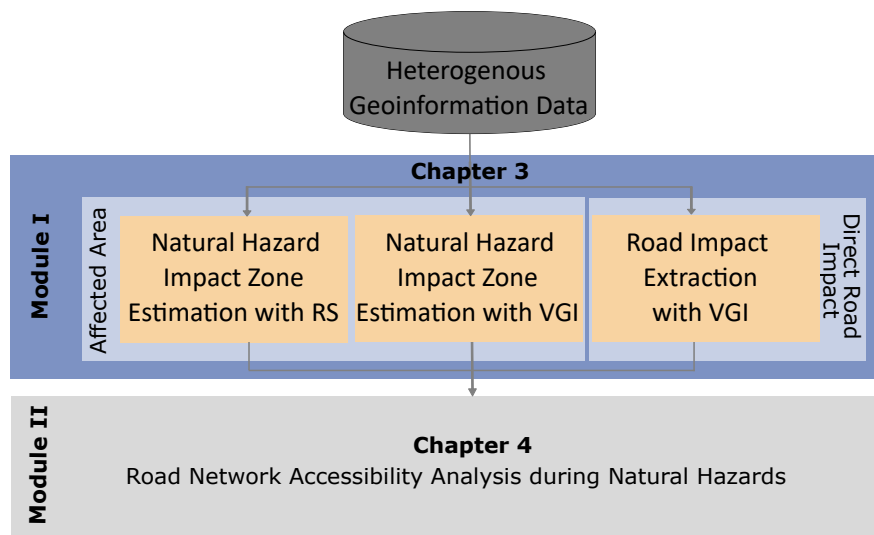


Figure 3.1.: Visualization of Module I, the natural hazard impact determination with geoinformation data. The Module I is subdivided into natural hazard impact zone estimation with remote sensing (RS) data (Section 3.1) and Volunteered Geographic Information (VGI) data (Section 3.2), and direct road impact extraction with VGI (Section 3.3). The results of this module are used as input for the consecutive Module II.

3.1 Natural Hazard Impact Zone Estimation with Remote Sensing Data

The estimation of natural hazard areas using RS data enables the rapid and accurate determination of hazard impact zones. However, it is important to recognize that each hazard type presents unique challenges and characteristics that affect the methodology for the impact area estimation. The distinct characteristics of hazards need specialized approaches using RS data to estimate the impact area (compare Section 2.1.1). Among natural hazards, wildfires emerge as a particular center of interest in disaster risk management due to their dynamic and rapidly changing behavior. Wildfires pose a specific set of challenges that require a specialized approach using RS data. Additionally, large-scale bush fires tend to occur more frequently in recent years [192]. In the following, the wildfire area estimation with RS data is investigated, serving as basis for its subsequent application in the analysis of hazard impacts on road networks.

3.1.1 Introduction

Detecting active fires quickly and on a larger scale is a critical task in the context of natural hazard analysis. Although burned area detection is not directly linked to immediate life-saving activities, mapping such burned areas supports a long-term evaluation of ecological and economic damages [193, 194]. Burned areas often remain impassable for traffic or rescue vehicles [195] and threaten inhabitants several days after the actual fire has passed.

Most studies do not consider the distinction between burned areas and areas covered with active bush fires but focus on the detection and mapping of either one of them ([110, 196] burned area, [105, 99] active fire). In some studies, areas with active fires and burned areas are declared as one single class compared to the class *Unburned* [197, 198].

In contrast, importance to this distinction between burned areas and areas covered with actual fires is attached here. The main reason for this clear distinction is that either of the characteristics poses different challenges concerning risk management or rescue mission planning. In addition, when investigating the accessibility of road networks during and after bush fires, the information if an area is burned or contains fires constitutes an essential factor. While roads within a fire area are impassable, roads within a burned area might be usable to a certain degree. A *Burned* area is referred to as an area that happens to be a place of a bush fire a short time ago. A short time ago means, in this context, several days after the firstly detected fire ended and its influence on the landscape is still apparent [199]. An area with *Fire* means a burning fire is present, which can be either the main fire front or even a small area of smoldering brushwood [99].

The detection of fire and burned area can be achieved with remote sensing data, as an increasing availability of these data can be observed in recent years. Many different approaches are already applied for either active fire detection (mostly rule-based approaches) or burned area mapping (data-driven or rule-based approaches). In this study, the focus will be on investigating and evaluating several different Machine Learning (ML) approaches for a combined fire and burned area detection. The task of detecting active fires and burned areas based on ML approaches with remote sensing data includes several challenges. In the following, the main challenges that are addressed are briefly described.

- *Combined Detection of Active Fire and Burned Area:* A combined data-driven approach for the detection of active fires and burned areas is focused on. In existing studies, different approaches are used for the two sub-tasks [114], if a distinction is performed between burned area and active fire. A methodology to detect active fires and burned areas in one go using the same ML approach for both sub-tasks is developed.
- *Configuration of Generic Concept:* The concept is set up to enable a generic detection of fire areas and burned areas. Thus, fire and burned area incidents worldwide on an appropriate scale can be distinguished with the given methodological approach independently of prior or detailed knowledge of the appearance of either class in the investigated region. This novel workflow enables facile detection of both relevant areas in one go.
- *Selection of Appropriate ML Approaches:* Many ML approaches would be eligible to carry out the task of fire and burned area detection. The applicability of several ML approaches is evaluated and the best-performing for a possible application is selected.
- *Generation of Reference Data:* Reference data are required for the training and testing steps of ML approaches. Since appropriate reference data are not available neither for active fires nor for burned areas, large-scale reference data are generated. This generation is also set up as a generic concept that can be used for reference data manufacturing in any fire and burned area detection application worldwide.
- *Detection in High Spatial Resolution:* For subsequent risk analysis, fire and burned area detection needs to be possible with very high accuracy, requiring a high spatial resolution of the chosen satellite data. A high spatial resolution enables significantly enhanced accuracy in predicting fires and assessing their impact on structures such as roads within these smaller dimensions.

To solve a combined active fire and burned area detection, the objective is to choose one sensor, from which data to implement both tasks using one selected approach can be derived. Though thermal data are well suited and state-of-the-art for fire detection [100, 115], thermal remote sensing cannot be considered for the task, as the spatial resolution is relatively low [200]. Additionally, thermal data can only be used for burned areas

estimation via active fire investigations [201] and is therefore not best suited for the task. Higher spatial resolution data are provided by optical sensors like the Landsat or Sentinel-2 sensor, which are suitable for active fire detection [104, 105]. Burned area detection is also possible with optical data [110, 193]. Therefore, the decision was made to use the Sentinel-2 sensor's data, which provides a spatial resolution of 10 m in several bands [114] for the combined burned area and fire detection task.

In contrast to the presented fire detection approaches (Section 2.1.1), indices are used in a first step [114] and then work with supervised approaches to improve the correctness of fire area detection and achieve a trustworthy fire map to be further used in applications. Supervised approaches have also been applied in burned area detection and achieve good results [197, 109]. Therefore, the use of similar approaches will be emphasized in this study. Since the revised studies involve the application of many different supervised approaches, several different ones will be tested instead of focusing on a single one.

Figure 3.2 shows our applied combined classification framework of fire and burned areas structured into different levels. First, the data are described in the dataset level covering the exemplary employed study regions **CA (I)**, **south-east (SE) Australia (II)** and **central Spain (III)** as described in Section 2.2 and the extracted input datasets (Section 3.1.2). The generated reference data are described next in the feature level in Figure 3.2. Note that we refer to the combination of input features and desired output data as a datapoint. Furthermore, in the data level, the generated datasets are processed and splitted, which is necessary for the ML models' training and evaluation. Finally, selected ML models, their optimization, and the model evaluation metrics are presented in Section 3.1.3. These parts are included in the model level of the classification framework.

3.1.2 Data

Selected Application Scenarios For fire mapping, the selection of the study area has to meet two main criteria. First, the study area should include regions characterized by big fires in the last years. Second, a variety of landscape characteristics should be part of these selected regions. Fires that occur in diverse vegetation types show different characteristics. Therefore, significant fires in three different regions and countries are utilized: CA in the US, the SE of Australia (including the States of Victoria, Australian Capital Territory, and New South Wales), and the central region of Spain. In total, four areas in **CA (I)**, five areas in **SE Australia (II)**, and one in **central Spain (III)**, mainly containing different land cover classes, are used in the RS approach. Figure 3.3 visualizes the locations of the fires. Specific information regarding these fire hazards is not provided, as these application scenarios serve as an observational benchmark for the proposed framework. In addition, the development of the approach does not depend on local fire characteristics but on the sheer data volume.

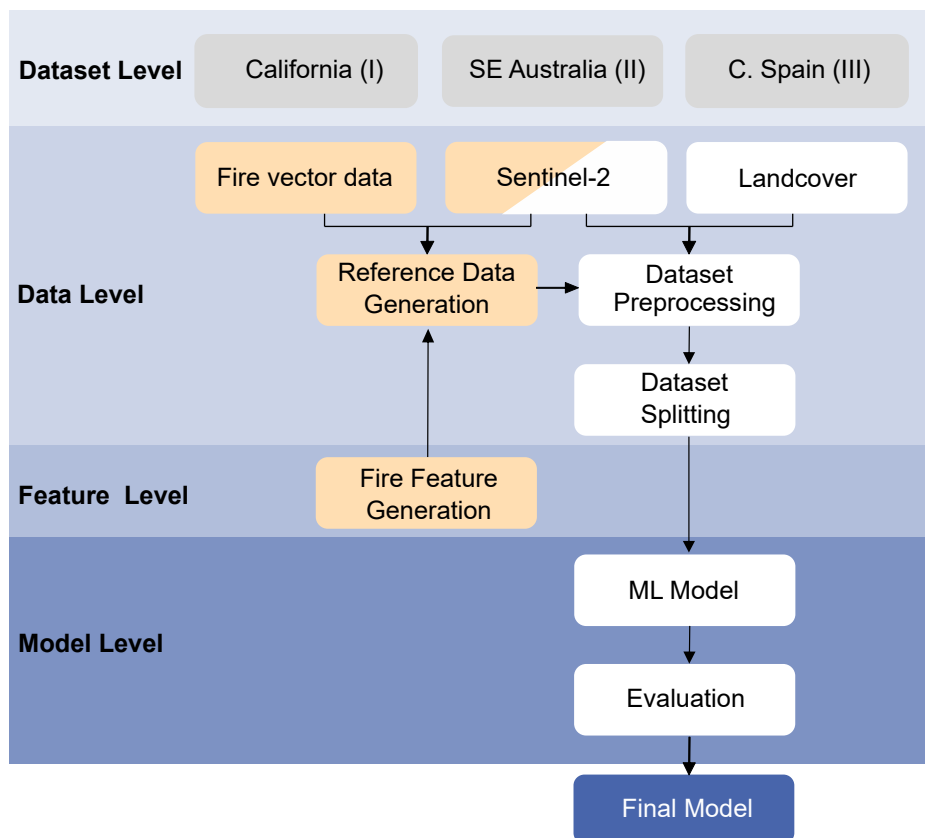


Figure 3.2.: Visualization of the combined classification framework of fires and burned areas divided into the dataset level, the data level, the feature level, and the model level. Orange: Components associated with the reference data generation phase within the framework. The following abbreviations are used: SE - Southeast; C - central; ML - Machine Learning. Reprinted from [14].

Datasets We employ optical remote sensing data in the form of Sentinel-2 data. The information in the Sentinel-2 bands is the main feature used for the classification of the fire classes. We use Sentinel-2 data to benefit from the high resolution of 10 m, given for at least 4 of its 13 spectral bands. The selected scenes are made available on the satellite mission’s download platform (Copernicus Open Access Hub) and via a Python API, called Sentinel API. Newer Sentinel-2 products are provided in Level-2A Bottom-Of-Atmosphere directly. The different bands have different spatial resolution of 10 m, 20 m, and 60 m. In Level-2A products, the cirrus Band 10 is omitted, as it does not contain surface information, so in summary, 12 spectral bands are used in this study. All bands are resampled to a 10 m resolution.

A land cover product is also acquired from an API. The land cover product is used as an additional input feature since different underlying land cover classes change the spectral reflectance of the classes of *Fire*, *Burned*, and *Unburned*.

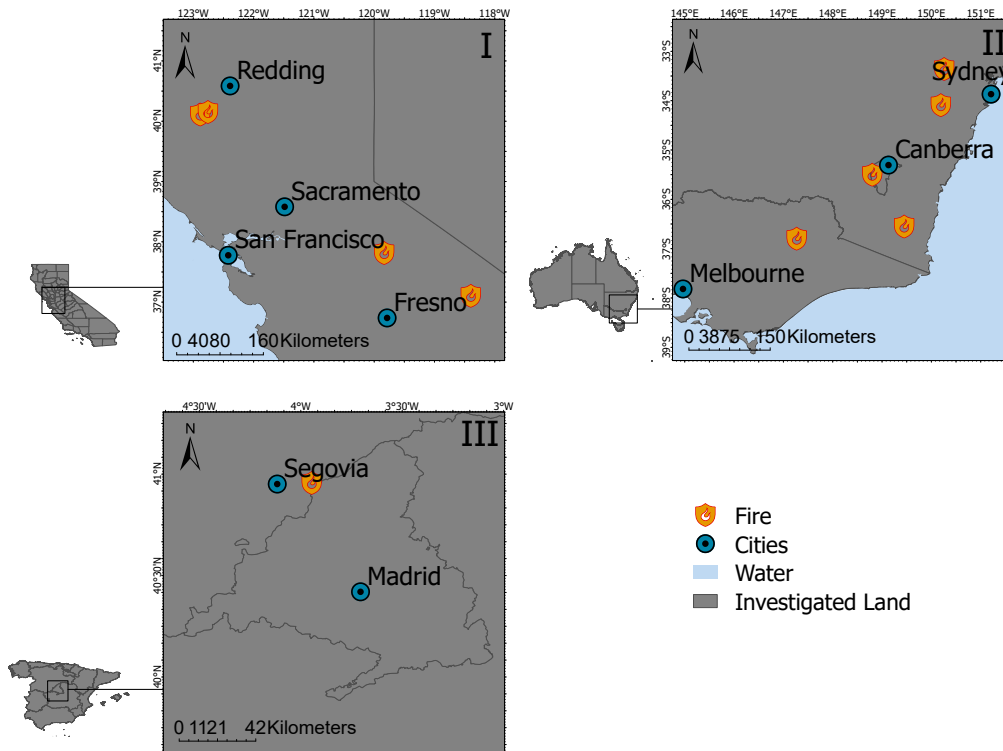


Figure 3.3.: Overview of cases study hazard locations and respective hazard types: **California (I)**, **south-east Australia (II)**, **central Spain (III)**. Data basis: © 2018 GADM. Projection: WGS84. Adapted from [14].

For example, a burned forest has a different spectral signature than a burned grassland. Thus, the ML approaches can learn during the training that several different burned land cover classes still correspond to the class *Burned* despite their spectral differences. The worldwide-available product Copernicus Global Land Cover Layers collection 3 with a 100m resolution is used [202]. The product is assessed via the GoogleEarthEngine Python API [203] and provides several bands of which the *discrete classification* is used, which includes 23 primary classes. The land cover classes are defined according to the CORINE (Coordination of Information on the Environment) Land Cover class definition. They are consistent over the entire globe. The product is derived from the PROBA-V 100 m time series. The land cover data are interpolated to a 10 m resolution by Nearest-Neighbour interpolation to retain discrete class values. Thus, its resolution corresponds with the resolution per pixel of the Sentinel-2 data. From the combination of the above input features, we obtain 13 input features in sum, containing 12 Sentinel-2 bands ignoring the band number 10 and one land cover feature for each selected Sentinel-2 pixel.

Fire perimeter data are used, which is acquired from national agencies. These data are only used to generate the reference showing unburned and burned area, which is necessary for training and testing of a model. Fire data are not available in a generalized database. Therefore, the data have been acquired for every region of interest from the responsible

governmental agency, e.g., CalFire (California, US) or data.gov.au (Australia). These data are provided in vector files, showing the extent of a fire (burned) area. For example, CalFire provides a multi-agency statewide database of fire history [204]. For each fire perimeter, metadata such as the fire name, id, size, objective are included by the responsible authority. Such data have been used as reference data in various studies (e.g., [205]). The vector data vary, depending on which agency they are provided by, concerning the temporal resolution and availability. For example, some vector files capture the outermost extent of accumulated burned area for a one-time step, and current data are available every couple of hours (e.g., three hours for data.gov.au). Other vector files capture the extent of one fire event that might have occurred for several days in a row, but data are only available once.

3.1.3 Methodology

In the following, three vital, methodological steps within the framework of supervised *Fire* and *Burned* classification are described. These are reference data generation, dataset preparation and the introduction of the applied ML models.

Reference Data Generation For the specific classification, no benchmark dataset is available in the required resolution (high spatial resolution of 10 m of Sentinel-2 data) for the target classes of *Fire*, *Burned*, and *Unburned*. Therefore, a respective dataset with all datapoints containing single pixels of the Sentinel-2/ land cover image with 13 input features (attributes) and the corresponding labels of the target class is created. In the following, we summarize the steps to generate the reference data (labels), before describing it in detail below. Figure 3.4 shows the steps 1 to 4.

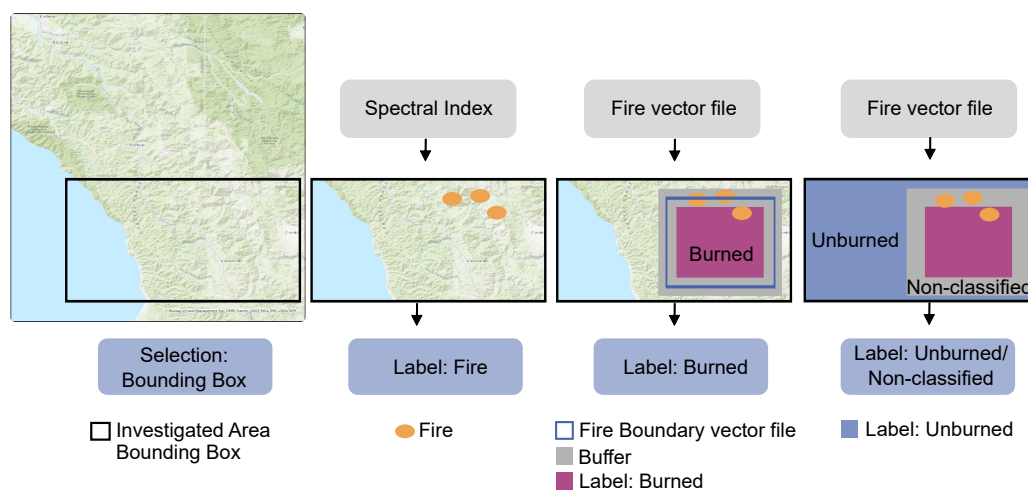


Figure 3.4.: Visualization of Steps 1 to 4 of the reference generation. Basemap: ESRI ArcGIS Pro. Projection: WGS84. Reprinted from [14].

1. Select a specific region of interest inside the study region by applying a bounding box, for which information on burned and unburned areas provided by authoritative data are available.
2. Detect an active fire area based on spectral indices. The detected pixels are labeled as *Fire*.
3. Detect a burned area based on the national agencies' fire vector file data. The detected pixels are labeled as *Burned*.
4. Finally, label the rest (neither fire nor burned) of the pixels within the bounding box as *Unburned* or *Non-classified*.

First, Step 1 requires the available and downloaded OSM data, providing information about fire areas or burned areas. Then, according to its size and the date of fire appearance, a specific fire site is chosen within the study regions from the OSM data. Simultaneously, we obtain the corresponding Sentinel-2 data of the selected region of interest several days after the set fire start date, providing reference data for burned areas. We also examine if actual fires are present in the available Sentinel-2 images, providing reference data for currently burning areas. For visual fire detection, false-color images of the Near InfraRed (NIR) (Band 8a) and Short-Wavelength InfraRed (SWIR) (Band 11 and Band 12) bands are most helpful. Thus, fires are well-detectable in the first days after the fire incident started. Concluding Step 1, we rely on areas that are detected as fire or burned areas visually and use these areas for further processing. We define a specific bounding box within this region of interest in Step 1. The corresponding Sentinel-2 image and OSM data are subsetting to the extent of this bounding box. All datapoints, respectively pixels, within this bounding box are labeled in the following steps.

For an automatic active fire detection in Step 2, several indices can be applied according to other studies (e.g., [201, 206, 108, 207]). In pre-studies, we have evaluated most of the proposed indices to select the most appropriate index for our task, the fire detection with Sentinel-2 data. We rely on the so-called active fire detection (AFD) index 3 (H_{AFD3}), according to Cicala et al. [114]. This index is regarded as most beneficial for the detection of highly energetic fires. At the same time, it is also useful for rather blazing, glowing, and therefore less energetic fires. It is calculated as follows:

$$H_{AFD3} = \frac{B_{12}}{B_{8A}} + \frac{B_{12}}{B_{11}} + \alpha \frac{B_{8A}}{B_{11}} \quad (3.1)$$

where $0 \leq \alpha < 1$ and B for Band. The indexing is applied for all pixels inside the bounding box created in Step 1. We subsequently apply thresholding. If the pixels' values are higher than the experimentally derived threshold of 5, we label these pixels as *Fire*. The rest of the pixels inside the bounding box remains unlabeled in this step.

In Step 3, we select the pixels, which cover the burned area. Therefore, we refer to the OSM data vector files as a reference for burned areas. To ensure that the pixels of the *Fire* and *Burned/Unburned* areas are not blended accidentally, we set a buffer zone around the vector file. The buffer size depends on the actual size of the OSM data vector file for the fire in question. About 100 m to 300 m buffer size is usually applied. Pixels within the OSM area but outside the buffer are then labeled as *Burned* areas. They are also reviewed, not to be accidentally labeled as *Fire* by comparison with fire labels of Step 2.

Finally, in the last step, we need to label the remaining pixels inside the bounding box area that have not been labeled yet. A pixel was already labeled as *Fire* if it is classified as fire by the AFD-3 index according to Step 2. A pixel was already labeled as *Burned* if it is located within the OSM boundary, not classified as fire and not located within the buffer zone according to Step 3. The label *Non-classified* is provided for pixels located within the buffer and not labeled as fire. For these pixels we can not be sure to which class they truly correspond from the references that are available to us. We discard these pixels to obtain only pure datapoints as input for our models. Eventually, we label pixels outside the OSM boundary and outside the buffer as *Unburned*.

For classification improvement and generalization purposes, we include pixels of the *Unburned* classes which cover water and settlement areas. These particular pixels are characterized by spectral differences and occur only in a reduced number. The main reason is that fires and burned areas appear primarily in forested regions in which these two land cover classes are relatively rare.

In sum, the reference data generation is conducted in a semi-automated manner. The extensive process for reference data generation, ensures the high reliability. However, the accuracy of the generated reference data can only be evaluated visually.

Dataset Preparation The above reference data generation is conducted for all datasets of the three application scenario regions **CA (I)**, **SE Australia (II)**, and **central Spain (III)**. Then, a dataset for the training process is created, combining all data from the selected areas of the two application scenario regions **CA (I)** and **SE Australia (II)**. This results in a combined dataset of nine fire hazards (four areas in **CA**, five areas in **SE Australia**). The datasets exhibits between-class imbalances for the target classes of *Fire*, *Burned*, and *Unburned* areas. Fire pixels are fewer, as fires do not burn continuously for long periods but have very limited periods of active burning depending on, e.g., the fuel source. Only in a relatively small area for a short period of time, during which a fire is actively burning, pixels for the label *Fire* can be captured. On the contrary, burned areas persist until local vegetation regrow. This leads to an underrepresentation of the *Fire* class. This class imbalance might impact results, particularly for the *Fire* class, which is essential for fire management and prediction. Furthermore, an imbalance within land cover classes within the three target classes is noted, affecting classification performance.

The dataset preparation process involves several steps (see Figure 3.5). First, the dataset is split into three equal subsets, denoted as Subset 1, Subset 2, and Subset 3 to reduce computational time, especially during ML training. This split is conducted randomly but guided to ensure that every subset consists of approximately the same number of datapoints per land cover class. This process is essential since some land cover classes are lowly represented. We then randomly split each subset dataset into three sets with a ratio of 60 : 20 : 20 (see Figure 3.5). Standard ML guidelines are followed with the chosen split ratio (see e.g. Kattenborn et al. [208]), and the randomized split guarantees an independent distribution of the subsets. Next, we apply a selected undersampling approach. Undersampling approaches are efficient to deal with in-between class imbalance [209]. We select an informed undersampling approach concerning the land cover classes. An undersampled training dataset of each original training subset is created by randomly undersampling only datapoints of majority land cover classes inside the majority targets, unburned and burned classes. We refer to these three under sampled training subsets as Uset 1 to 3. These subsets are used as training datasets for the ML models.

The evaluation process involves multiple tests, depicted in the following, for the case when trained on the train split of Uset 1, including:

1. Internal validation using the train split of Uset 1,
2. Test I using the test split of the respective subset, Uset 1,
3. Test II using the other two subsets (Uset 2 and Uset 3) as test data,
4. Test III using data from an unseen region in **central Spain (III)**.

The detailed process is depicted in Figure 3.5. This comprehensive evaluation ensures robust model assessment. Additionally, data preprocessing such as feature scaling is performed for certain classification approaches.

ML Models As mentioned in Section 2.1.1, several supervised learning approaches exist using Sentinel-2 input data to predict classes such as *Fire*, *Unburned*, or *Burned* successfully. These approaches comprise, for example, tree-based models, Support Vector Machines (SVM), or deep learning such as Convolutional Neural Networks (CNNs). However, the objective of this study is to evaluate the classification performances of such ML approaches to predict all of the three defined classes in one pass. Therefore, we select shallow learning approaches such as an Extremely Randomized Tree (ET) [210], an AdaBoost [211], a Gradient Boosting (GradientBoost) [212], a Multi-Layer Perceptron (MLP) [213], a supervised Self-Organizing Map (SOM) [214, 215, 216, 217], and an SVM with bagging [218]. Besides, we rely on a one-dimensional (1D) CNN, which is similar to the approach of Riese et al. [219]. The selected ML approaches have been chosen since their robustness and strong classification abilities have been proven in similar classification tasks and pre-studies (see [220, 109, 221]). Table A.1 in Appendix A.1 summarizes all applied ML models with their respective hyperparameter settings. Note that we only apply scaling as preprocessing for the deep learning approaches and the BaggingSVM.

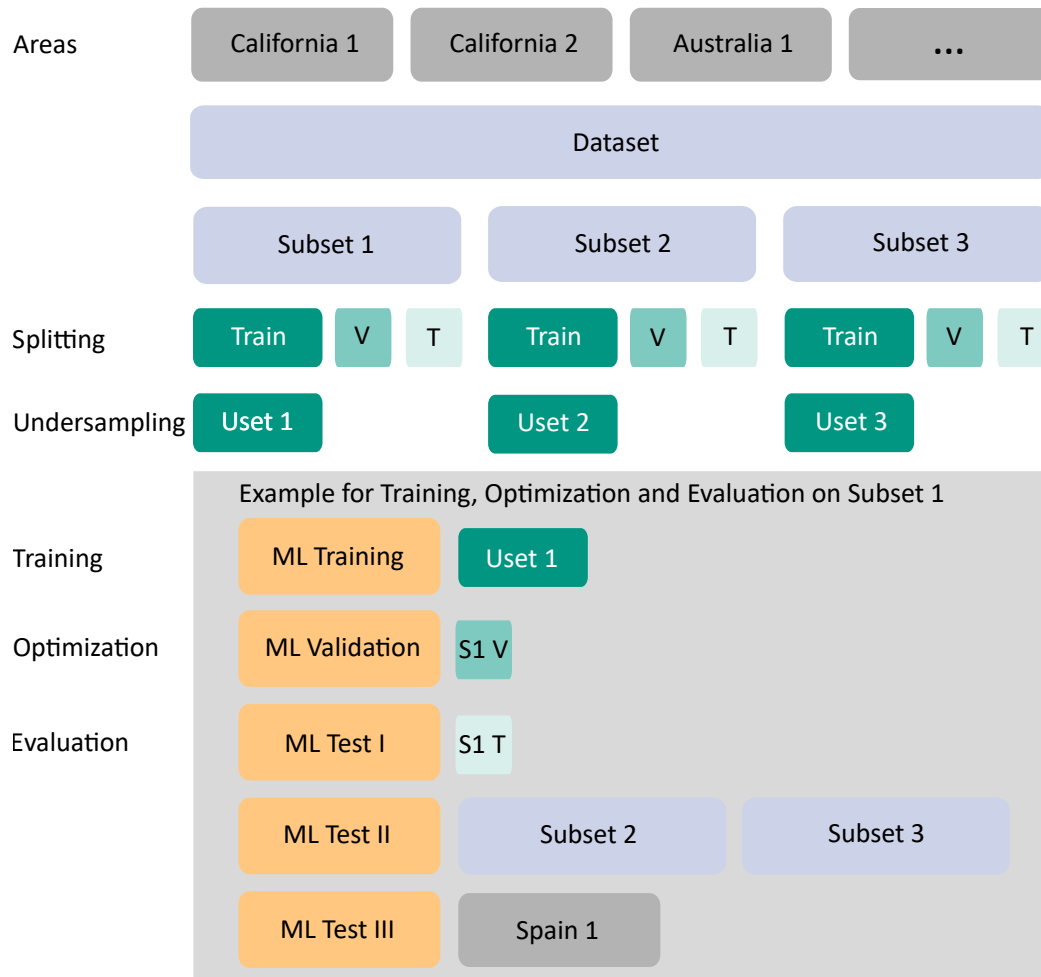


Figure 3.5.: Flow diagram summarizing the dataset preparation applied in this study with the ML process example illustrated for Uset 1. The following abbreviations are used: ML - machine learning; S - subset; T - test set; Uset - undersampled set; V - validation set. Reprinted from [14].

ET, AdaBoost, and GradientBoost are applied as tree-based classification models and are associated with decision trees. Generally, they include a root and a leaf node. Root and leaf nodes are then linked by branches. During the training of decision trees, the data of the respective dataset are split at every branch. With these splits, subsets are generated, which highly correlate to the 13 input features. For example, RF is defined by an optimum split, while ET relies on a random split, which reduces variance, according to Geurts et al. [210]. Details on the structure and set-up of the models are presented in the corresponding studies [210, 211, 212].

For the underlying classification task, we rely on the supervised classification SOM introduced by Riese et al. [215]. In sum, the supervised classification SOM contains an unsupervised and a supervised SOM. The unsupervised SOM part selects the best matching unit for each datapoint. Selecting the datapoints is implemented randomly. Then, the learning rate, neighborhood function, neighborhood distance weight matrix, and class-change probability matrix are calculated. In contrast, the supervised SOM connects the selected best matching unit to a specific class. The SOM weight matrix is modified, and the process is repeated until the maximum number of iterations is reached. The Python implementation can be found by Riese [222].

Another ML approach included in the model level is the SVM. We propose an SVM ensembles approach with bagging. In this specific case, each SVM is trained independently with randomly chosen training datapoints. Finally, these SVMs are aggregated into a collective SVMbagging [218]. This proposition is advantageous since the standard SVM storing the kernel matrix requires memory, which scales quadratically with the number of datapoints. So far, except for the classification SOM, the ML models are implemented with the Python package `scikit-learn` [223].

As an Artificial Neural Network (ANN) approach, we use an MLP. The MLP consists of a simple architecture with one input, at least one hidden, and one output layer [224]. Each node, except the input node, is a neuron that uses a nonlinear activation function. Back-propagation is applied for training. We use the standard `scikit-learn` [223]-implemented MLP architecture with the hidden layer sizes of 5 and 2. The input layer consists of 13 neurons representing our 13 input features.

Since CNNs have achieved good classification and regression results on remote sensing images and spectral data [225, 226], we also apply a CNN architecture. More precisely, we employ a 1D-CNN since the generated reference datapoints are extracted point-wise. A standard two dimensional CNN, therefore, is not applicable. The idea to deal with point-wise reference data with the help of a 1D-CNN is adapted from Riese et al. [219]. Generally, a 1D-CNN is resilient against any noise occurring in the Sentinel-2 data. Based on a 1D-CNN's deep layers, several features are created out of the 13 input features. The architecture is similar to the one implemented in Riese et al. [219]. However, it is adapted during the training process and optimized for the task.

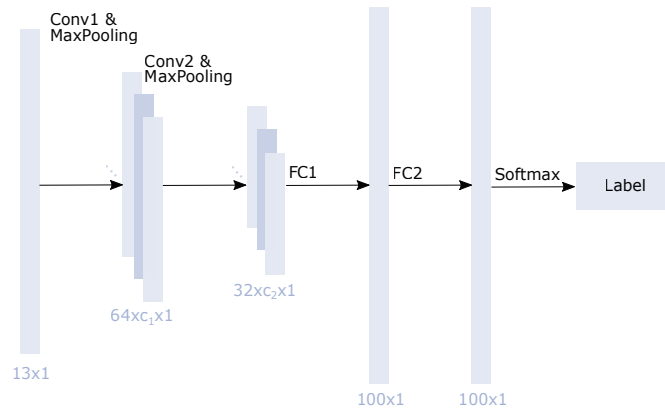


Figure 3.6.: Flowchart of the one-dimensional (1D) Convolutional Neural Network (CNN) architecture for the 13 input features during the training process. The network includes convolutional (CONV) and fully-connected (FC) layers. At the end of the network, a softmax function is applied. Adapted from [14].

Figure 3.6 shows the implemented 1D-CNN architecture. The architecture comprises two convolutional layers followed by a max-pooling layer. Two fully-connected layers, each with 100 neurons, are then employed. Softmax activation function is used for the last layer while Rectified Linear Unit is used for the other layers. The Adam optimizer is adopted. Hyperparameters of the CNN are optimized through a Hyperband tuner [227], a rapid variant of random search. It offers adaptive resource allocation and early stopping. The 1D-CNN is trained five times, and the optimal model is determined based on the highest validation accuracy across these runs. The results from these runs are averaged for assessment.

For the evaluation of the models' classification performances and the comparison of the different results, we rely on several metrics. Concerning the reference data, the prediction for a datapoint is either true positive, true negative, false positive, or false negative. The applied metrics are implemented in the `scikit-learn` [223] package. Besides, we have to consider that metrics are applied which can cope with an imbalance multiclass-classification problem. For example, the Balanced Accuracy (BA) defines such a metric suitable for imbalanced datasets. Overall Accuracy (OA), Cohen's κ coefficient, precision, Average Accuracy (AA) and F1 score are additional metrics that are usually applied in classification problems.

3.1.4 Results

In this section, the results for the estimation of natural hazard impact zones using RS data are presented. Table 3.1 shows the prediction scores of the applied ML models on the selected Subset 2. In this case, the models have been trained on Uset 3. All selected ML models achieve very high prediction scores. 1D-CNN and ET show the best classification results with an OA above 97%. The supervised classification SOM produces the least accurate results with an OA of 87%, followed by AdaBoost with 91%. When considering Cohen's κ , all models' values range from 73% to 94%, with a slightly stronger differing value of 63% for the SOM approach. With 83% to 97% for all models, the precision is similar to the models' OA values and the F1 scores. The AA score also ranges in similar values of 80% to 97% for all models. All models achieve high BA values (85% to 98%), especially ET and 1D-CNN outperform the other models with 98%. The ET achieves the best accuracies in the metrics OA to precision, while the CNN achieves best results in AA and BA. The class-wise performance of ML models is evaluated using test Subset 2, while the models were trained on Uset 3 (see Figure A.1 in Appendix A.2). The models exhibit strong discrimination among the three target classes, especially for the *Fire* class, achieving a BA score between 95-99%. The SOM's classification performance is slightly lower, with its lowest performance in classifying the *Burned* and *Unburned* classes. Notably, the 1D-CNN excels in classifying the *Unburned* class, with a score of 98.31%.

Table 3.1.: Classification metrics in % of all machine learning (ML) models trained on the Uset 3. The models' prediction is performed on Subset 2 and compared to the reference data. The one-dimensional Convolutional Neural Network (1D-CNN) scores are calculated as average of five runs. The following abbreviations are used: OA - Overall Accuracy; Prec - Precision; AA: Average Accuracy; BA - Balanced Accuracy). Reprinted from [14].

Model	OA	κ	F1	Prec	AA	BA
AdaBoost	91.2	73.6	86.8	86.8	86.9	86.9
BaggingSVM	93.7	81.1	90.5	90.6	90.5	91.8
ET	97.9	93.6	96.8	96.8	96.3	97.5
GradientBoost	95.3	86.2	93.0	93.1	93.0	94.7
MLP	96.1	88.4	94.2	94.2	94.2	94.9
SOM	86.9	63.0	81.0	82.8	80.3	85.3
1D-CNN	97.6	92.9	96.4	96.5	96.4	97.7

Performances on Different Subsets Since different subsets are used for ML model training, optimization, and evaluation, the models' classification results can be compared on the different subsets (Table 3.2). Four models with low computational costs, trained on various Uset subsets, are evaluated on the remaining Subsets, respectively. The models demonstrate consistent and satisfactory classification results across the Subsets. The ET model excels, showing minimal deviation (up to 0.9%) between training Usets and evaluating Subsets. AdaBoost has a slightly larger deviation (1.3%), but yielding the lowest AA score.

Table 3.2.: Classification results of the four selected models on different training and test data subsets. The values represent the Average Accuracy (AA) in %. Reprinted from [14].

Model	Training Test	Uset 1		Uset 2		Uset 3	
		Subset 2	Subset 3	Subset 1	Subset 3	Subset 1	Subset 2
AdaBoost		85.6	85.6	86.5	86.5	86.9	86.9
ET		96.6	96.6	97.5	96.7	97.5	96.7
GradientBoost		93.0	93.0	93.1	93.1	93.0	93.0
MLP		94.0	94.0	94.0	94.0	94.1	94.2

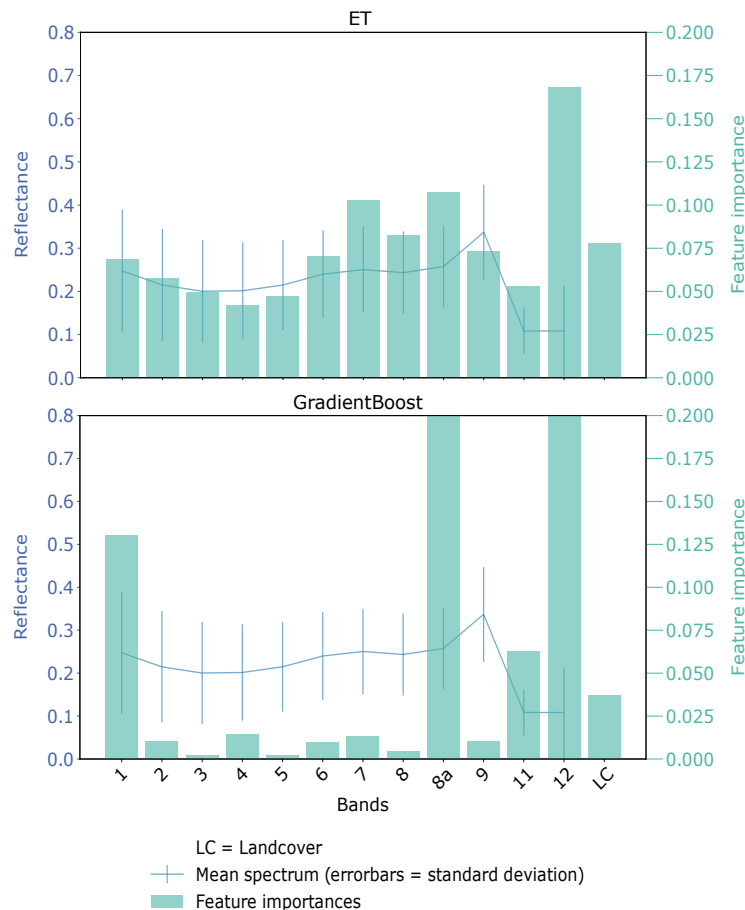


Figure 3.7.: Exemplary feature importances for Extremely Randomized Tree (ET) (top) and Gradient Boosting (GradientBoost) (bottom). Reprinted from [14].

Feature Importance Figure 3.7 shows the feature importance of two ensemble approaches, ET and GradientBoost, exemplary. As for ET, the Sentinel-2 Band 12 is the most important feature, followed by Band 8A and Band 8. The additional land cover feature is the fifth important one in this case. The other remaining Sentinel-2 features are medium important. For GradientBoost, the feature importance is more clearly ranked. The

Sentinel-2 Bands 12 and 8a are the most important ones, followed by Band 1, covering the SWIR region and the land cover information.

Application The top-performing classification models, ET and 1D-CNN, are tested on an independent dataset, a regional area in **central Spain (III)**. 1D-CNN outperforms ET across all metrics, achieving an overall accuracy of 99.8%. ET scores 99.6% (Table 3.3). Visualized results of both models accurately display burned areas within defined boundaries, although 1D-CNN's mapping accuracy is higher (Figure 3.8). Additionally, both models correctly classify *Fire* areas, although they slightly overestimate *Fire* class presence compared to the reference data.

Table 3.3.: Classification metrics of Extremely Randomized Tree (ET) and the one-dimensional Convolutional Neural Network (1D-CNN) for comparison on the independent regional dataset of **central Spain (III)** in %. Reprinted from [14].

Model	OA	κ	F1	Prec	AA	BA
ET	99.6	79.1	93.7	94.3	93.4	82.3
1D-CNN	99.8	83.2	95.0	95.4	94.9	91.0

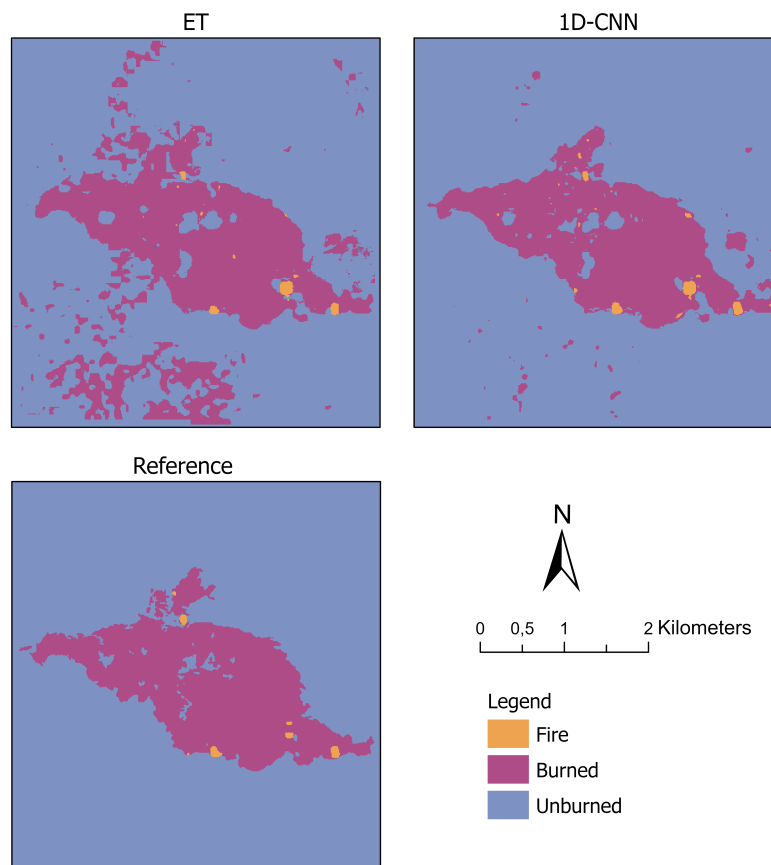


Figure 3.8.: Visualization of the classification results of the Extremely Randomized Tree (ET) (top left) and the one-dimensional Convolutional Neural Network (1D-CNN) (top right) and reference data (bottom) on the independent test region in **central Spain (III)**. Projection: Transverse Mercator. Reprinted from [14].

3.1.5 Discussion

Supervised ML models require precise reference data for fire and burned area detection using Sentinel-2 data for training and testing. These are obtained through a semi-automated process involving carefully selected national agencies vector data and Sentinel-2 data. The accuracy of the classification results is tied to the quality of the employed reference data. In our visual evaluation concerning the study's generated reference data, we find that the used reference data are feasible for the underlying classification task. Overall, we notice that some supervised ML models classify the three classes *Fire*, *Unburned*, and *Burned* better than other models. Although all models achieve high OA scores with more than 87%, few models are outstanding with an OA score above 97%, such as ET and 1D-CNN referring to Table 3.1. ET represents a shallow learning ensemble approach, and 1D-CNN is a deep learning approach. When selecting the appropriate ML model, we suggest applying shallow learning approaches such as ET since they require less computation time and are relatively simple to train.

Concerning the various input features, the spectral information of the Sentinel-2 data combined with information about the underlying land cover represents the basis for the detection of fires and burned areas. For example, the spectral features are the most important for fire detection, while the land cover information indicates the distinction between burned and unburned areas. In conclusion, especially apparent in the GradientBoost, the SWIR bands and the land cover are the main important features. These features are also used for the active fire index calculation and generally for fire and burned area detection (e.g., [114]). We can conclude that the applied input features are sufficient to solve the underlying classification task with supervised ML models.

The results demonstrate that the classification of fires and burned/unburned areas can be performed well by all applied models. However, ET and 1D-CNN perform better overall and in class-wise evaluation than all other models. It is further demonstrated that good results can be achieved for the underrepresented *Fire* class applying undersampling. This class is slightly overestimated. However, overestimating this class is preferred considering the potential dangers that could arise if this class would be underestimated in wildfire management.

As the number of datapoints per class is comparatively balanced due to undersampling, balanced accuracy scores are high. Models achieve high and similar classification results across different training and test subsets. This confirms that there are sufficient datapoints in each subset to solve the classification task. Furthermore, the choice of subsets is less relevant than the selection of an appropriate ML model. The ET and 1D-CNN models, evaluated on an independent dataset of a wildfire in Spain, show strong classification performance, particularly the 1D-CNN. Small misclassifications based on unknown underlying land cover classes occur in both models. The 1D-CNN generates a much smoother result due to its low-level feature derivation.

When evaluating the models' performances on the entirely independent test dataset (Test III), we have to consider the different metrics in addition to the OA. According to the OA scores, both models perform well, but the scores of the additional metrics decrease. The comparatively low BA score indicates, for example, that the lower number of datapoints in the *Fire* class affects the models' performances. This becomes apparent especially on an independent dataset with land cover varying compared to the training dataset.

Therefore, the developed approach is applicable for a generic combined fire and burned area detection compared to existing approaches that aim either at fire detection (e.g., [228, 117]) or burned area detection (e.g., [109]). Additionally, the developed approach is based on high-resolution remote sensing data of 10 m compared to existing approaches based on low-resolution remote sensing data like the Moderate-resolution Imaging Spectroradiometer data (e.g., [116, 229]).

3.1.6 Conclusion and Integration in Framework

Overall Conclusion In this study, a combined fire and burned area detection approach using supervised ML models and Sentinel-2 satellite images is proposed, developed and implemented. The approach highly benefits from Sentinel-2's high spatial resolution and own suitable reference data generated using authoritative data. Undersampling is applied to enhance the classification of the *Fire* class. Tested models, especially 1D-CNN and ET, achieve excellent classification results. The models' generalization capabilities are demonstrated and found to be good on an independent dataset. Our presented methodological approach can be considered a first approach towards a combined detection of fires and burned areas.

Limitations and Outlook The approach could be further enhanced by considering reference data validated on the ground, additional training datapoints, and oversampling instead of undersampling. Furthermore, cloud coverage and non-commercial, high-resolution satellites' overpass time not always allow natural hazard area estimation with remote sensing data in (near) real-time. Therefore, the integration with VGI data can be valuable.

Framework Integration Beyond its immediate focus on wildfire hazards, our developed methodology carries implications for the impact area estimation for natural hazards in general. Characteristics between different hazards vary a lot and need to be investigated with various remote sensors (compare Section 2.1.1). However, methodologies using RS data in general are a suitable tool for natural hazard impact area estimation. The developed integration of machine learning models and reference data generation, as presented for wildfire hazards, can serve as a solid basis for methodologies adapted to other hazard types like floods, landslides, and earthquakes. It highlights the relevance of integrating RS data into the larger context of natural hazard management. Overall, the approach demonstrates

that natural hazard area estimation with RS data is accurate and valuable. The hazard impact zone from RS data represents areas where impacts of hazards on road network could be occurring. Spatial alignment of the extracted hazard zone with the road network can be used for the estimation of the impacts on roads in a next step, described in detail in Section 4.3.2.

3.2 Natural Hazard Impact Zone Estimation with Volunteered Geographic Information Data

VGI data offer valuable real-time insights into hazards, which can be used for natural hazard impact estimation. VGI data, can be viewed as data to bridge the gap in information until RS data becomes available for natural hazard analysis. On the other hand, VGI provides additional information compared to RS data, such as more specific information available in the texts. Moreover, VGI can highlight areas affected by natural hazards where humans are predominantly impacted. These area information can be more valuable for rescue services than simply identifying the location of the hazard. Therefore, it can also be a complementary source of information compared to RS data.

Furthermore, VGI can provide valuable benefits for the accurate mapping of certain hazard extents that can not, or only insufficiently, be mapped from RS data, due to, e.g., cloud cover or infrequent overpass times of satellites. However, the unique characteristics of each type of natural hazard pose distinct challenges. Therefore, different hazard types need specified methodologies for accurate area estimation from VGI, similarly to the accurate estimation from RS data (compare Section 3.1). Once again, the investigation focuses on wildfire area estimation using VGI data. Additionally, the focus lies also on TC impact area estimation, as TCs are complex natural hazards that involve rapidly changing conditions. Moreover, RS for TC analysis might be often hindered by cloud cover. Thus, it does not allow impact estimation during or shortly after the hazard, but rather damage assessment after the hazard (compare Section 2.1.1).

This section explores the possibilities for the application of VGI data for the estimation of the impact zones of natural hazards. The objective is to estimate the areas most likely being affected from the hazard based on the VGI data and therefore most likely impacting underlying road network.

3.2.1 Introduction

This section evaluates the utility of VGI in the form of tweets for spatial analysis of natural hazards in the absence of, or in addition to, RS data. The lack of RS data can occur from either the temporal unavailability of such data due to satellite overpass times or because the hazard's characteristics make it impossible to detect through RS data (compare Section 2.1.1). Though many data sources exist in the category of VGI data, we focus on Twitter (now X) data. So-called tweets that often provide georeferenced, concise messages are a valuable source for information extraction (e.g., [22, 23, 24]). To investigate whether or not VGI data can be a relevant information source for natural hazard estimation, we apply spatial analysis techniques. We evaluate the contributions and limitations of such data source to estimate the impact zone of a natural hazard from the given VGI data. Most realized studies do not consider using VGI data for spatial analysis like natural hazard estimation (compare Section 2.1.1). The main reason for this clear distinction is that analyzing these data in a spatial context can yield precise information about natural hazard extents. In contrast, detecting the occurrence of such (event detection) or general information extraction from the text (information retrieval) only yields approximate hazard locations.

The task of spatial analysis of natural hazards includes two major aspects that we address:

- *Spatial Hazard Estimation (Impact Zone Estimation)*: First, we investigate whether or not and in which accuracy range we can estimate a natural hazard impact zone from Twitter data. The employment of VGI data includes several challenges as location accuracy and location correlation. Furthermore, the availability of VGI data and their location is heavily dependent on other factors, e.g., population density. We, therefore, investigate and evaluate the influence of such factors on the feasibility of our spatial analysis approach.
- *Temporal Hazard Estimation (Development Estimation)*: Secondly, the temporal aspect plays a role in several natural hazard scenarios. For example, TCs are very agile natural hazards with a fast movement rate compared to hazards with lower degrees of temporal development like floods or wildfires. In such a scenario, it is of particular interest to estimate the development of the natural hazard for a prospective time step. Information already available from earlier time steps is used. We analyze the feasibility of TC track estimation in an application scenario including a temporal component. Fortunately, Twitter data include the posting time, which can be evaluated for the task.

Different approaches are eligible to solve the task of VGI data spatial analysis for natural hazard estimation. The choice of spatial analysis technique is based on the hazard type and its characteristics. Two natural hazard types are investigated representatively. These are wildfire hazards and TC hazards.

First, the development of a methodology to estimate natural hazard impact areas of hazards with low degrees of temporal development like wildfires, in the following called *stationary*, is being emphasized. The section addresses the challenges of VGI data usage for natural hazard estimation through two major approaches:

1. estimating an approximate barycenter location of the hazard through factor weighting of tweet locations, and
2. estimating the approximate hazard location and the human-affected hazard location through combining several different methods that scan text for helpful information.

Supplementary data, e.g., population density information, from various open-source data providers, e.g, the worldpop organisation, are integrated to account for the influences of sociodemographic and geographical factors on tweet occurrence. Figure 3.9 shows our applied framework structured into different levels. First, the data are described in the dataset level covering the exemplary employed study regions **Camp (IV)**, **Landiras (V)** and **Var (VI)** fires as described in Section 2.2 and the extracted input datasets (Section 3.2.2). On the data level, the generated datasets are pre-processed. The generated dataset is described next, including the extracted contextual information. Finally, methods for the approximate barycenter estimation and approximate hazard location estimation are stated in Section 3.2.3 as included in the method level of the framework.

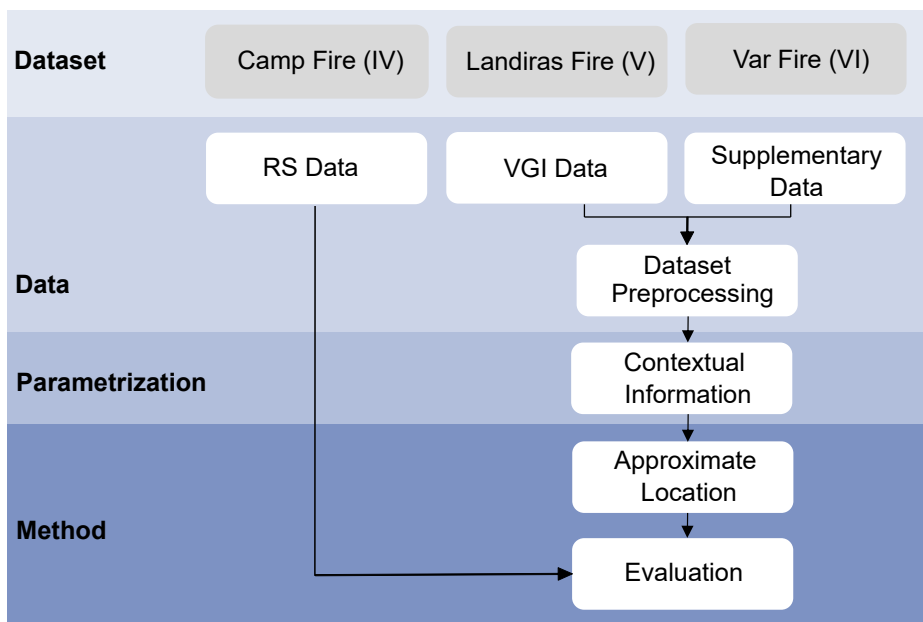


Figure 3.9.: Visualization of the framework for natural hazard impact zone estimation from Volunteered Geographic Information (VGI) for *stationary* hazards, representatively for wildfire scenarios. The following abbreviation is used: RS - Remote Sensing.

Secondly, the development of a methodology to estimate natural hazard impact areas of hazards with higher degrees of temporal development, like TCs, is being emphasized. These are in the following called *moving* hazards. For the development of an intuitive but suitable methodology for the estimation of these *moving* hazards, the methodology first focuses on the estimation of TCs in a *stationary* setting. Only then, the methodology is transferred to *moving* TCs by looking at specified time periods to include the characteristic temporal change of *moving* hazards. For this estimation methodology, the applicability of a regression model to estimate the distance from VGI datapoints to the natural hazard extent is investigated. Figure 3.10 shows our applied regression framework structured into different levels. First, the data are described in the dataset level covering the exemplary examined hazard scenarios **Irma (VII)** and **Ida (VIII)** as described in Section 2.2 and the extracted input datasets (Section 3.2.2). The generated dataset is described in Section 3.2.3, including the reference generation in the feature level in Figure 3.10. On the data level, the generated datasets are processed and split, which is necessary for the regression’s training and evaluation. The selected regression models, their optimization, and the model evaluation metrics included in the model level of the framework are presented in Section 3.2.3.

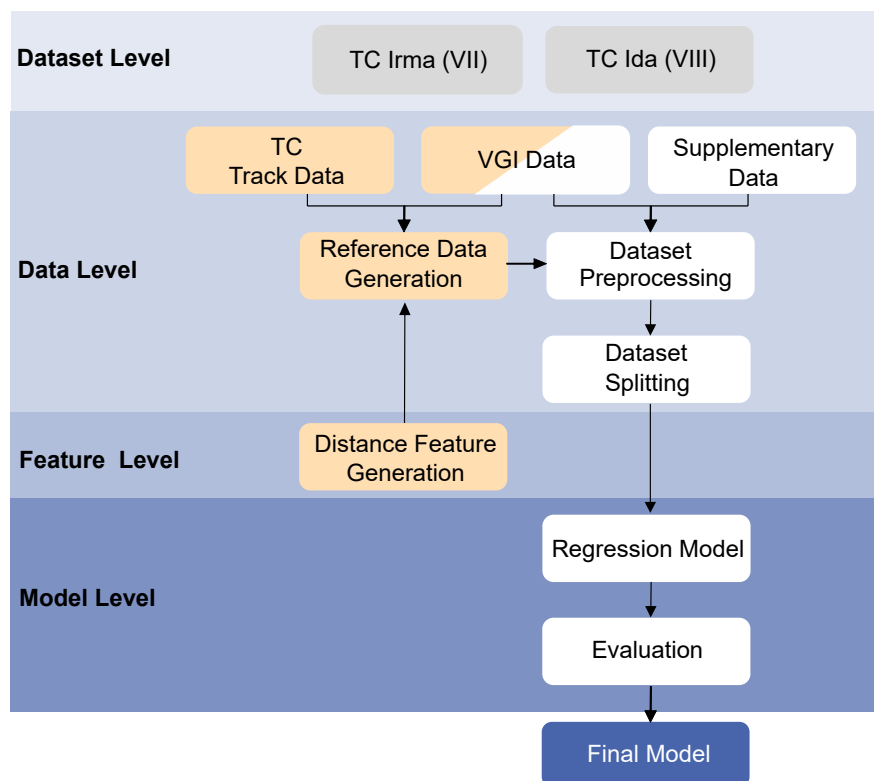


Figure 3.10.: Visualization of the regression framework for natural hazard impact zone estimation from Volunteered Geographic Information (VGI) for *moving* hazards, representatively for tropical cyclone (TC) scenarios divided into the data level, the feature level, and the model level. Orange: Components associated with the reference data generation phase within the framework. Adapted from [44].

3.2.2 Data

Selected Application Scenarios Two natural hazard types are investigated representatively, for *stationary* and *moving* hazards. This variety in hazards illustrates the applicability of VGI data for hazard impact assessments on the one hand. On the other hand, the transferability of using VGI data, which can be employed for various types of hazards is demonstrated.

This work relies on different application scenarios of fire hazards that occurred in CA, US, and France in the past years. These are the following fires: **Camp (IV)** fire near Paradise in 2018 (CA), and the fires near **Landiras (V)** in 2022, and **Var (VI)** in 2021 (France). These study areas are chosen considering their different constellations of parameters, as explained in Table 3.4, to show the possibilities and limitations of the developed methodology. Fire characteristics, like the fire's size and spreading rate, are considered since it influences the amount and dynamics of available tweets. Furthermore, general factors that influence VGI occurrence, like land cover information, population density, general tweet behavior, and whether agencies like firefighters or road security agencies use VGI as a medium to spread the news, are considered. Figure 3.11 (top and middle) visualizes the locations of the fires.

Furthermore, two exemplary TCs in the region of mainland US are chosen as application scenario hazards. The considered TCs are TCs **Ida (VII)** 2021 and **Irma (VIII)** 2017. TC **Ida** formed on August 26, 2021, and dissipated on September 4, 2021. It made landfall on the US coast in Louisiana on August 29, 2021. TC **Ida** caused destruction in many states of the US. It became the second-most damaging and intense TC to strike the US state of Louisiana on record, behind TC Katrina [230]. TC **Irma** formed on August 30, 2017, and made its first landfall on Cudjoe Key, Florida, US, on September 10, prior to another landfall on Marco Island, Florida, the same day. It dissipated on September 13, 2017, and became the sixth costliest US Atlantic TC [230]. Figure 3.11 (bottom) visualizes the locations and extent of the TCs.

Datasets The first datasets used for the natural hazard area estimation with VGI data are the **Camp (IV)** fire, and the fires near **Landiras (V)** and **Var (VI)** described in Section 2.2. These are used as datasets for the development of a methodology for the natural hazard area estimation with VGI for *stationary* hazards. Secondly, for the development of a methodology for the natural hazard area estimation with VGI for *moving* hazards, the used datasets are the TC **Ida (VIII)** and **Irma (VII)** described in Section 2.2.

This study uses Twitter data as VGI to exploit its high usage and accessibility. The selected Twitter data are obtained through Twitter's download API accessed via Python. The direct location extraction method (compare Section 2.1.1) obtains the most accurate locations from the tweet metadata.

Table 3.4.: Overview of fire characteristics and characteristics influencing VGI data regarding the three scenario areas for fire impact estimation. Adapted from [1].

Fire	Camp Fire, California	Landiras, France	Var, France
Fire Starting Date	08/11/2018	12/07/2022	16/08/2021
Fire Duration	-25/11/2018 (17 days)	-25/07/2022 (13 days)	-26/08/2021 (10 days)
Total Fire Area	~620 km ²	~138 km ²	~57 km ²
Fire Behaviour	620 km ² within 3 days, spreading extremely quickly, but then remaining within almost these same boundaries until it is extinct	+/- constant spreading	57 km ² within 22 hours, spreading very quickly but then remaining within these same boundaries until it is extinct
Landcover	Shrub landcover, mountainous, few populations overall, but one town	Woodland/forest landcover, flat-hilly, few population	Forest/shrub landcover, hilly, few population
Population Density/Distribution	Low density, irregular distribution around and INSIDE possible fire area	Low density, irregular distribution around possible fire area	Low density, regular distribution around possible fire area
Tweet Behavior	Less tweets, less place information in text	Less tweets, more place information in text	Less tweets, more place information in text
Agencies (Fire/Road)	Using twitter	Not using twitter	Not using twitter
First Available Remote Sensing Data	3 days after fire start (11/11/2018)	5 days after fire start (17/07/2022)	1 day after fire start (17/08/2021)

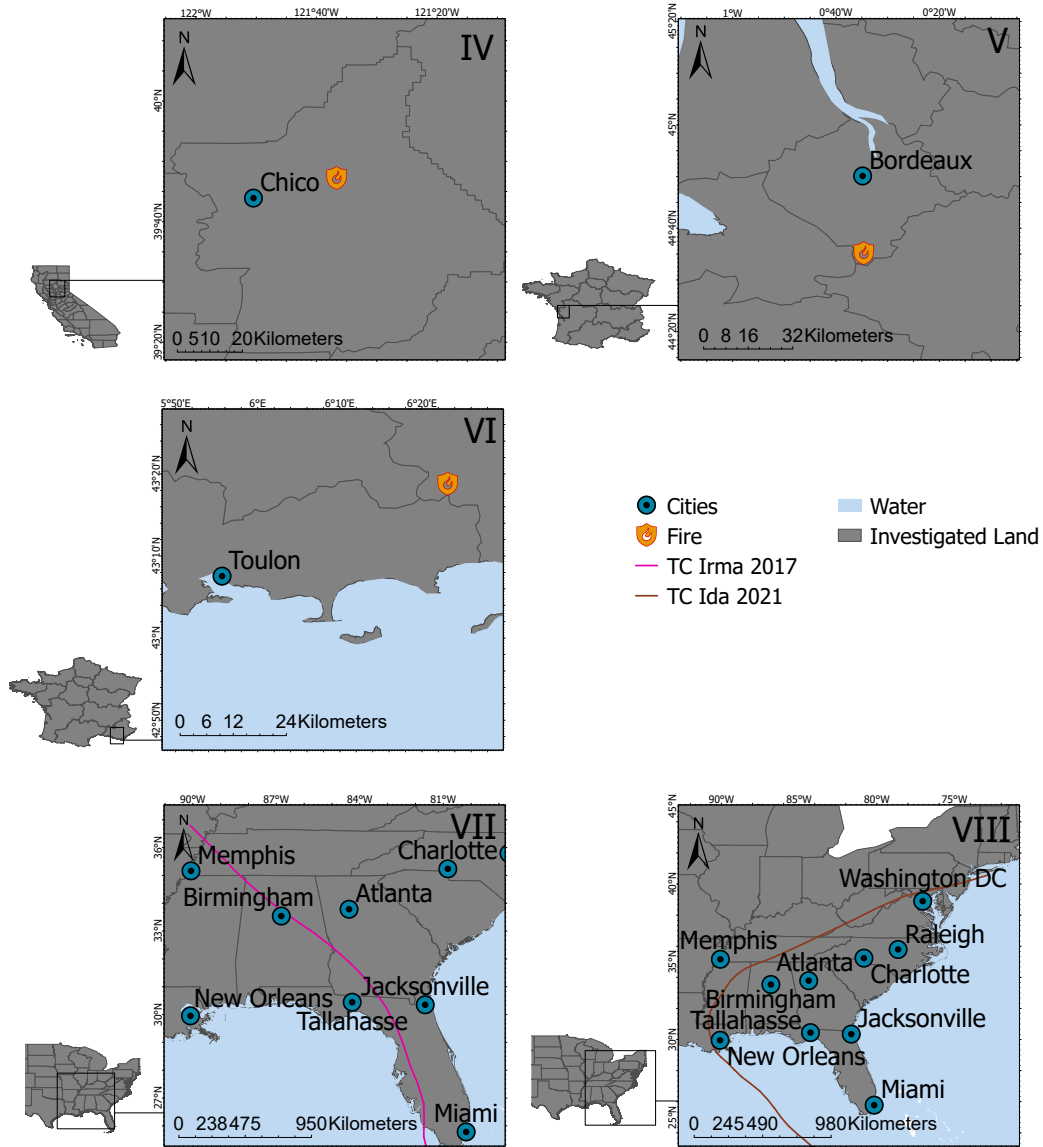


Figure 3.11.: Overview of cases study hazard locations and respective hazard types: **Camp (IV)**, **Landiras (V)** and **Var (VI)** fires, **Ida (VII)** and **Irma (VIII)** tropical cyclones (TCs). Data basis: © 2018 GADM. Projection: WGS84.

Table 3.5.: Overview of numbers (#) of extracted tweet data for *stationary* and *moving* hazards. The following abbreviations are used: coord. - coordinates.

Hazard	Camp (IV)	Landiras (V)	Var (VI)	Irma (VII)	Ida (VIII)
Tweet dates	08/11/2018- 10/11/2018	12/07/2022- 16/07/2022	16/08/2021- 17/08/2021	10/09/2017- 13/09/2017	28/08/2021- 02/09/2021
# of tweets with coord.	52	0	3	1375	1332
# of tweets with place	157	30	82	not used	not used

Only a limited number of tweets contain the `coordinates` information. In addition, the `place` field also contributes to the hazard location estimation, although with lower accuracy. Tweets with a filled `place` field are still helpful as they contain textual information about affected areas. Tweets that contain keywords like the hazards name or type and happen during the hazard time in a specified approximate hazard zone are pulled from the API. Tweet text, date and time, and location are extracted for each hazard scenario. Table 3.5 displays the number of tweet data extracted per application scenario for the *stationary* hazard investigation. We differentiate between tweets with `coordinates` information and `place` information for location information. For the analysis of *stationary* hazards both location types are used, due to the generally low number of available data. However, we employ only the `coordinates` given in the metadata to achieve the highest possible accuracy for the regression task of the *moving* hazards.

The supplementary data are pulled or derived from different OSM and non-OSM sources, as displayed in Table 3.6. In our case, the supplementary data are population density, altitude, slope, aspect, distance to the nearest road, Digital Divide Index (DDI) [231], and landcover for the investigation areas. A systematic relationship between population density and Twitter use has been reported by Arthur et al. [232]. Altitude and slope are additional factors influencing tweet density and may have interaction effects with population density. By including them separately, we allow the model to capture potential non-linear relationships or interactions that might be missed when they are combined in a single feature.

Slope and aspect (orientation of slope, measured clockwise in degrees from 0 to 360) are calculated based on the altitude using ArcGIS [233]. Aspect can influence temperature, vegetation, and potentially the desirability of locations for various activities, which may, in turn, be related to tweet density. The distance to the nearest road can also influence tweet density through more people mostly staying near roads and not staying in entirely secluded regions. The distance is calculated from an OSM road feature dataset using the software ArcGIS [233]. The DDI [234] is an index that measures the physical access and adoption of broadband infrastructure and the socioeconomic characteristics that limit their use. It comprises two scores: the infrastructure/adoption and the socioeconomic scores.

Table 3.6.: Supplementary data with their sources and years of creation. The following abbreviations are used: CGIAR SRTM - Consultative Group on International Agricultural Research, Shuttle Radar Topography Mission; DDI - Digital Divide Index; CGLS-LC100 - Copernicus Global Land Cover Layers. Reprinted from [44].

Data	Data Source	Year
Population Density	worldpop.org [236]	2020
Altitude	Hijmans [237] - CGIAR SRTM (3 seconds resolution)	2018
Slope	Derived from altitude	2018
Aspect	Derived from altitude	2018
Distance to nearest road	Hijmans [237] - Digital Chart of the World	independent
DDI	Gallardo [234]	2019
Landcover	CGLS-LC100 Collection 3 [202]	2019

The added supplementary data are included as they can be more explanatory for the occurrence of tweet points itself. For example, more VGI data occur in areas with higher population density. Different data affecting tweet data, e.g., population data, have been investigated in several studies [235, 22]. For distinct hazards and methodologies, distinct supplementary datasets must be employed for the weighting of influencing factors on tweet occurrence.

Finally, the utilization of hazard information data that serve as (pseudo-) reference is crucial. These data are considered as so-called 'known' hazard data. These are necessary for both training and testing of supervised approaches and the evaluation of unsupervised estimation approaches from VGI. Pseudo-reference data are hazard areas extracted from Sentinel-2 RS for the fire application scenarios. The most temporally proximate available RS images to the start of the fire (as listed in Table 3.4) are extracted for the application scenarios. As suitable non cloud-obstructed Sentinel-2 data are not available for one application scenario, we rely on California Department of Forestry and Fire Protection (CalFire) agency data in this case. These data are provided in vector files, showing the extent of a fire area.

Reference data are TC track data provided by weather services for the TC application scenarios. These are vector data that provide the calculated best track of the TC (compare Figure 3.11). It is usually generated after the season when forecasters gather all the available information from different sources and datasets [238]. These data are available, from the responsible weather services, e.g., the National Hurricane Center (NHC) for our application scenario hazards. Furthermore, to evaluate the temporal aspect of the TC development, we need information on the time-dependent location of the TC. We use the NHC's Tropical Cyclone Public Advisories (TCPA) [239] to extract information about when the TC eye passed at which location. The TCPA are issued every six hours and provide the actual TC eye geographic location-specific time. We employ these data to differentiate between tweets that occur during a hazard and those that are posted after a hazard has

taken place at a specific location and time. We choose the respective geolocations day-wise for our analysis of the temporal aspect of TC track estimation.

3.2.3 Methodology

Considering the different characteristics of the two varying hazard scenarios *stationary* and *moving* and the different requirements for an impact area estimation using VGI, two separate methodologies are developed for these hazards, representatively.

Stationary Hazards Methods

In this section, the two primary method types for stationary hazard impact zone approximation are explained. These are approximate barycenter calculation and approximate location estimation from tweet datapoints. For these methodologies landcover and population density datasets are used as supplementary data. Figure 3.12 displays the methods overview.

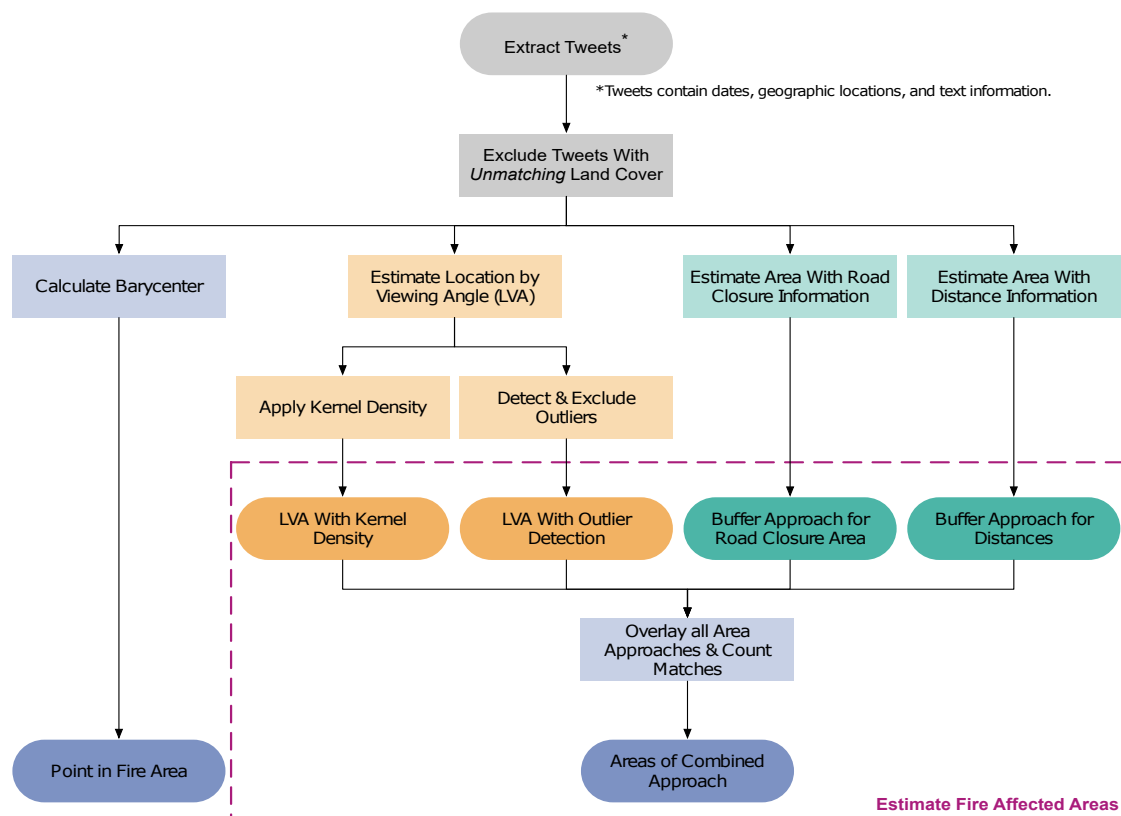


Figure 3.12.: Methodology overview for approximating fire-affected areas based on Twitter data. Reprinted from [43].

Approximation of the Barycenter When evaluating the tweet data in a geospatial manner, we first calculate the weighted barycenter location of the tweet points, considering the influencing factors. Utilizing population density and land cover as weighting factors for barycenter approximation offers significant advantages:

- Population Density: More people in an area means a higher probability of someone witnessing and reporting a wildfire.
- Land Cover: Land cover diversity impacts the visibility and detectability of wildfires and fire propagation.

The geospatial barycenter is calculated as follows:

$$\bar{X}_w = \frac{\sum_{i=1}^n x_i \cdot w_i}{\sum_{i=1}^n w_i}, \bar{Y}_w = \frac{\sum_{i=1}^n y_i \cdot w_i}{\sum_{i=1}^n w_i} \quad (3.2)$$

where $\text{dens}_{\text{tweet}}$ is the point density per tweet calculated by kernel density from all the tweets. dens_{pop} is the population density according to WorldPop.org at the point location. w_{landcov} is a custom weight depending on the underlying landcover type at the point for each point i .

$$w_i = \log\left(\frac{\text{dens}_{\text{tweet},i}}{\text{dens}_{\text{pop},i}}\right) + w_{\text{landcov},i} \quad (3.3)$$

where $\text{dens}_{\text{tweet}}$ is the point density per tweet calculated by kernel density from all the tweets, dens_{pop} is the population density according to WorldPop.org at the point location, and w_{landcov} is a custom weight depending on the underlying landcover type at the point for each point i . Highly combustible landcover types like shrubs or forest have a higher weight. These are more likely for a fire to burn and continue to burn to an area with such landcover, compared to, e.g., a water landcover area.

Approximation of the areal location Next, we estimate approximate hazard locations or affected areas with several methods according to the availability of the respective data in the tweet texts. These include the viewing angle of the fire by mentioned places in the text (1), road segment blocking information (2), and distance to the fire information (3). Figure 3.13 displays exemplary tweet text snippets containing the relevant information for the employed methods.

1. We approximate the hazard location by considering names of places that are mentioned in the tweets' texts talking about the respective hazard (see Figure 3.13, (1)). This method is therefore referred to as the *Location by Viewing Angle* (Location by Viewing Angle (LVA)) approach. We extract these mentioned places with two approaches: NER or pattern recognition by RegEx (e.g., [240, 241, 242]), which are NLP methods. For NER, we employ the Spacy Python library [243], an open-source NLP library. We use it to detect of the entities GPE (Geopolitical Entities: Countries,

cities, states) and LOC (Non-GPE locations, mountain ranges, bodies of water). We apply RegEx in addition to NER, as NER recognizes general location places, while we can extract more specific areas with RegEx. For RegEx, we employ our own developed algorithm, which consists of the two steps of name detection and geoparsing. It searches for spatial places like *Mt. Wilson* or *Monrovia Peak*, employing word search (e.g., *Peak*). Furthermore, it uses RegEx patterns that search for associated nouns (e.g., *Monrovia*). After extracting place names, we geoparse, which converts text descriptions of places into geographic identifiers like coordinates. Next, we apply a methodology to check for the viewing angle. The people might not see mentioned places in their tweet locations, as obstructions like mountains could prevent them. Therefore, we check the plausibility of the viewing angle by considering the occurrence of viewing obstructions in the line of sight from the location to the mentioned place. As a result, we obtain locations to which the speaker can view, and which are probable that he is seeing the hazard there. With the obtained points, we conduct two separate methods again to get more independent results. These are in line with the principle that where more people think the hazard is there, the hazard is more likely to be there. These are:

- *Kernel density estimation on viewing angle points*: Based on the resulting points of 1., we conduct kernel density estimation as implemented in ArcGIS [233]. It places a kernel (smooth, continuous function) on each datapoint and sums these kernels to create a smooth representation of the underlying probability distribution. We extract areas with a specific density and a higher probability of the hazard's presence within those areas.
- *Non-outlier estimation on viewing angle points*: We use an Isolation Forest, implemented in ArcGIS [233] to detect non-outlier points. It works by isolating instances using binary splits and constructing an ensemble of decision trees. Outliers are identified as instances that require fewer splits to be isolated. We then calculate a convex hull spanned by non-outlier points in the following.




- (1)  I can see the flames over **Mt. Wilson** from my house.
- (2)  The road is closed on **WB37 between Atherton Ave and US101**.
- (3)  We are **five miles** away from the fire.

Figure 3.13.: Exemplary tweet text snippets from which information about approximate areal locations of natural hazards can be extracted: (1) Named places, (2) Road closure information, (3) Distance information. The relevant text information that is considered is marked in **bold**. Texts are simplified and adapted from original extracted tweet texts. Reprinted from [43].

2. In this step, we consider blocked road information (see Figure 3.13, (2)). Road authorities often post information about such in emergency or hazard cases. We search tweets mentioning such information or posted by responsible agencies and extract their locations. From this information, we extract the exact road locations via RegEx implemented for roads (compare Section 3.3). We geoparse and obtain points of blocked road information, mainly two road intersection information per tweet (e.g., *Angeles Crest Hwy & Upper Big Tujunga Rd*). We can then extract the closed road segments between those two mentioned points and the area they are spanning which most probable corresponds to the hazard area.
3. Finally, we consider distance information in the texts (see Figure 3.13, (3)). We search tweets mentioning distance information and buffer their location with the this specific distance. We obtain a circle on which the hazard seen by the speaker might lie. To account for coarse estimates by speakers, we apply a buffer around this circle with a distance of 30 % of the initial space. This assumption is based on the idea that people tend to gauge distances more accurately when hazards are in closer proximity to them. Furthermore, we limit the buffer areas by landcover plausibility, e.g., a buffered area is not considered if overlapping a landcover area that is not plausible to contain fire, e.g., water or bare rock.

With the above methodological approaches, we consequently obtain approximations of areas that could be or are perceived by tweet text speakers as hazardous areas. Then, we cross-check all the results from these methods with land cover plausibility (areas in certain landcover areas are more likely combustible; see above). Finally, we combine the single estimation method results to estimate the fire's minimal and maximal possible affected area with a confidence interval.

Additionally, using pseudo-reference data for approach evaluation (testing for supervised approaches, comparison for unsupervised approaches) helps to validate the approaches' performance and assess its generalizability to different hazard scenarios. For the evaluation of our methodology, we provide qualitative results in the form of maps. We compare the calculated barycenter and the fire approximation areas with the RS fire extents. We refer to the latter as a pseudo-reference, since the employed RS images are only the most temporally proximate available RS images to the start of the fire. These images do not accurately depict the actual state of the fire at the time when the tweet data were collected (compare Table 3.4 in Section 3.2.2).

Moving Hazards Methods

In this section, the method of location approximation from tweet datapoints for moving hazard impact zones is explained. An unsupervised estimation as employed for stationary hazards is not suitable for moving hazards due to the temporal component in these cases. Since many more supplementary data that are thought to explain the occurrence of tweets have to be considered, a manual weighting scheme is not practical. Therefore, a supervised multivariable regression, taking into account the tweet locations and the supplementary data as features is used. Reference data are incorporated into the training process for the supervised estimation approach. These allow machine learning models to learn the spatial relationships between VGI datapoints and actual hazard occurrences. The target variable to be estimated is the TC track, which represents the hazard's approximate location. However, it can not be estimated directly. Therefore, a substitute variable is used. This variable can easily be used as label for the regression task (→ [Reference Data Generation and Dataset](#)). Furthermore, this section describes the dataset preparation (→ [Dataset Preparation](#)). Two different regression models are tested for the regression task (→ [ML Models](#)). Postprocessing steps are conducted after the regression task (→ [Postprocessing](#)).

Reference Data Generation and Dataset As reference data, known information about the natural hazard is used. In this case, this is the TC track information obtained from weather services. A substitute value should be easily usable for the regression task and represent the spatial information of the TC track. This substitute value is each tweet point's geodesic distance to the nearest TC track point in km (compare [Figure 3.14](#)). This geodesic distance implicitly contains information about the location of the TC track. It serves as the label for the regression model and is the dependent variable estimated by the regression approaches.

A dataset with all datapoints containing the input features and the corresponding labels of the distance from tweet point to TC track is created. In the following, the steps to preprocess the input data to be used as features is summarized: First, the Twitter data locations, which are referred to as datapoints, are preprocessed. Each point possesses its x and y geographical coordinates transformed into Universal Transverse Mercator (UTM) coordinates. These two UTM coordinates are the first two input features for the ML models. Furthermore, we retain the posting time information for the tweets. This information is not used as an input feature but is relevant for the temporal hazard evaluation, especially for partitioning datapoints in during- and post-hazard tweets. Next, we combine the tweets' information with the supplementary data (compare [Table 3.6](#) in [Section 3.2.2](#)). The values of each of the supplementary raster datasets are extracted for each datapoint and added as an additional feature. In conclusion, the **Irma** dataset contains eight features (tweet location x, tweet location y, population density, altitude, slope, aspect, distance to

nearest road, DDI), the distance to TC track label, and the date column for 1375 datapoints, exemplary. The **Ida** dataset is processed accordingly, following the same procedures.

Dataset Preparation The TC track approximation is first investigated in a *stationary* mode to develop and evaluate the regression model’s suitability for the task. It is then being transferred to a *moving* scenario. Figure 3.14 displays the overview of both dataset preparation scenarios.

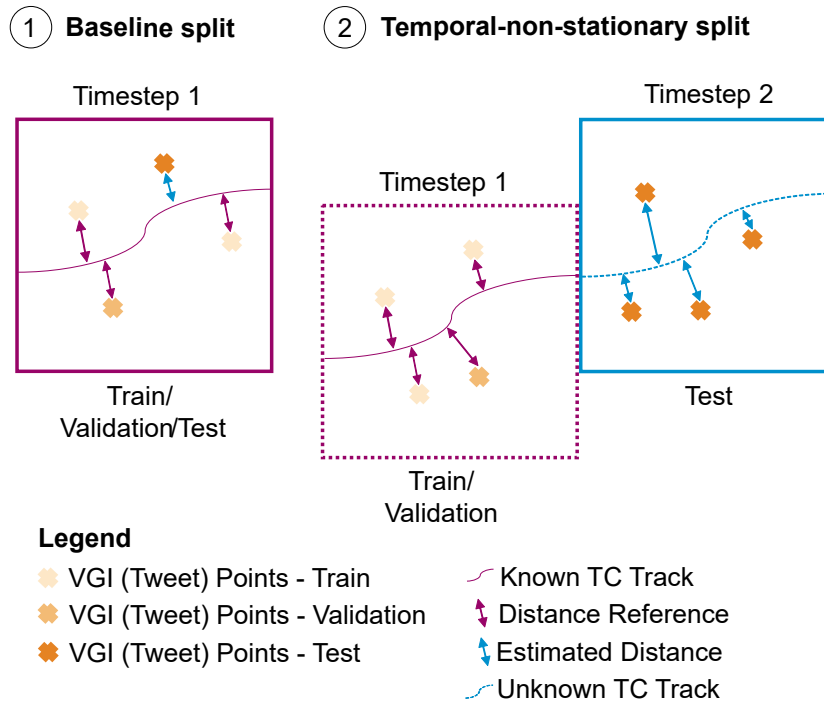


Figure 3.14.: Methodology overview for approximating tropical cyclone (TC)-affected areas based on Twitter data. The following abbreviation is used: VGI - Volunteered Geographic Information.

For the development of the regression model in a stationary setting, we randomly split the TC **Irma** dataset into three sets for training, validation and testing with a ratio of 60 : 20 : 20 (Figure 3.14 (1)). Standard ML guidelines are followed with the chosen split ratio (see, e.g., Kattenborn et al. [208]). The randomized split guarantees an independent distribution of the subsets. The training dataset is reserved for the respective regression model’s training, while the evaluation of the model is conducted on the test dataset. Besides, the model’s hyperparameters (Table A.2 in Appendix B.1) are optimized on the validation dataset. In Figure 3.14 (1) the geodesic distances that serve as label for the regression used in the training and validation phase are depicted in purple. The geodesic distances that are estimated by the regression models in the testing phase are depicted in light blue. This split is referred to as the *baseline (BS) split* in the following.

Finally, we add the temporal component investigating the hazard’s development estimation. For this scenario, the TC **Ida** is used for investigation. A TC moves over a spatially extensive

area at a certain speed, resulting in the fast development of its impact zone. Its evolution leads to some areas being currently impacted in timestep 1 but not in timestep 2 and vice versa. Figure 3.14 (2) displays this scenario. To model such a scenario that should be able to represent an application scenario, we choose the following:

- Considering the movement direction of the TC, we spatially split the area that it overpasses into two parts. One part that will serve as training (timestep 1) contains significantly more datapoints than the other (testing/ timestep 2) part.
- The training dataset comprises all during- and post-disaster tweets in the spatially distinct training part of the spatial area.
- The test dataset comprises the during-disaster tweets in the spatially distinct testing part of the spatial area.

The reference label for the regression equals the geodesic distance from tweet point to known TC track in timestep 1. The geodesic distance is estimated by the regression model for timestep 2, which implicitly contains information about the location of the TC track. This scenario corresponds to a TC's evaluation whose eye has moved over a spatial area used for the models' training and is now located over the testing part. Therefore, only the during-hazard tweets are used for the testing, as post-hazard tweets would not have been created in a real application scenario. We select a major spatial area as training data and a very small area as testing data. The testing area comprises tweet data posted in the area containing half of the city of New York City, hit by TC **Ida**. The training area comprises tweet data posted in the other half of this area and all the datapoints from other tweet data along the TC **Ida** track and along the complete TC **Irma** track, to obtain a maximum of training sample points. Such a spatial split is necessary to allow the models to learn from spatially not very distinct datapoints (New York first half) and estimate in a spatially similar environment (New York second half). Data of the TC **Irma** are included to augment the number of training datapoints. This split is referred to as the *temporal-non-stationary (TN) split* in the following.

ML Models This subsection describes the model level (see Figure 3.10), including the ML models to solve the underlying regression task, as well as their optimization and evaluation. Estimating hurricane tracks from tweet data can be done using regression of the nearest distance from the tweets to the track. Since we have several input features and are trying to depict a rather complex connection with our output label, we need to employ a sophisticated regression approach. Therefore, we apply two different ML models to evaluate their estimation performances on the different splits and datasets.

The study investigates two different machine learning models, ET and Geographically Weighted Regression (GWR), to solve the regression task. ET is applied as a tree-based regression model and is associated with decision trees (DTs). Generally, they include a root and a leaf node linked by branches. During the training of DTs, the data of

the respective dataset are split at every branch. These splits generate subsets, which correlate highly to the input features. However, an ET can only incorporate very different geographical variances by coordinates given as input features. It might not be able to model the local relationships between the coordinates. Therefore, we select GWR as a different approach [244]. GWR considers non-stationary input features by incorporating features within each target value's neighborhood. It can therefore link the local relationships between the features and the label, which makes it especially suitable for geographical applications. The models' hyperparameters are tuned by a grid search for the ET and manually through iterative experimentation using the ArcGIS software for the GWR. Model performance is evaluated using the following metrics, defined in Table A.3 in Appendix B.2: Coefficient of Determination (R^2), Root Mean Squared Error (RMSE), Mean Absolute Error (MAE), and Maximum Error (ME).

Postprocessing For the regression task, the distance from the tweet point to the hurricane track was used as a substitute value to enable the deployment as a data label. Only the distance is estimated from the approach, but no directional information is given. Therefore, trilateration is necessary to obtain the hurricane-impacted zone from the estimated data. We conduct the following steps to obtain the impact zone:

1. Buffer the tweet points with their respective estimated distance.
2. Calculate the intersections of the buffer circles.
3. Calculate the kernel density of the intersection points. This step is based on the assumption that where more of the buffers intersect, the higher the chance that this area is actually a hazard impact zone.

3.2.4 Results

In this section, the results for the estimation of natural hazard impact zones using VGI data are presented. The overall estimation performance of the applied models on stationary hazards like wildfires and moving hazards like TCs will be presented, respectively.

Stationary Hazards Results

The results and their cartographic visualization achieved based on the applied unsupervised combined method presented for each fire case are displayed in Figure 3.15. As mentioned above, the results are compared and overlaid with the RS data generated fire extents as pseudo-reference. For each map, the total number of tweets before the availability of the RS image is included in the approaches. By qualitative analysis, it can be verified that all the resulting maps agree with the RS fire pseudo-reference on a coarse level, while differences are observed on a finer level. Additionally, Table 3.7 displays the deviances

between the approximated barycenter and hazard extends as estimated using the developed methodology.

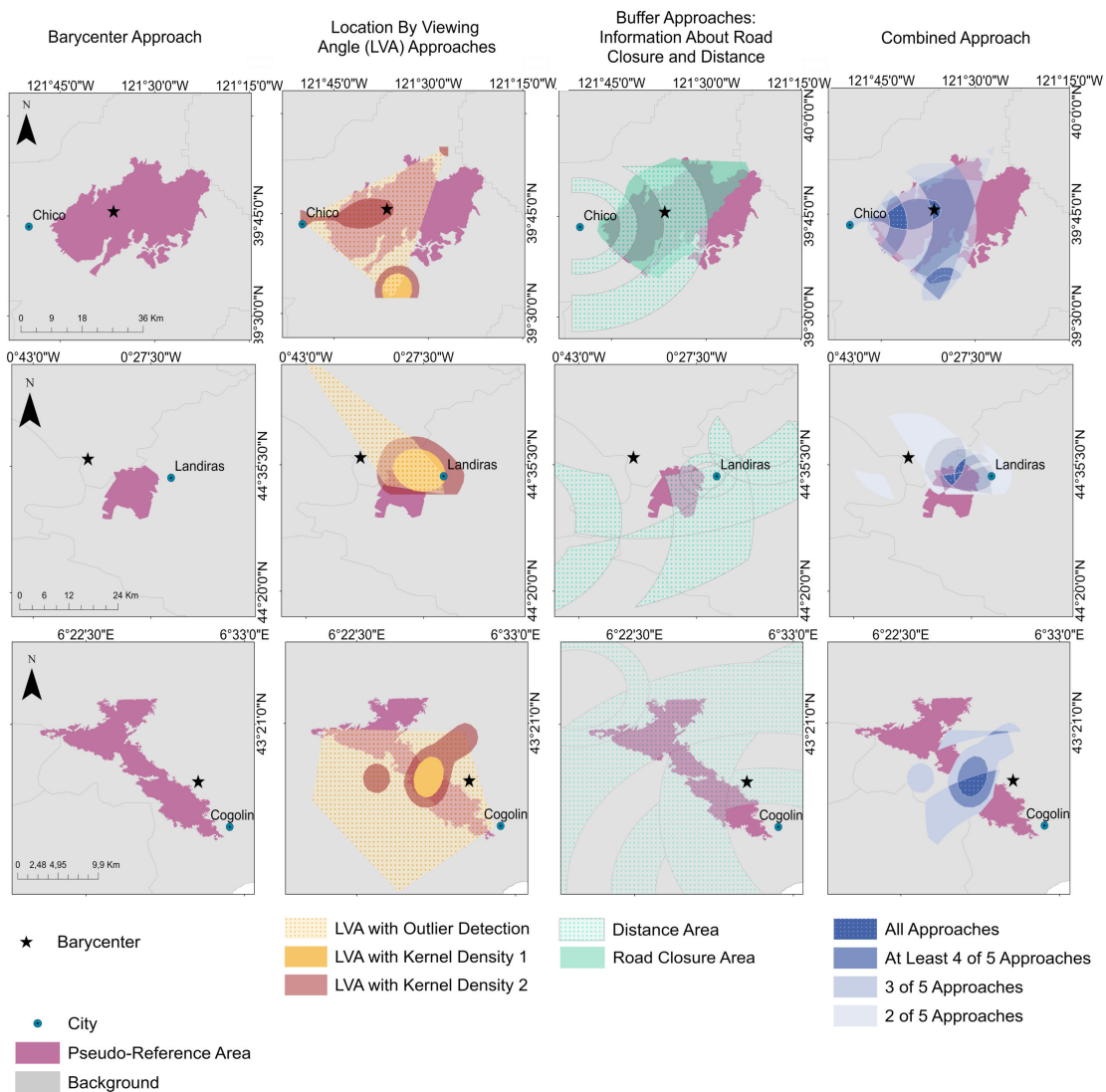


Figure 3.15.: Visualization of the impact zone estimation for the selected fires: the **Camp (IV)** fire near Paradise (row 1), California, and the wildfires near **Landiras (V)** (row 2) and in the **Var (VI)** region (row 3), France. The following abbreviation is used: LVA - Location by Viewing Angle. Data basis: © 2018 GADM. Projection: WGS84. Reprinted from [43].

In the result obtained for the **Camp** fire (IV) (Figure 3.15, row 1), the barycenter (column 1) also corresponds well with the RS fire area. LVA (column 2), distance area, and road closure area (column 3) can be estimated. LVA with outlier detection and distance and road closure area results correspond mostly to the pseudo-reference area but are located in the western part of the RS fire area. LVA with kernel density detects three significant point cluster densities: a small one in the North, one in the South, and one on the axis from

Chico and Paradise. Consequently, the overlaps, as a combination of all applied approaches, (column 4) indicate the estimated area in the western part of the pseudo-reference area and are heterogeneous.

In the result obtained for the **Landiras** fire (V) (Figure 3.15, row 2), the barycenter (column 1) also lies beyond the RS fire area. However, the barycenter still approximates the course affected area. LVA (column 2) and distance area (column 3) can be estimated and correspond primarily with the northern and eastern regions of the fire area, respectively. Consequently, the overlaps of the approaches (column 4) combined show the estimated area in the northern half of the RS fire area.

In the result obtained for the **Var** fire (VI) (Figure 3.15, row 3), the barycenter (column 1) lies beyond the RS fire pseudo-reference. However, given the very distinct shape of the fire area, the barycenter still approximates the course-affected fire area. LVA (column 2) and distance area (column 3) can be estimated and correspond mainly with the central location of the fire area. Consequently, the overlaps of the approaches (column 4) combined show the estimated area in the central part of the RS fire area. The overlaps miss out on the upper and lower part of the very distinct fire area shape.

Table 3.7.: Deviances in km for the wildfire hazard approximation methods: Distances are given between the calculated barycenter and the center of remote sensing (RS) pseudo-reference areas, and the center of the combined approaches area approximation and the center of RS pseudo-reference areas, respectively.

Wildfire	Barycenter Deviance	Area Approximation Deviance
Camp	3 km	4 km
Landiras	10 km	3-4 km
Var	4 km	<2 km

Moving Hazards Results

The selected models on the selected *BS split* trained on datapoints of the TC **Irma** achieve generally high scores. Table 3.8 shows the estimation results of the applied models on the respective test sets. ET model on the baseline split show the best regression results with an R^2 -score of >93%. The GWR produces minor accurate results with an $R^2 = 82\%$. When considering RSME and MAE, the ET model achieves satisfactory regression results between 4 km and 6.5 km. These metrics are much higher for the GWR approach.

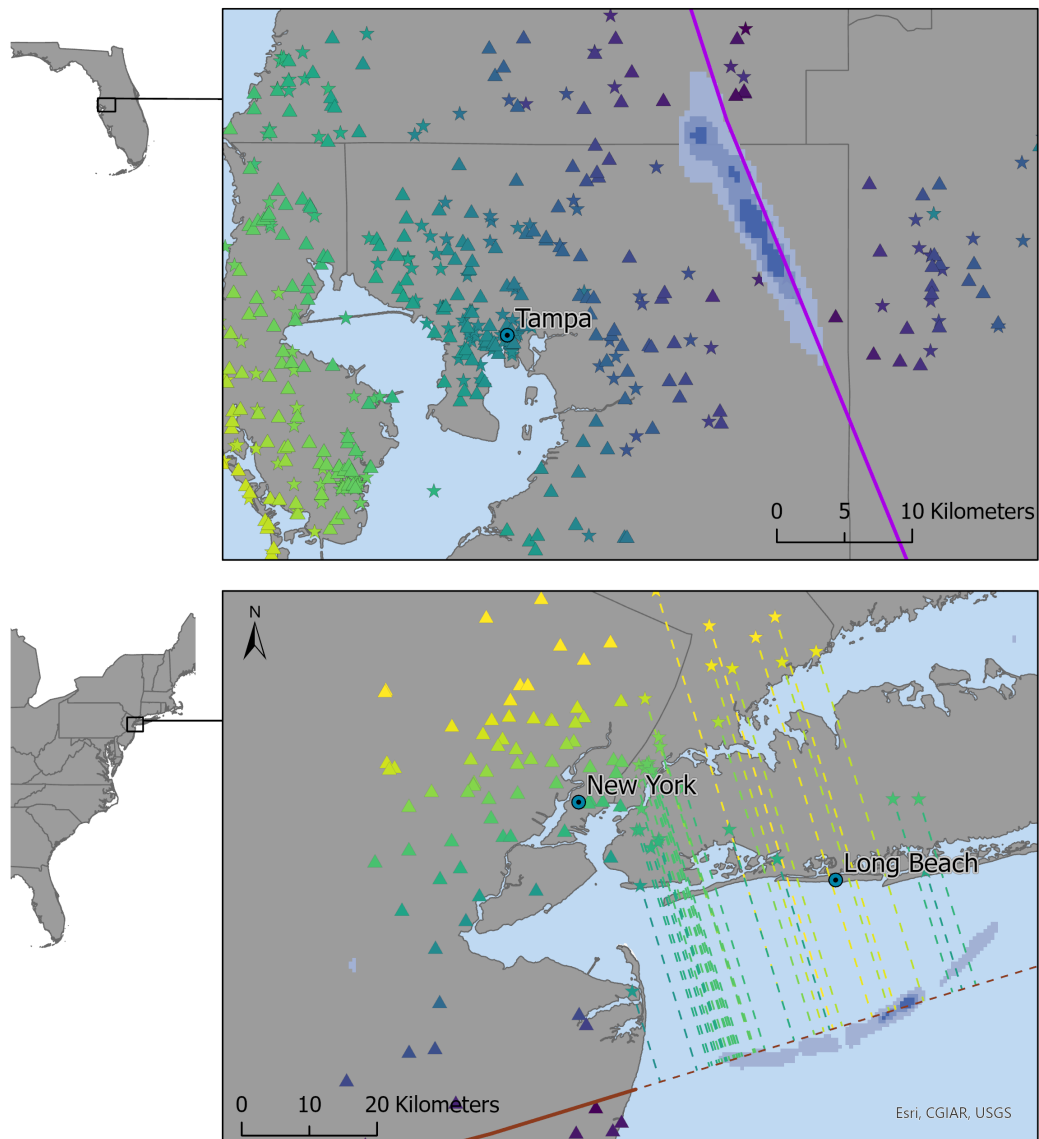
We visualize our approach’s geographical accuracy in Figure 3.16 (top) for the *BS split* with the GWR model. The displayed subset consists of a regional area in Florida, US. For the visualization of the respective results, we focus on the selected study area subsets to allow the recognition of details for better understanding. The total area of the hurricane passage could not be visualized due to its size. Very few estimated test datapoints show

deviations from their expected distance compared to their surrounding points of about 15 km. Most deviating test datapoints differ from their expected distance compared to their surrounding datapoints by only about 5 km. In the eastern part of the subset, a major part of the test datapoints is estimated to be of a distance of ≤ 30 km from the track, while they should be rather ≤ 50 km from the track according to the training datapoints. When postprocessing the estimated distance from the tweet point to track to derive the actual impact area, we obtain distinct areas characterized by varying degrees of likelihood for the impact area's presence. Overall, the estimated impact area corresponds very well with the hurricane track reference, especially for the central area of the subset. Towards the edges of the investigated subset, the impact area is not estimated with high likelihood.

Since the ET model achieved the higher scores for the regression task, this model is applied for the impact zone estimation considering the hazard's development. The selected model on the *TN split* trained considering the temporal aspect, using datapoints from both the TCs **Irma** and **Ida**, achieves medium scores (Table 3.8). ET model shows a medium score for R^2 results with a value of about 67%. When considering RSME, MAE, and ME, ET achieves still outstanding results considering the temporal distinct datapoints (RSME: 8.5 km, MAE: 6.4 km, and ME: 22.8 km). We apply the ET model exemplarily to visualize our model's geographical accuracy in Figure 3.16 (bottom). The displayed subset consists of a regional area in New York, US. Most of the estimated test datapoints' distances corresponds well with the closest actual train datapoint's distances. We see no major miscalculations of test points except for one test point closest to the TC track. It shows a deviation from the expected distance compared to its surrounding points of about 20 km. Additionally, in this visualization, we explicitly display the estimated distances from the test datapoints to the yet-to-be-estimated hurricane track. This presentation aims to enhance the comprehension of the factual meaning of the estimated values. When postprocessing the estimated distance from the tweet point to track to derive the actual impact area, we obtain distinct areas characterized by varying degrees of likelihood for the impact area's presence.

Table 3.8.: Regression metrics in of all TC approximation estimation models predicted on the test dataset and compared to the reference data. The following abbreviations are used: R^2 - Coefficient of Determination; RMSE - Root Mean Square Error; MAE - Mean Absolute Error; ME - Maximum Error; ET - Extremely Randomized Tree Regressor; GWR - Geographically Weighted Regression; TN - temporal-non-stationary. Adapted from [44].

Model	Split	R^2 in %	RMSE in km	MAE in km	ME in km
ET	Baseline	93.2	6.5	4.0	57.4
GWR	Baseline	82.4	10.5	5.9	130.5
ET	TN	66.8	8.5	6.4	22.8



Legend

- 0 km
- 75 km
- Cities
- ▲ Train Datapoints: Reference Distance [km]
- ★ Test Datapoints: Predicted Distance [km]
- Hurricane Irma Reference Track
- Hurricane Ida Reference Track
- - - Hurricane Ida Track to be Estimated
- - - Estimated Distance to Track [km]
- Likelihood of Impact Area Presence
 - Probable
 - Very Likely
 - Highly Likely

Figure 3.16.: Visualization of the estimated distances of test datapoints to the **Irma (VII)** track of the *baseline (BS) split* based on the Geographically Weighted Regression (GWR) (top) and the estimated distances of test datapoints to the **Ida (VIII)** track of the *temporal-non-stationary (TN) split* based on the Extremely Randomized Tree (ET) (bottom). Note that we do not display the reference distances nor the estimated distances for the **Irma** track results directly due to loss in visualization clarity. Instead, we display the distances only by color-coding of the respective tweet points. The estimated impact area obtained from the postprocessing of the estimated distances is displayed with its respective likelihood values. Data basis: © 2018 GADM. Projection: WGS84. Adapted from [44].

3.2.5 Discussion

The application scenarios' findings indicate that natural hazard impact zone estimations from VGI with methodologies for *stationary* and *moving* natural hazards showed satisfactory accuracies when compared with the respective (pseudo-) references. However, since perfectly fitting reference data (ground truth acquired during the hazard) are lacking, available reference data must be used. These are RS sensed images of the wildfires and NHC-provided TC tracks. These references, and the Twitter point locations' accuracy represent a limiting step in the workflow. The discussion of the applied models on stationary hazards like wildfires and moving hazards like TCs will be presented, respectively.

Stationary Hazards Discussion

For the wildfires, the findings indicate that tweets' weighted barycenter center calculation aligns well with the fire area pseudo-reference, as determined from RS imagery. The presented approaches also demonstrate that the estimated minimal and maximal affected area corresponds closely to the area detected from RS. Overall, no single one of the applied methods does achieve the best results for all investigated fires. The methodology performs satisfyingly on all investigated fire scenarios. While it does not work better or worse in any application scenario, the results are very different and influenced by various factors.

For the **Camp** fire, the barycenter also lies well within the pseudo-reference area, due to a distribution of VGI data mainly influenced by population density, whose effects we removed by weighting. Large areas of the extent overlap with the pseudo-reference. According to all approaches, fire areas of the highest likelihood are located near the most populated places, Chico and Oroville in the south and the devastated town of Paradise right in the center of the fire. Due to the location of the fire in the Sierra Nevada foothills, less information is available about the eastern area of the fire, which is located in the higher mountainous region with no significant settlements. However, the primary area of the fire corresponding with the pseudo-reference area was estimated using our approaches. Since the pseudo-reference represents the final extent of the fire at the end of the fire duration, it is spatially more extensive than our estimated extent three days after the start of the fire.

For the **Landiras** fire, the barycenter lies outside of the pseudo-reference area and is comparatively far from the areal estimation. This occurs due to the distribution of VGI datapoints that occur very far from the actual fire area, e.g., in the city of Bordeaux, which is located approximately 30 km from the fire location. Despite the weighting of datapoints the barycenter is shifted towards this high-density population and tweet occurrence hub. The estimated area from VGI corresponds to the northern area of the RS data area. The fire spread from the north to the south in this application scenario, which corresponds well with the findings. Despite a deficient amount of VGI data in this application scenario, the area estimation is good. This is attributed to a suitable estimation geometry, as this area

is generally flat, and the fire was seen from even distant places without obstruction. The estimated area is also closer to populated places where people might be more affected.

For the **Var** fire, the barycenter lies slightly shifted from the pseudo-reference area, which can be explained by the characteristic, very narrow shape of the fire area. The narrowness of the area makes it challenging to pinpoint the actual center accurately. The correspondence of the VGI extent with the RS extent is mostly limited to the middle of the RS area. Though the number of VGI datapoints is acceptable in this application scenario (compare Table 3.5), several factors contribute to the quality of VGI data for estimating the fire area. Firstly, the rapid spread of this fire covered the entire area in just one and a half days. Observations were hindered as it ignited in the late afternoon and continued to propagate through the night. Additionally, the fire area was relatively small (compare Table 3.4), and citizens in more distant areas showed little interest, contributing to suboptimal estimation geometries. Due to the fire's location traversing the hilly region of the Massif des Maures, visibility towards the fire was constrained to specific places, leading to a non-ideal distribution of VGI points. Additionally, for the **Var** and **Landiras**, the fire and road agencies responsible do not use Twitter as an information distribution tool. Consequently, the estimation of road closure areas, as outlined in the developed methodology, is unavailable in these cases.

In conclusion, the most impactful error source for estimating wildfire extents from VGI is, of course, the distribution of VGI. Even with low data (e.g., **Landiras** fire), the fire area can be well estimated if the viewing geometry is suitable. Factors that influence the distribution of VGI are mostly related to the visibility towards the fire (e.g., mountain obstruction, night, places very distant to fire, small fires). These are the main limiting factors to obtaining suitable information from VGI data. Moreover, utilizing distinct methodologies, specifically the barycenter and area estimation approaches, prove highly valuable. The influence of various factors affecting these analyses results in independent outcomes that mutually complementing each other. For instance, in the case of the **Landiras** fire, the barycenter is less precise due to VGI data characteristics distant from the fire location, which is attributable to good visibility. Conversely, these characteristics contribute to highly accurate results in estimating the fire area.

In contrast to the studies focusing on information retrieval from VGI data during wildfires (e.g., [167, 168]) and the few existing studies for spatial analysis of wildfire hazards using VGI data [158, 177, 178], the developed methodology can be easily transferred to other wildfire scenarios. The use of a variety of freely available information from VGI data and the use of supplementary data to account for demographic biases has not been employed frequently [22]. Due to the use of these in this study, the transfer to other wildfire studies is possible, as demonstrated. Additionally, accuracies range within several kilometers compared to temporally close hazard extents derived from other data sources. These accuracies indicate that wildfire extent estimations are achieved at significantly higher accuracy levels compared to estimations using, for instance, only kernel density [22].

Moving Hazards Discussion

For the TC, the findings indicate that the underlying regression task for impact zone estimation is feasible, based on the provided input features extracted from the tweet locations and the supplementary data. All model and split combinations achieve comparatively high R^2 -values. With RMSE and MAE of 4 km to 10 km, all models and splits (*BS split vs TN split*) estimate the points at a reasonable distance from the actual reference distance to the TN track. However, the ME should be considered when evaluating the results, and outliers might be removed to achieve a corresponding overall result. Evaluating the overall performance, the results of the ET model are most beneficial for the regression task to estimate the distance to the natural hazard.

The visual results (see Figure 3.16 in Section 3.2.4) reveal that our model can accurately regress the distance from tweet points to the natural hazard. Most of the test points' predicted distance correspond well with the train point's reference distance of datapoints in a near area. Compared to the reference track, the estimated distances for the datapoints clearly show the regression approach's applicability for natural hazard extent estimation. However, the model miscalculates a few test points. With a few points of 15 km and some points of 5 km deviation, these misclassifications can be neglected. Our employed postprocessing of the estimated distance from tweet points to the hurricane track is suitable for the delineation of the impact area's presence. For the Florida subset region, comparing the estimated impact areas with the hurricane track confirms the high accuracy of the estimation approach, particularly in the central region of the subset. However, as moving towards the periphery of the investigated subset, the likelihood of accurately estimating the impact area decreases due to lower test point density distributions in this area. Combining such partially estimated impact areas from various high tweet density hubs could be used subsequently to interpolate from the total hurricane track length impact area. In the investigated New York subset region, the circular shape of the estimated area can be explained by the distribution of the test datapoints to the track. These are all located on the track's northern side, leading to a less suitable trilateration arrangement. In general, the estimation of the impact zone including the temporal component of moving hazards, is much more difficult than the estimation of stationary hazards.

Overall, this approach demonstrates high accuracy compared to traditional weather data forecasts (e.g., [245, 246]), which are mostly based on weather models, e.g., European Centre For Medium-Range Weather Forecasts [247]. Numerical models relying on such data are the primary prediction method [248] for TC track estimation. Precise actual hurricane tracks with traditional methods are only provided after a TC event, sometimes not until one year after the event [249]. In contrary, this approach is able to estimate the hazard impact zone in near-real time using the temporal-non-stationary split method. Furthermore, this approach provides a first approach towards a TC impact area estimation using VGI. In

contrary, studies using VGI data for TC analysis so far only focus on information retrieval for the event [164, 165] and very coarse spatial analysis [131, 176].

General Discussion

It is essential to note that the employed methodologies are not meant to display the exact hazard area per se. Instead they should give a quick, first approximation of where the hazard might be positioned and might have an impact on human life. Therefore, the developed methodologies are an excellent first measure to localize the approximate hazard position, especially when lacking other data. Especially when introducing a further challenge with high degrees of temporal development of the hazard estimation, accuracies drop. Nevertheless, these estimation results remain valuable, especially in the absence of other data for the approximate hazard extent estimation.

The developed approaches are applicable for a generic natural hazard estimation from VGI data. They offer high accuracies compared to existing approaches for natural hazard impact zone modeling (e.g., TC track modeling [250, 251, 252], and *stationary* hazard extent estimation [22, 21]). Furthermore, near-real-time availability is given compared to remote sensing data, normally used for natural hazard estimation and mapping [14, 253]. Finally, we can adequately estimate a near-real-time scenario for a hazard with high degrees of temporal development. We extracted information from the tweet locations, texts and dates.

Limitations of VGI VGI data provides approximate indicators of hazard locations with limitations. It lacks data in uninhabited areas, introducing biases towards populated regions. Data accuracy varies, with human estimations being less precise. Viewing angle calculations and corrections are used to account for inaccuracies. Additionally, VGI is influenced by regional factors and randomness, making it less accurate than technical sensors.

Advantages of VGI VGI, like Twitter data, offers a real-time alternative to RS data for hazard identification. VGI's immediate availability is a critical advantage, enabling rapid response during natural disasters. It provides richer information, including text details about hazards, sentiments, and areas where humans are impacted. This complements RS data, making VGI valuable for rescue services. Estimations using VGI data are particularly useful when other data sources are lacking for initial hazard assessments.

3.2.6 Conclusion and Integration in Framework

Overall Conclusion Overall, the results for the approximate area estimation for *stationary* and *moving* natural hazards from VGI data are very promising. The investigated hazards, chosen to represent a diversity of natural hazards, come with varying available reference data for the hazard scenarios. Furthermore, different characteristics of the hazards and the tweeting behaviour, in these cases, require various supplementary data that help to describe tweet occurrence. Due to these varieties in hazard scenarios, divergent methodologies need to be developed for *stationary* and *moving* natural hazards, separately. One significant contribution of VGI and an advantage compared to, e.g., remote sensing data, is the availability of text messages. While these methodologies may not provide the highest accuracy, they serve as first tools for rapidly identifying and assessing potential hazard areas, particularly in scenarios where alternative data sources are limited or unavailable.

Limitations and Outlook The challenge of diverse hazard characteristics has been addressed by developing methods for *stationary* and *moving* hazards. However, varying availability of reference data is another challenge for the estimation of hazard impact zones using VGI. The reference data used for the evaluation of the *moving* hazards methodology have been accurate. In contrary, actual reference data for the investigated time of the wildfire using VGI data was not available. Instead, pseudo-reference data from later time steps have been used. The evaluation of the developed methodology would benefit from incorporating accurate and temporally aligned reference data. E.g., MODIS data could be employed. These are available day-wise but with a much lower spatial resolution. Furthermore, the developed methodologies could profit from the pre-processing of tweet text, including reliability analysis, to enhance their accuracy. More specific information about the hazard event could be extracted via NLP from the texts to improve the hazard impact zone estimation methodology.

Framework Integration These methodologies can be adapted to a range of hazards based on the hazard's respective characteristics. For instance, the methodology developed for wildfires can be adapted for other stationary hazards like floods. While this section primarily focuses on estimating the impact zones of fires and TCs, it contributes to a broader framework for assessing the effects of various natural hazards on road networks. The presented approach demonstrates the possibility of integrating VGI data into the broader context of natural hazard management. By evaluating the spatial alignment of the estimated hazard zones from VGI with the road network, it becomes possible to estimate their impacts on roads, as discussed in more detail in Section 4.3.2.

3.3 Road Impact Extraction from Volunteered Geographic Information Data

Besides spatial analysis (compare Section 3.2), information extraction (e.g., [24, 157, 163]) is a valuable task using VGI data. In the context of road network analysis, one significant application of VGI is the extraction of road impact information and its geolocalisation. A methodology is developed to extract road-related data, such as road intersections and segments, obtained from tweets texts that contain information regarding damage or blockages of the roads using NLP techniques. Subsequently, the extracted road locations are geocoded.

3.3.1 Introduction

VGI has been used in various studies for extracting location information from text. Extracting place names from text, in general, is conducted using geoparsing. Geoparsing is converting text descriptions of places into geographic identifiers, like coordinates. It consists of two steps:

1. extracting place names from text and
2. geocoding the extracted place texts into geographic identifiers.

The first step (1) is mainly conducted mostly with NER or RegEx (e.g., [240, 241, 242]). New studies focus on improving general place extraction from texts by using various techniques like convolutional neural networks for text analysis [254] and transformer models [255]. Some studies also focus specifically on improving road names' extractions [25]. Secondly (2), only a few studies focus on the improvement of the place names' geocoding. However, it is equally important, as a better place name extraction is only valuable for geographic applications if all the newly extracted place names can also be allocated to a geographic location. Currently, the main geocoding methods employed are Google Place API [240, 256, 241], Yahoo Placemaker [257] and ArcGIS geocoding [258], which are not freely available. Recently, more studies have also used open-source geodatabases (e.g., [259, 260]). However, not all APIs and databases offer precise geoparsing at road level.

VGI has been used in a few studies in road analysis contexts. It has generally been applied mainly for road location approximation from Twitter posting location [261] or text indicators [262]. Furthermore, VGI has been used for event detection near roads (e.g., traffic event detection) [263, 258, 262]. These studies, however, do not focus on detailed road intersections or road segment locations. Using VGI text for specific road place extraction, among other traffic event-related named entities, has been described

in Ünsal [264]. Vallejos et al. [265] geocode traffic incident locations recognized from NER precisely. Yu et al. [25] and Gelernter et al. [138] focus on road extraction, which extracts place names from text data but do not conduct the geoparsing step. In summary, geoparsing has improved in the past years when focusing on road name extraction, but gaps exist in specific geographical road location extraction. VGI data has yet to be studied for intersection or road segment information extraction for geographical applications. As a result, the accuracy requirements for such applications have yet to be adequately addressed.

3.3.2 Data

Selected Application Scenario The application scenario used for this investigation is a flooding that occurred in 2022/23 in the **San Francisco Bay Area**, CA, US (IX). This application scenario was selected as the hazard occurred in an urban area with high numbers of VGI data and with a dense road network. Starting on 31/12/2022 heavy precipitation led to widespread flooding in large parts of California, persisting until 25/03/2023. The flooding resulted in evacuation orders for 6,000 people in total, 200,000 homes without electricity and 22 fatalities. The analysis of VGI data for flood hazard impact determination includes data obtained within the entire San Francisco Bay Area. Figure 3.17 visualizes the location of the flood.

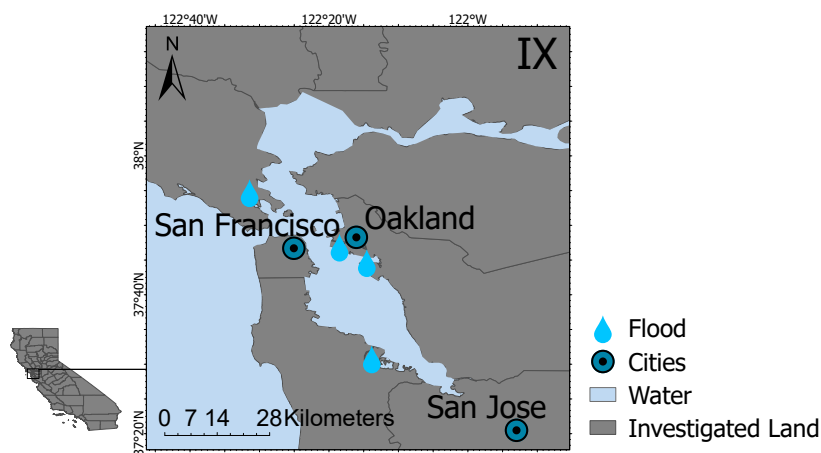


Figure 3.17.: Overview of the cases study hazard location for the **San Francisco Bay Area (IX)** flood. Data basis: © 2018 GADM. Projection: WGS84.

Datasets Information about closed roads or deteriorated road conditions during a natural hazard is usually available from responsible agencies like firefighters or police. Still, recently more studies have focused on including citizen science [266] in the form of VGI data. This section employs Twitter data as VGI data for impacted road extraction. Twitter is used in recent studies due to its widespread usage and easy accessibility [20, 267, 268]. The specific Twitter data are acquired from Twitter’s download API using Python

programming. The tweet data containing relevant keywords about the hazard, for the time when the natural hazard takes place, are extracted for the application scenario. Next, only tweets containing relevant keywords about infrastructure are selected. We extract the tweet location, date and text.

In total, we collected 32 non-identical road-related and hazard-related tweets. The low number is due to the exclusion of:

- Messages of identical content if a specific road segment is closed for a longer time and the identical message is repeated for update purposes.
- Messages that are road-related but related to another hazard than the investigated one (e.g., car fires in the investigation region).

3.3.3 Methodology

We consider blocked road information. Road authorities often post this information in emergency or hazard cases. We search tweets with mentioning such information or tweets posted by the responsible agencies. Tweets by road agencies or other agencies posting about road conditions have mostly a similar structure, mentioning a major road affected between certain intersections with that road. Considering this structure, we conduct our methodology. The road extraction can be divided into three tasks:

- Text processing
- Geoparsing
- Geographic Information System (GIS) processing.

Figure 3.18 displays the process. The tasks are conducted as follows for each tweet text:

1. From the tweets' texts, we first extract place locations via NER (e.g., *Oakland, CA*). Furthermore, we extract road locations via RegEx implemented for roads (e.g., *Angeles Crest Hwy*).
2. We save the extracted locations of one tweet text in a merged format, saving (1) the general location and (2) all extracted road names separately.
3. We geoparse the general location by searching the location name in the geodatabase and extracting the associated place polygon. This general area is used to search for the road names only in a specific area in the following steps, which is vital as specific road names appear in different neighborhoods or even different cities.
4. We geoparse the road names by post-processing the road names and searching for their names in the road database. Thus, we extract road lines in a GIS.

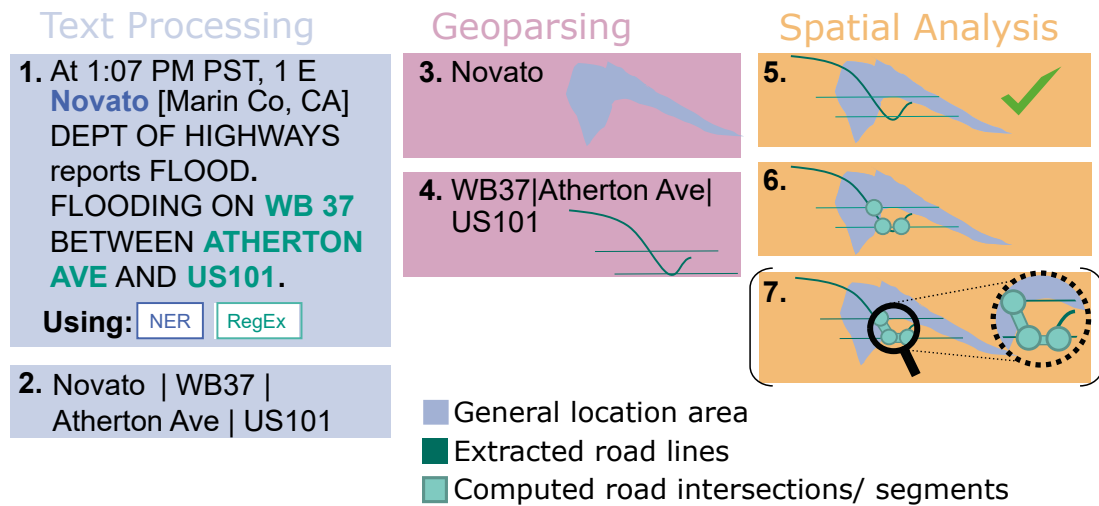


Figure 3.18.: Visualization of the impacted road extraction framework during natural hazards from Twitter data. The following abbreviations are used: NER - Named Entity Recognition; RegEx - Regular Expression. Reprinted from [1].

5. We overlap the extracted road lines with a general location polygon to ensure we extract the correct road of the specified neighborhood.
6. We then compute the intersections of the extracted road lines if several road names have been mentioned in the text (e.g., *Atherton Ave & US101*) and obtain intersection points.
7. Finally, to find affected road segments as mentioned in the tweets' texts (if several road names have been mentioned), we extract the road segments located between the extracted intersection points.

3.3.4 Results

For the **San Francisco Bay Area** floods, from a total of 32 messages that contain road location information, four messages have data that are not accurate enough for road information extraction (e.g., *Flooding in all lanes on Interstate 580 EB.*) . This kind of message would allow us to extract the road name Interstate 580. But since the highway passes through the total region of the San Francisco Bay Area and from the text, we do not know which segment(s) of the road are meant. Therefore, these messages are considered too unspecific. Furthermore, the methodology fails on another four messages either in the text processing step or in the geoparsing step. The name extraction fails due to different naming conventions, e.g., *Camino Pablo*. In this example the English RegEx and NER do not consider Camino (Spanish) as a road name. The geoparsing fails because the extracted road location names can not be linked with a geographical location (e.g., *Bryant onramp*)

as they are not named in our database. In total, we obtain 24 messages from which road extraction is possible.

With our road extraction method, we obtain three types of information about roads, depending on the information available in the text:

1. Only a single road name is mentioned, which means we can extract the total road segment as a line feature.
2. Only an intersection of two roads is mentioned, so we can extract this intersection as a point feature.
3. Several roads and/or specific intersections of several roads are mentioned, which means we can extract the road segments between the said intersections as a line feature. Therefore, this type of information offers the most precise impacted road segment extraction.

Figure 3.19 displays the different extracted roads for the application scenario of the Oakland flood. We observe that from most text information data we obtained road segments and corresponding intersection locations. Only for one example, we only extract a single intersection information, which doesn't allow us to extract a corresponding affected road segment. The extracted roads are distributed all over the investigated areas. Furthermore, we observe that major roads are mostly being extracted, as these are talked about in tweets from road agencies.

3.3.5 Discussion

For the **San Francisco Bay Area (IX)** flood scenario, we have a low number of non-repeating texts about the road conditions during the hazards. However, these few texts allow the extraction of relevant impacted road segments for this hazard. We encountered few challenges in accurately extracting road information from the messages. We encountered a few challenges in accurately extracting road information from the messages. We found that a few messages needed to be more accurate for road information extraction, containing only general road names without intersection locations. These messages are not suitable for our analysis. Additionally, we encountered issues with the name extraction step that failed due to different naming conventions and the geoparsing step that failed due to location names needing to be linkable to geographical locations. Furthermore, when only a single intersection location is extractable, determining the corresponding affected road segment is impossible. However, a substantial number of roads that are impacted by the hazard can be extracted with a high level of detail (intersection-wise). Due to the extraction from authority data which verify and often update the data compared to other tweet data, these roads can be extracted with a high level of certainty. Our presented

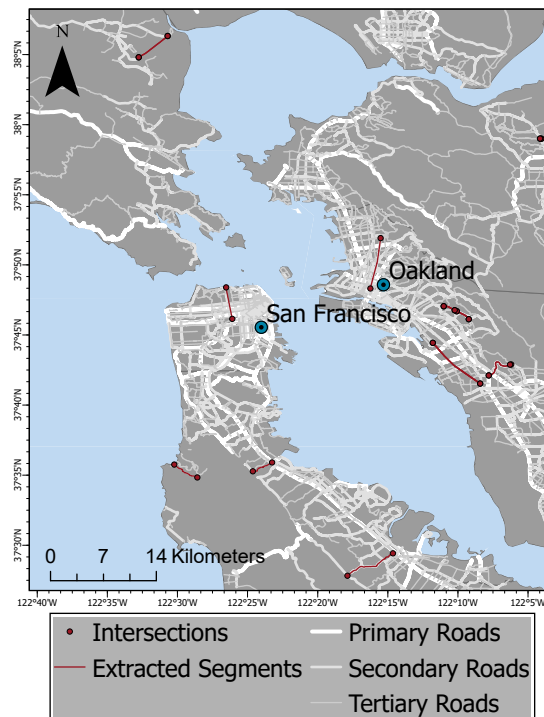


Figure 3.19.: Visualization of extracted impacted roads from Volunteered Geographic Information (VGI) text information data for the flood in the **San Francisco Bay Area (IX)**. Data basis: © 2018 GADM. Projection: WGS84. Reprinted from [1].

methodological approach is a first approach towards precise road place extraction, including name extraction and geocoding, which has not been conducted before. Though Yu et al. [269] focused on precise road name extraction, they focus on something other than geocoding. Other studies do not focus on road extraction specifically and often use geocoding with nonspecific place names, e.g., [255, 240]. A drawback of the developed methodology is that extracted roads primarily consisted of major roads, as they were the ones prominently discussed in general tweets and from road agencies. Information about smaller impacted roads can not be gained from these data sources.

3.3.6 Conclusion and Integration in Framework

Overall Conclusion The road extraction methodology allows the extraction of impacted roads from text messages of VGI data. Overall, our road information extraction methodology provided valuable insights into the impact of hazards on road networks. While facing particular challenges, it still demonstrated its potential in capturing relevant road information from social media messages during hazard events.

Limitations and Outlook However, future improvements could be made to address the limitations encountered during name extraction and geoparsing. Improvements could include, e.g., RegEx patterns for other languages that could extract Spanish road naming

conventions or the integration of other databases including highway ramp names for geoparsing. Additionally, as the developed methodology is based on general text assessment, it could be transferred to other textual information sources, such as police reports documenting road issues. This expansion could improve the accuracy and increase the amount of extracted information regarding impacted roads.

Framework Integration The road extraction from VGI methodology contributes to the framework by providing valuable insights into the direct impact of hazards on road networks. Traditional hazard impact assessment approaches often rely on official reports of responsible agencies. By extracting road-related information directly from VGI text messages, the framework gains a more immediate view of road conditions during hazard events from freely and openly available data sources. However, the impacted road location extraction methodology could be applied to various text information data. Furthermore, the approach can be easily transferred for any hazard scenario and type where tweet or general text data are generated. Integrating road information extracted from VGI sources complements the multi-source geoinformation approach of the broader framework of natural hazard impact determination from geoinformation data. Extracting directly impacted roads from VGI provides a more precise evaluation of the extent and severity of damage on the specified object of the road infrastructure, compared to impact zone extraction. Assessing the spatial alignment of the extracted impacted roads with the road network enables the analysis of the impacts on roads described in Section 4.3.2.

3.4 Synthesis on the First Module

In conclusion, **Module I** forms the basis of the framework designed to assess the possible impacts of natural hazards on road network accessibility. The module thereby relies on various geoinformation data: RS and VGI. These data provide an appropriate basis for the determination of hazard impacts. The assessment of the hazard impacts on road networks requires a nuanced approach that distinguishes between two fundamental types of impact: hazard-affected areas and direct impacts of the hazard on road infrastructure. Affected areas involve estimating hazard impact zones first. Figure 3.20 displays the components developed in **Module I** to determine the natural hazard's influence using various geoinformation data, subdivided into hazard impact zones estimation and direct road impact extraction.

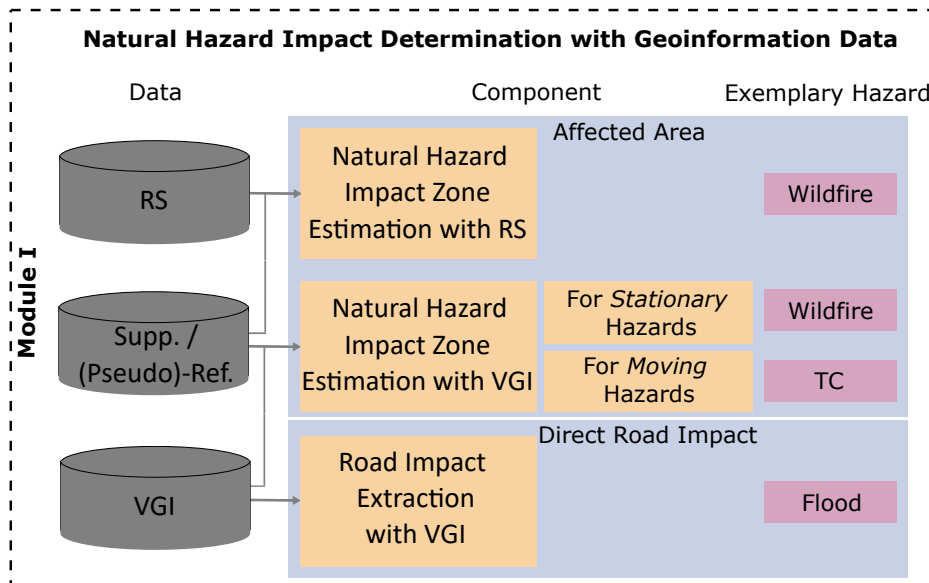


Figure 3.20.: Visualization of Module I, the natural hazard impact determination with geoinformation data, subdivided into natural hazard impact zone estimation with remote sensing (RS) data (Section 3.1) and Volunteered Geographic Information (VGI) data (Section 3.2) for *stationary* and *moving* hazards, and direct road impact extraction with VGI (Section 3.3). The following abbreviations are used: Supp. - Supplementary Data; Ref. - Reference Data; TC - Tropical Cyclone.

Hazard impact zones can be accurately estimated using high-resolution remote sensing, which is demonstrated for the mapping of wildfires (Section 3.1). For other hazards, the methodology can be adapted using similar machine learning models and similar data sources (compare also Section 2.1.1). However, when high-resolution RS data are not available due to the non-commercial satellites' overpass time of a few days, VGI data can be used to map hazard impact zones in near-real-time. With two different methodologies for two hazard types (*stationary* and *moving*), it is demonstrated that the use of VGI data for hazard impact zone estimation is possible. Other hazards that show similar characteristics to wildfires (e.g., floods) in terms of their rather stationary extent, can be estimated with the adaption of these methodologies using similar models and the same data sources (Section 2.1.1). In this thesis, it is demonstrated that wildfire hazards can be approximately estimated and areas where people are majorly affected by the hazard can be identified. TC hazards are characterized by high degrees of temporal development- Their impacts zones can not be properly mapped using RS data. It is shown, that for TC hazards, VGI data offer the opportunity to map hazard impact zones in near-real-time. Furthermore, direct impact analyses focus on the immediate consequences of a hazard's direct influence on road segments. Direct hazard impacts on roads for a flood hazard can be determined accurately by extracting road information from VGI (Section 3.3). By relying on text data, this approach offers a substantial advantage over RS techniques because text data yield additional information about roads impacted by hazards.

Extracting direct impacts in the form of impacted roads offers a more certain assessment of immediate consequences on, e.g., road infrastructure. Affected area estimation provides a broader understanding of potential disruptions. Both are essential for effective hazard management. In scenarios where complete data on direct road impacts might not be immediately available, the significance of estimated impact zones becomes evident.

All components (Section 3.1, Section 3.2, Section 3.3) are designed to be applied independently on hazards in different geographical locations and environments. Additionally, the components are designed to be easily transferable to other hazard types (see Chapter 5, Section 5.4.2). Furthermore, the determined hazard impacts serve as the basis for the assessment of the accessibility of road networks (Module II, Chapter 4) under the influence of hazard impacts in this thesis. By analyzing the spatial relationship between hazard impact zones and roads, planners and emergency responders can evaluate which segments of the road network may be affected (compare Module II, Chapter 4). Subsequently, they could conduct accessibility analyses based on the determined hazard impacts.

Road Network Accessibility Assessment during Natural Hazards

This chapter includes elements from

[1] J. Florath, J. Chanussot, and S. Keller. “Road Accessibility during Natural Hazards Based on Volunteered Geographic Information Data and Network Analysis”. In: *ISPRS International Journal of Geo-Information* 13.4 (2024), p. 107

marked with a [green line](#).

[Module II - Road Network Accessibility Assessment during Natural Hazards](#) is the second part of the framework for the assessment of natural hazards’ impact on road infrastructure. [Figure 4.1](#) displays the steps developed in [Module II](#) for the road network accessibility assessment during natural hazards. First, the degraded network which experiences hazard impacts is constructed. Secondly, the network accessibility under hazard impacts is analyzed. Like the first module, the network analysis relies only on freely and openly available road data in the form of OSM data. To estimate the hazards’ impact on road networks an overlay operation that superimposes the hazard impacts on the road network datasets is performed in [Section 4.3.2](#). This overlay operation provides valuable insight into the spatial intersection of hazards and roads, highlighting the precise locations where road functionality may be compromised. The resulting *degraded road network* then becomes the basis for conducting in-depth accessibility analyses. Degraded road conditions are investigated to evaluate the overall accessibility within the network before and during/shortly after the hazard as well as the change in accessibility ([Section 4.3.3](#)).

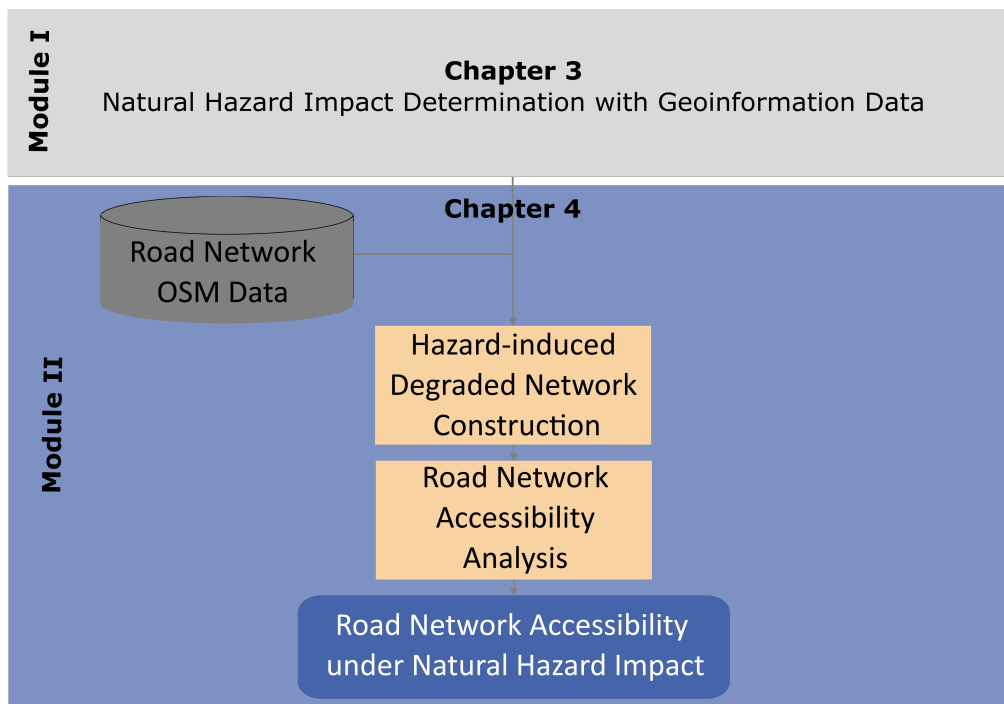


Figure 4.1.: Visualization of Module II, the road network accessibility assessment during natural hazards using input from Module I, subdivided into the introduction of the Open Street Map (OSM) road network data (Section 4.3.1), the hazard-induced degraded network construction (Section 4.3.2) and the network accessibility analysis (Section 4.3.3). The final result of this module and the infrastructure assessment during natural hazards framework in total is the road network accessibility under natural hazards' impacts.

4.1 Introduction

Road network analysis studies relationships and interactions between entities (nodes and edges) in a road network, utilizing tools to calculate paths within the network. A path refers to the route between nodes in a network. It is a series of interconnected edges that connect one node to another. The paths within a network can be computed using various performance measures as basis. E.g., the distance corresponds to the calculation of the shortest paths, or the travel time corresponds to the computation of the fastest paths [35, 12].

Further performance measures are throughput and capacity [270, 271], topological measures [272, 273], economic measures [274], and accessibility [275]. One important measure defining the road network performance is accessibility [275]. Accessibility is defined as the ease with which a location can be reached. However, there are various measures of how accessibility can be determined. Accessibility indices [12, 276] have been applied in a few studies. These metrics mostly rely on connectivity information but require more detailed traffic and travel demand data for more complex network analysis (e.g., [270, 277]). Obtaining daily or average travel demand data is often already diffi-

cult [278, 279]. This difficulty is intensified in hazard situations that deviate from average daily traffic scenarios. Even when average travel demand data are available, they may not accurately reflect travel patterns in hazardous situations. As a result, metrics that do not rely on other traffic data are more useful in such cases.

Utilizing accessibility-based metrics enables a fast and generic analysis of the hazard-impacted road network. Such metrics measure the connectivity between locations, which is a direct road network performance measure. Many methods rely on graph theory (e.g., [31, 32]). Common accessibility methods include the use of various measures of connectivity (e.g., beta index, association number, alpha index, gamma index) and accessibility indices (Shimbel index and nodal degree) [33, 280, 281]. For network analysis, the graph theoretical measures betweenness and closeness centrality are often used [282, 283, 284]. They provide a fast and overall picture of accessibility in a road network but do not include specific scenarios that could be important to natural hazard planning and emergency response. Antunes et al. [285] and Santos et al. [286] present accessibility-maximization approaches in a critical road infrastructure context. Accessibility-based performance measures are also proposed by Chen et al. [287].

Otherwise, accessibility indices can be adapted to situational requirements, like an immediate emergency response (evacuations or emergency facility access [12]) or general connectivity investigations (remoteness of places [276]). As a basis serves the calculation of shortest paths according to Dijkstra [288]. However, here, different metrics can be used again, like the distance along graph edges or the travel time along graph edges [289, 12], for calculating the shortest or fastest path, respectively. Applying graph theory for road network analysis, different criteria apart from the simple shortest paths can be valuable in general [290, 291] and for accessibility measures [280]. The use of k-shortest paths has been investigated, e.g., in Chondrogiannis et al. [292] and [290]. However, these criteria have not been considered for alternative road network accessibility analysis measures in a hazard context. In total, we rely on four different methods to analyze the accessibility change due to the hazards' impacts. These are the theoretical accessibility measures betweenness centrality (BN, 1) and closeness centrality (CN, 2) based on graph theory (e.g., [293, 283]) that are employed for the first time in an accessibility change estimation using a degraded road network. Furthermore, we use a free-flow assumption accessibility index adapted from Guth [12] for shelter accessibility analysis (SAI, 3). Besides, an alternative routing assumption accessibility measure (ARAA, 4) will be newly developed. This measure is the first of its kind to consider anticipated congestion scenarios. Each method is applied to the data of the intact and degraded road network and the differences in accessibility are computed.

4.2 Data

Selected Application Scenario For the road network accessibility analysis, the flood data from the **San Francisco Bay Area** (see Figure 3.17 in Section 3.3.2) are employed once more as an exemplary hazard. This hazard is suitable, as it occurred in an urban area with a dense road network and a high number of impacts on the road conditions. However, due to the large size of this region, the application of the network analysis is restricted exclusively to a subset within this area, specifically the city of **Oakland (X)**. The city of Oakland, located within the San Francisco Bay Area, documented unprecedented 24-hour rainfall records during the course of this event. Figure 4.2 visualizes the location of the flood.

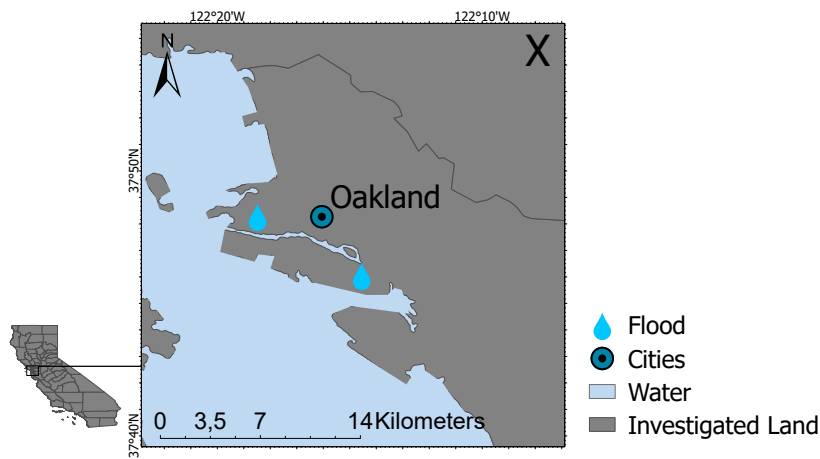


Figure 4.2.: Overview of the cases study hazard location for the **Oakland (X)** flood, a subset of the **San Francisco Bay Area (IX)** flood (Figure 3.17 in Section 3.3.2). Data basis: © 2018 GADM. Projection: WGS84.

Road Network Related Data To carry out the accessibility analysis, we use a road graph network (compare Section 2.1.2) retrieved from the OSMnx [184] python package. For the selected **Oakland (X)** application scenario, we selected a reasonable region of interest and extracted the graph's nodes and edges within this region. It is essential to use cleaned graphs that only contain relevant nodes that represent road intersections. This is assured by the preprocessed OSM road data obtained from OSMnx (compare Section 2.1.2).

The OSM data need to be evaluated to address the concerns about the reliability of VGI data, which can be subject to various biases and limitations. We use authoritative road data from government sources of the respective application scenario region. These are the San Francisco Bay Region Roadways by the Metropolitan Transportation Commission, which is the transportation planning, financing, and coordinating agency for the nine San Francisco Bay Area counties. Additionally, we use Maxar World Imagery, a high-resolution satellite imagery prepared by a free provider.

Table 4.1.: Overview of network analysis data for the **Oakland (X)** flood. Adapted from [1].

Shelter locations	N° Edges	N° Nodes
St. Vincent de Paul, Ira Jinkins Community Center	22,289	8,472

Additionally, some of our network analysis approaches need specified destination points within the network (compare Section 4.3.3). In our study case, the destination points are emergency shelters. Data about the location of emergency shelters are obtained from the respective responsible agency, the city of Oakland administration (oaklandca.gov), for the flood hazard. The reason for the selection of the subset of the city of **Oakland (X)** is the availability of a reasonable number of emergency shelters (two) that can be reached within this region. Table 4.1 displays the selected shelters' information and the number of edges and nodes that were selected for the application scenario.

Hazard Impact-Related Data For the construction of the degraded network after the hazard started, we use the impacted roads extracted from VGI (Section 3.3) for the selected scenario region of **Oakland (X)**. Additionally, impact zones for the **Oakland** floods are used. This is a 100/500-year flood hazard map provided by the Association of Bay Area Governments for the San Francisco Bay Area. These Federal Emergency Management Agency's flood hazard zones are based on historical data about regional flooding. 100-year floodplains are areas with a 1% (1 in 100) annual chance of flooding that are likely to be flooded at least 0.15 m. 500-year floodplains are areas with a 0.2% (1 in 500) annual chance of flooding. The map includes the 100 and 500-year floodplains designated by the agency and potential floodplains currently protected by levees. The used map was updated on July 1, 2022.

4.3 Methodology

In the following, the network basics (Section 4.3.1), the methodology to construct the degraded network (Section 4.3.2), and the network accessibility analysis (Section 4.3.3) are described.

4.3.1 Road Network Basics

The OSM data are evaluated to address the concerns about the reliability of VGI data, which can be subject to various biases and limitations. We compare the edges of the OSM network data to the authoritative road data to evaluate the OSM data's accuracy. Between the OSM and the administrative data source, 6% of the road data are different. When visually comparing OSM road data and Maxar World Imagery, OSM data mostly deviate on

private property grounds, e.g., harbor area and open cast mine land. The reason being private roads not mapped in OSM data.

The network analysis focuses on the accessibility of the road network and therefore on the accessibility of points within the road network only. Origin and destination points for path calculations in the network are graph nodes, in the following referred to as starting and endpoints. The starting and endpoints for the calculation of our accessibility measures (Section 4.3.3) depend on the specific region of the network being analyzed and the selected measure. In general, the starting and end points for the investigated pathways are all nodes within the network. The starting point is any node within the network, and the endpoint is each of the other nodes in the network. However, few accessibility measures do not calculate the accessibility to each node but only to few specified destination (end) points. A use-case scenario focusing on the accessibility analysis of evacuation shelters is investigated. These shelters are crucial during natural hazard events. In contrast to e.g. emergency facilities, which are also crucial during hazard events, non-emergency-vehicles trying to reach shelters are more likely to be stuck in congestions. Evacuation shelters (see Section 4.2) are therefore predisposed to scenarios of expected congestion. Therefore, their use as destination points allows the evaluation of accessibility under anticipated congestion scenarios.

As the nodes of the road network are the starting points for the network accessibility analysis, the accessibility measures are calculated and stored for each network node. The edges' accessibility is calculated as the minimum accessibility of its two connecting nodes, as an edge can be only as accessible as the node with the lowest accessibility among the nodes it is connected to.

4.3.2 Degraded Road Network Construction based on Hazard-Induced Impact

In this section, the focus lies on identifying the network edges that have been degraded by the hazard. Therefore, the determined hazard impacts are overlapped with the road network data. These are the impacted roads, as extracted using VGI data (e.g., Section 3.3) for this application scenario, and the hazard impact zone. The hazard impact zone for this application scenario is a 100/500-year flood hazard map (see Section 4.2). During the overlapping process, roads in the network that experience direct impacts during the hazard (as extracted in Section 3.3) are categorized as *degraded*. Furthermore, roads in the network that overlap with the hazard impact zone are categorized as *degraded* as these roads are at risk of being degraded, too. This categorization also applies to situations where only a part of the road edge or a road segment end node is affected. When one node is degraded, the entire segment is affected because the degradation of a critical point disrupts the continuity and functionality of the entire network segment.

The degraded network is constructed from the uncorrupted network by eliminating the degraded segments (edges) and degraded intersections (nodes). When degraded nodes and edges are removed, parts of the network might become *disconnected* when they do not have any connection to the rest of the network anymore. In this case, we keep the main network with the largest number of connected components for the subsequent analysis. Degraded and disconnected nodes are considered non-accessible, and therefore an accessibility measure is not calculated for them.

4.3.3 Road Network Accessibility

To evaluate the impact of natural hazards on road network accessibility, all accessibility measures for the uncorrupted and the degraded network are calculated. Finally, to assess the network accessibility change, the difference in network accessibility before (uncorrupted network) and during (degraded network) the hazard is calculated. For each measure M for each node v , the impact is calculated as:

$$M_{Impact,v} = M_{before,v} - M_{after,v} = M_{intact,v} - M_{degraded,v} \quad (4.1)$$

Accessibility Measure Definition Betweenness and closeness centrality are measures that indicate accessibility for a network in a general, holistic view. They are selected as measures representative of general measures (compare Section 4.1) of graph structure widely used in network theory. Betweenness Centrality (BN) [294] is a measure that quantifies the importance of a node within a network based on the number of shortest paths that pass through that node. Betweenness centrality of a node v is the sum of the fraction of all-pairs shortest paths that pass through v :

$$BN(v) = \sum_{s,t \in V} \frac{\sigma(s,t|v)}{\sigma(s,t)} \quad (4.2)$$

where V is the set of nodes, $\sigma(s,t)$ is the number of shortest (s,t) -paths considering the travel time, and $\sigma(s,t|v)$ is the number of those paths passing through some node v other than s,t [295]. A node with a high betweenness centrality value acts as a bridge or connector within the network. A node with a low betweenness centrality value has limited influence on the overall network structure.

Closeness Centrality (CN) [296] is a measure that quantifies how quickly a node can be accessed from other nodes in a network. It calculates the average shortest path distance from a node v to all other nodes in the network:

$$CN(v) = \frac{n-1}{\sum_{w=1}^{n-1} d(w,v)} \quad (4.3)$$

where $d(w, v)$ is the shortest path distance between w and v considering the travel time, and $n - 1$ is the number of nodes reachable from v . A node with a high closeness centrality value is able to reach other nodes in the network more quickly. On average, a node with a low closeness centrality value takes longer to reach other nodes in the network. All centrality values are finally normalized to the range $[0, 1]$, fitted on the value range before the hazard, and transformed into the value range before and after.

Free-flow assumption accessibility indices have been used, e.g. for emergency response (Emergency Facility Accessibility Index (EFAI) [12]) or general connectivity investigations (Accessibility and Remoteness Index of Australia (ARIA) [276]). For our evacuation scenario, we slightly adapted the EFAI towards reaching emergency shelters instead of emergency facilities. An emergency facility or shelter accessibility index can consider specific facilities and critical locations to provide a more targeted assessment of accessibility in the hazard-affected areas compared to global measures. Therefore, the Shelter Accessibility Index (SAI) for an origin node v is defined as:

$$SAI(v) = \sum_S \frac{t_{vS}}{\bar{t}_S} \quad (4.4)$$

where t_{vS} is the travel time from origin v to the nearest shelter S and \bar{t}_S is the mean travel time of all origins to the respective nearest shelter S . The EFAI and ARIA define the index with a fixed threshold of three for the ratio. This threshold is employed to remove the effects of extreme values. EFAI and ARIA have predominantly been used to analyze overland road networks and focus primarily on the hierarchy of roads ranging from motorways to tertiary roads, excluding residential roads. Our study area, in contrast, includes all levels of road hierarchy. For example, residential roads contribute significantly to the total road count. This inclusion tends to reduce the mean travel time. However, in rural, mountainous regions, the travel times can be notably higher than the mean. When divided by relatively small mean values, destinations in these regions result in comparatively high index values.

Consequently, extreme values might be much more prevalent in some application scenarios, which makes it necessary to consider these values, too. Therefore, contrary to the EFAI and ARIA, we do not define the SAI with a fixed threshold of three for the ratio. A node with a low SAI value is more accessible, as it indicates that its travel time to the nearest shelter is relatively short compared to the average travel time. On the contrary, a node with a high SAI value is less accessible. Note that this measure operates inversely compared to all the other measures, where a higher value denotes greater accessibility. However, the existing and the adapted shelter indices consider a free-flow scenario. Especially for evacuation scenarios where many people leave the same location at the same time, these free-flow assumptions might be critical. As many people are prone to take the same routes (the fastest one), this can lead to congestion. These, in turn, lead to other routes being faster

than the routes that are normally the fastest in free-flow cases but are not considered in the index calculation.

Therefore, the use of an alternative routing assumption accessibility to measure accessibility is advantageous. Since a free-flow assumption is probably wrong in evacuation scenarios, it would be favorable to consider travel demand and capacity data to account for congested roads [277, 297] correctly. However, obtaining travel demand data is difficult, especially in a hazard-case scenario (compare Section 4.1). Therefore, we develop an approach that is independent of travel demand and considers routing alternatives to the respective shortest paths. The measure Alternative Routing Assumption Accessibility (ARAA) considers not only one shortest path but a selected number of k shortest paths. We assume that people would be using paths that are

1. still short (fast) compared to the shortest path, but
2. considerably different (few overlaps) to the shortest path.

following Kondo et al. [280]. The accessibility measure is therefore the sum of the number of common nodes between the k shortest selected paths. In contrast to other approaches that try to find several non-overlapping shortest paths [280], we adapt the underlying assumption to develop an approach that uses the amount of overlapping as an accessibility measure. The fewer the found paths between two points are overlapping partially, the more these points are accessible and vice versa. As a measure for the amount of overlapping of paths we use the sum of the number of common nodes between the selected paths. The ARAA for each origin node v is therefore calculated as:

$$ARAA(v) = \frac{1}{\sum_{i,j=1}^k |Set(path_i) \cap Set(path_j)|} \quad (4.5)$$

for $path_i, path_j \in paths_{vS}(t)$, $i \neq j$, where k is the number of calculated shortest paths between origin node v to the nearest shelter S considering the travel time. A node with a high ARAA value is more accessible as it has more paths leading to a shelter that are not (partially) overlapping. A node with a low ARAA value is less accessible as it has fewer paths leading to a shelter that are not (partially) overlapping.

4.4 Results

In this section, we present the results of the construction of the degraded network and the subsequent accessibility analysis of the intact and the constructed degraded road network.

Figure 4.3 shows the network degradation estimation process exemplary for the **Oakland (X)** flood application scenario. Figure 4.3, top left, shows the hazard impact zone, in this case, a 100/500-year flood map for the San Francisco Bay Area. Figure 4.3, top right, shows the road segments directly impacted by the flood in 2022/23 as extracted from VGI data (Section 3.3). Combining the degraded roads affected directly by the floods in 2022/23 and the possibly degraded roads obtained from the overlap of the impact zone with the road network, a more complete picture of the roads that may be degraded due to the hazards' impact is given. Thus, the degraded road edges and nodes of the road network in Figure 4.3, bottom, are obtained.

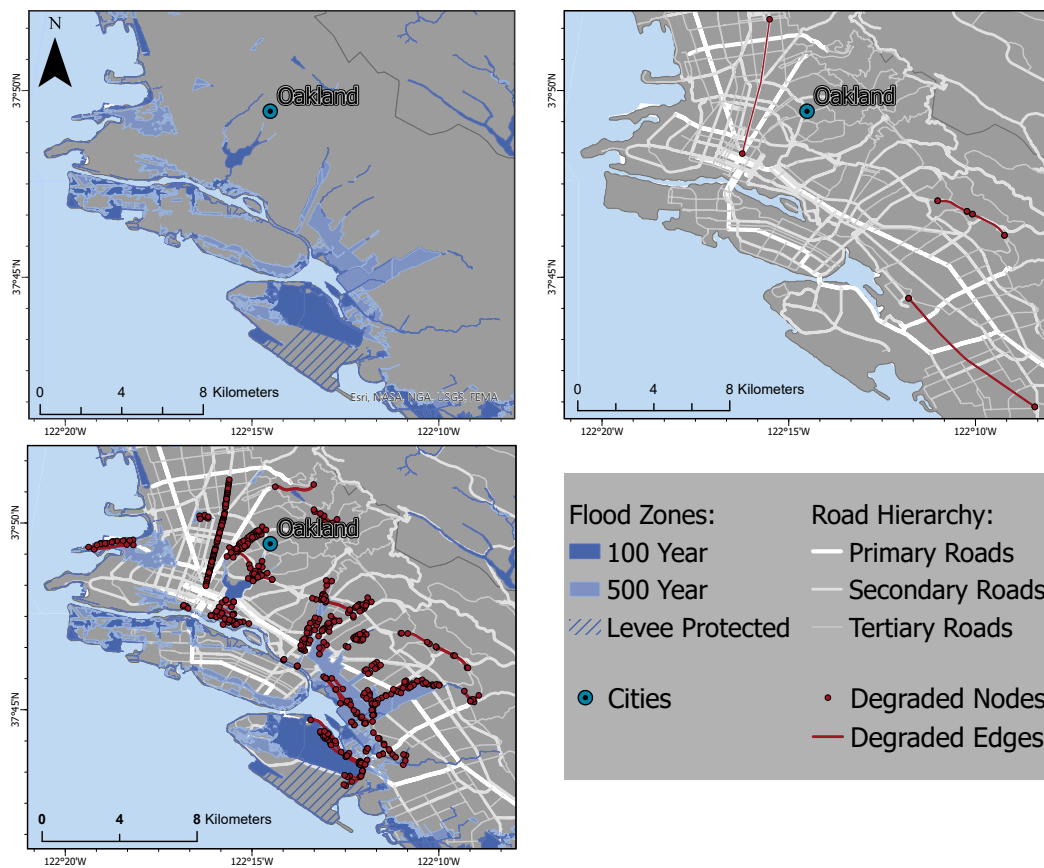


Figure 4.3.: Visualization of the impact zone of a hazard responsible for anticipated impacts on the road network (top left) and the degraded road extraction results responsible for direct impacts on the road network (top right) on the **Oakland (X)** flood application scenario. Visualization of the complete degraded roads due to the hazard's impact (roads crossing impact zone and directly extracted) (bottom) on the **Oakland (X)** flood application scenario. Data basis: © 2018 GADM. Projection: WGS84. Adapted from [1].

In the following, we will present the results of the four measures applied to the intact and degraded road network for the **Oakland (X)** study region. Furthermore, the change in network accessibility from before (intact road network) and during/after (degraded road network) a flood is presented for the four measures. The change is called the hazard's impact on road infrastructure in the following. We visualize the road network accessibility and the hazard's impact estimated by the four measures in a road map (Figure 4.4). The values of these measures were grouped into five classes defined by quintiles. For the visualization of the after-hazard accessibility the quintiles of the before-hazard accessibility are used to show possible changes. Furthermore, we present the results of the four accessibility measures for the network edges because the visualization of the node accessibility values' becomes less effective when numerous nodes overlap (compare Figure A.2 in Appendix C.1). The display of the edge accessibility values allows a more straightforward interpretation of the degraded and less accessible road sections and facilitates the assessment of the hazard's impact on the road infrastructure.

Figure 4.4, row 1, shows the results for the betweenness accessibility measure for the road network before and during/after the hazard ($Q_{0.2}$: 0.0053, $Q_{0.4}$: 0.0130, $Q_{0.6}$: 0.0300, $Q_{0.8}$: 0.0760) and the accessibility change due to the hazard impact ($Q_{0.2}$: 0.00016, $Q_{0.4}$: 0.00057, $Q_{0.6}$: 0.00170, $Q_{0.8}$: 0.00730, range [0, 0.12]) for the **Oakland (X)** application scenario. We see that this measure highlights major traffic arteries as highly accessible, while roads in residential neighborhoods are less accessible. As several major arteries become less accessible due to the impact of the hazard, we see a shift of accessibility towards other arteries. Some arteries were moderately accessible before the hazard and became highly accessible after the hazard. These become more important for the general traffic flow, as the previously important ones are less accessible. Roads in urban neighborhoods remain lowly accessible. Consequently, we see less change in neighborhood roads and in general to the east of the area, where accessibility has not changed much as no major arteries were present neither before nor after the hazard.

Figure 4.4, row 2, shows the results for the closeness accessibility measure for the road network before and during/after the hazard ($Q_{0.2}$: 0.64, $Q_{0.4}$: 0.73, $Q_{0.6}$: 0.79, $Q_{0.8}$: 0.83) and the accessibility change due to the hazard impact ($Q_{0.2}$: 0.0004, $Q_{0.4}$: 0.0005, $Q_{0.6}$: 0.0007, $Q_{0.8}$: 0.0009, range [0, 0.001]) for the application scenario. Before the hazard, using this measure, edges in the center of the study area were much more accessible, while edges at the borders of the area were less accessible. For large parts of the area, accessibility is very high, especially in the center of the study area. During/after the hazard, large parts of the area are less accessible overall, especially in the center-west. The edges in the center-east remain the most accessible. Looking at the change, we see a pattern where especially edges near the center-east area show a higher change to less accessibility. Accessibility of edges in the east remains about the same. We can see which neighborhoods are clearly affected by the impact of the hazard on the road network and therefore the change in accessibility.

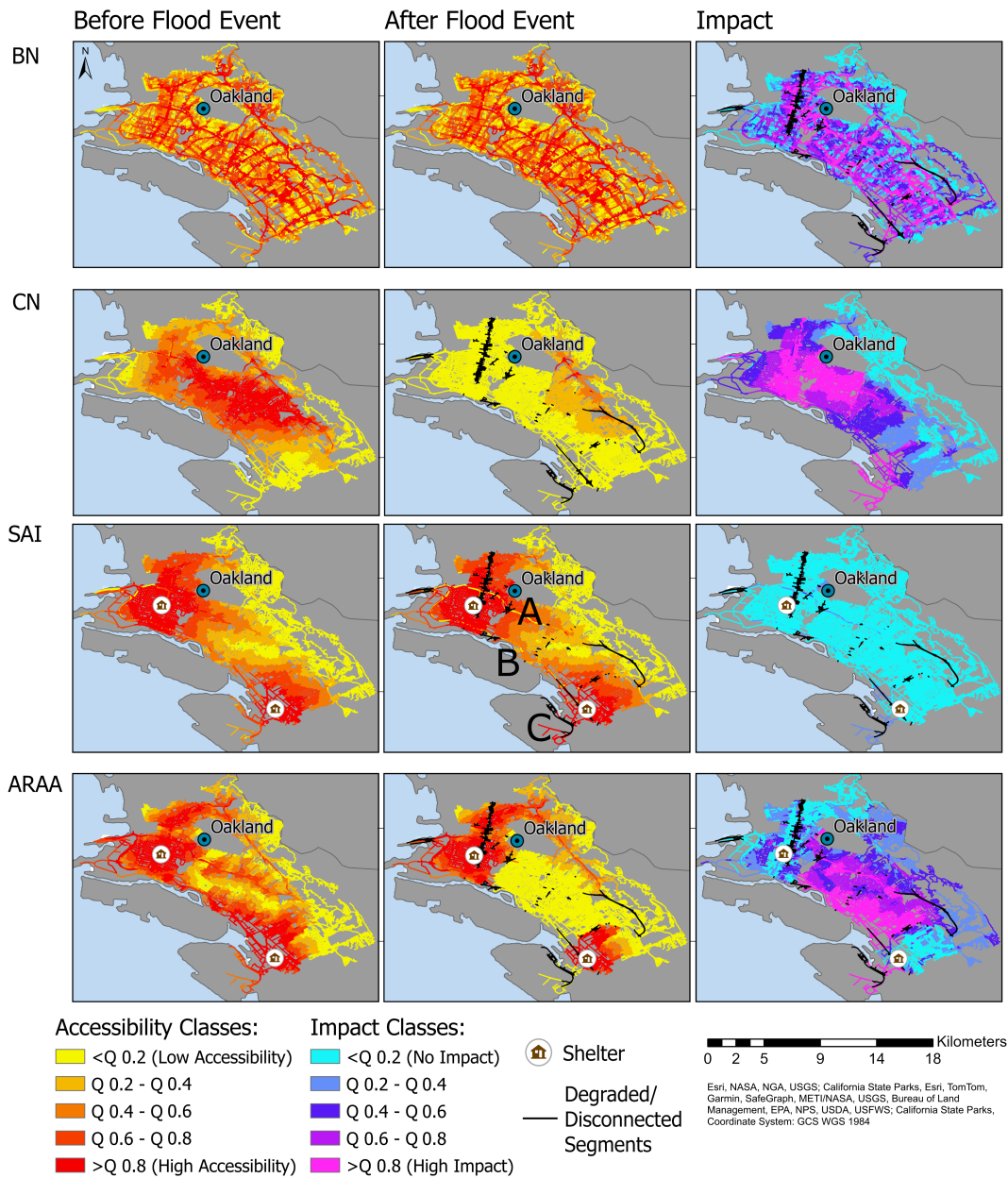


Figure 4.4.: Visualization of the betweenness centrality (BN), row 1, closeness centrality (CN), row 2, Shelter Accessibility Index (SAI), row 3, and Alternative Routing Assumption Accessibility (ARAA), row 4, measures for the flood in **Oakland** displayed for the intact network before the hazard, the degraded network during/after the hazard and the change in accessibility between the two for the network edges. Quintiles for each measure are given in the text. Note that the SAI impact values are visualized with different intervals (interval boundaries I1: 0.1, I2: 2.45, I3: 4.89, I4: 7.33). Data basis: © 2018 GADM. Projection: WGS84. Reprinted from [1].

Figure 4.4, row 3, shows the results for the SAI measure for the road network before and during/after the hazard ($Q_{0.2}$: 1.3, $Q_{0.4}$: 1.1, $Q_{0.6}$: 0.9, $Q_{0.8}$: 0.6, range [0, 10]) and the accessibility change due to the hazard impact ($Q_{0.2}$: 0.012, $Q_{0.4}$: 0.018, $Q_{0.6}$: 0.022, $Q_{0.8}$: 0.027, range [0, 9.86]) for the application scenario. Note that for this measure, the value range is inverted, where a high SAI value represents low accessibility and a low SAI value represents high accessibility. Using the shelters as destination points, we see a significantly higher accessibility of the edges that are close to the shelters. For the intact road network, the center of the study area is also comparatively highly accessible. However, the center-north is more accessible because it is more connected to the northern shelter area, mainly by a major road that runs to the south. The eastern study area is the least accessible. For the degraded network, we see almost the same pattern of accessibility overall, as places near the shelters, whose paths are not obstructed are still very accessible. However, several major arteries such as Interstate 580 and 880 (Points A and B) become much less accessible in certain segments near degraded roads. The area near the Oakland Airport (Point C) obtains higher accessibility values. The distribution of the SAI values is extremely right-skewed (median: 0.02) with 95.2% of the values lying below the value of 0.1, meaning that the accessibility of most road segments has not changed. The first interval (interval boundary I1) is defined as "no change" with values below 0.1. Four further classes are formed with equal interval boundaries (I2: 2.45, I3: 4.89, I4: 7.33). Only for a few roads, changes in accessibility have been observed around points A, B, and C and a few locations close to degraded edges.

Figure 4.4, row 4, shows the results for the ARAA measure for the road network before and during/after the hazard ($Q_{0.2}$: 5.05, $Q_{0.4}$: 6.09, $Q_{0.6}$: 7.24, $Q_{0.8}$: 9.25, range [0, 55]) and the accessibility change due to the hazard impact ($Q_{0.2}$: 0.00, $Q_{0.4}$: 0.34, $Q_{0.6}$: 2.11, $Q_{0.8}$: 3.98, range [0, 39]) for the application scenario. Similar to the SAI measure results, we see the most accessible places near the shelter points. Accessibility declines quickly when moving away from these locations. Major traffic arteries and connecting segments are shown with slightly higher accessibility values compared to purely residential neighborhood roads. The least accessible areas are some in the center, in the east, and the southeast of the study area. In the degraded network, the areas nearest to shelter locations maintain high accessibility, as degraded roads do not need to be used to reach shelters. The areas at the center become less accessible. Regarding the change in network accessibility, we observe that the areas close to the shelter locations that already had good accessibility before and after the hazard, experienced the least amount of change. The center of the study area between the two shelters is most affected by the impact of the hazard, while the central-east and northwest show moderate changes in accessibility.

4.5 Discussion

In this section, we discuss the presented study and results achieved in accessibility. We discuss the OSM data usage and the construction of the degraded dataset. The hazard's impact on the road network accessibility for the **Oakland** floods obtained from the developed methodology is discussed. Finally, we discuss the suitability of the selected accessibility measures for the task.

Road Network Data With variations of 6% compared to authority road data, OSM data are suitable for road network analysis applications due to their accuracy and completeness of relevant public spaces and infrastructure. These findings correspond with the findings of other studies that investigated the accuracies of OSM road network data, especially in urban environments [298, 299]. The relevant road network attributes, such as road distance and travel time for network analysis, have high completeness in most regions [12]. If missing, these attributes can be quickly filled using the OSMnx package [184]. Shelter locations are available with superior accuracy as they are extracted from responsible hazard management authorities.

Degraded Road Network In this scenario, the hazard impact zone is extracted using data provided by hazard management authorities. However, hazard impact zones estimated with geoinformation data (Section 3.1 and Section 3.2) can be used instead. When the overlap of the hazard impact zone with the road network is combined with the roads directly impacted by the hazard, a complete overview of the roads at risk of being degraded within the study region can be gained. The construction of the degraded network as described, as also conducted, e.g., in Guth [12], ensures the construction without connectivity errors.

Overall, we conclude that the flood hazard heavily impacts the road network of the **Oakland** study region. The degradation of many major roads is mentioned in Twitter messages texted during the 2022/23 flood. Additionally, when including minor roads that are most likely influenced as derived from the inundation zones map, large portions of the road network became degraded due to the hazard. The degradation influences the network accessibility largely. Furthermore, the road network accessibility overall changes heavily comparing the intact and the degraded road network. Large portions of the total area experience changes due to the impact of the hazard. This results from having many impacted roads in a comparatively small urban area, where impacts on major roads that traverse the city largely influence the whole road network.

Network Accessibility Four accessibility measures have been investigated. Table 4.2 shows a short summary of the advantages and drawbacks of each measure. The betweenness centrality gives a good overview of general network accessibility by highlighting important and highly accessible traffic arteries. In the context of the degradation of the road network due to a hazard, this measure balances the accessibility degradation of

Table 4.2.: Advantages and disadvantages of different accessibility measures. The following abbreviations are used: SAI - Shelter Accessibility Index; ARAA - Alternative Routing Assumption Accessibility. Reprinted from [1].

Measure	Advantages	Disadvantages
Betweenness	<ul style="list-style-type: none"> • Fastest connections easily distinguishable • In hazard case newly fastest connections easily distinguishable 	<ul style="list-style-type: none"> • No differentiation for absolute accessibility
Closeness	<ul style="list-style-type: none"> • Area-wide not punctual accessibility values • Good for degradation impact on accessibility 	<ul style="list-style-type: none"> • Accessibility depends on choice of network borders • Not for absolute accessibility estimation
SAI	<ul style="list-style-type: none"> • Adapted to situational requirements • Most important roads degradation highlighted 	<ul style="list-style-type: none"> • Reduced interpretability • Too optimistic (shortest path does not consider possible congestions)
ARAA	<ul style="list-style-type: none"> • Adapted to situational requirements • Less optimistic (realistic for congestions) • Important arteries visible 	<ul style="list-style-type: none"> • Calculation time

former major arteries with the accessibility amelioration of new major arteries. Therefore, this measure is valuable for route planning to select major arteries that can provide fast access to edges in intact road networks and degraded networks. Here, it would be valuable to display if a positive or negative change happened to the different edges. However, the measure's drawback is its tendency to ignore absolute accessibility. It highlights new arteries as highly accessible, even though they may still be less accessible than the former major arteries of the intact network.

Using the closeness centrality, it is easily distinguishable which edges in the network are able to reach other edges easily. For network degradation, the measure displays neighborhoods that become less accessible. Overall, the accessibilities in all areas are similar and less scattered and heterogeneous than for the betweenness centrality. This helps to investigate which regions might have more difficulty being reached by emergency vehicles or other places in the case of an evacuation. The drawback of this method is the major dependence of the accessibility value on the selected investigation area. Edges in the center of the selected area are, by default, more accessible. This measure computes

a very universal picture, with almost all road experiencing a drop in accessibility due to the degraded roads. Therefore, the measure is suitable to display changes in accessibility accurately, but needs to be used with caution for absolute accessibility analyses.

Our betweenness and closeness centrality findings correspond with other studies that used those measures for network accessibility analysis (e.g., [282, 283, 284]). These measures provide valuable insights into networks' structural characteristics and efficiency and are fast and easy to apply to any kind of network. Betweenness and closeness centrality are global measures that capture the overall importance of nodes in the network very well. However, they heavily rely on the network structure. Due to natural hazards, the degraded road network has an altered network structure. Therefore, betweenness and closeness centrality values may change significantly (betweenness centrality for major arteries, closeness centrality overall, compare Section 4.4), even for minor disruptions. Minor changes can completely alter the selected paths, leading to different nodes being much more important from a theoretical perspective. Viewed from a practical point of view during a natural hazard, it is important to recognize that certain regions or specific roads that hold significance in the intact network may retain their critical importance even when assigned lower accessibility values in a degraded network.

Accessibility indices can be adapted to situational requirements, like immediate emergency response (evacuations or emergency facility access [12]) or general connectivity investigations (remoteness of places [276]). These indices can consider specific facilities and critical locations to provide a more targeted accessibility assessment during a natural hazard. Compared to the previous measures, the SAI is adaptable to situational requirements for route planning investigations to provide a more targeted assessment of the accessibility of regions. However, the inverse definition of the SAI (like EFAI and ARIA) could be more optimal and this measure is less straightforward and more challenging to interpret. Adapting the SAI to avoid using a fixed threshold (see Section 4.3) enhances its usability for networks with all hierarchies of roads, especially when compared to EFAI and ARIA [195, 276]. However, the SAI still follows an extremely right-skewed distribution and is not optimal for the visualization of accessibility and especially its changes. Only few major arteries (Points A and B in Figure 4.4, row 3) and few other roads especially in the South (around Point C) experience changes. Additionally, due to the definition of this measure, using the mean travel time value, roads near the Oakland Airport (Point C in Figure 4.4, row 3) become more accessible compared to the mean, as the mean value becomes larger overall. Furthermore, considering only one shortest path, the measure can be seen as too optimistic in evaluating the accessibility impact. In reality, when evacuation orders are given, and all people decide to choose the depicted shortest path, the accessibility of this path would drop rapidly. This would lead to congested scenarios where free-flow measures can not estimate accessibility.

The ARAA can be adapted to situational requirements as much as the SAI, e.g., for shelter or emergency facility accessibility. With the ARAA, major traffic arteries, as well as regional

clusters of accessibility, can be easily detected. In the context of degradation of road networks, the ARAA can give clear statements about areas of change in accessibility. For the impact, the ARAA shows a very detailed and differentiated accessibility value pattern for the impacted regions (center of study region). Only very few edges closest to the shelter locations are considered highly accessible when assuming congestions. The ARAA can be adjusted to simulate congestion severity by augmenting the number of k paths to be computed. Furthermore, due to the use of alternative routes, it is a more realistic measure for congested scenarios than free-flow measures [195]. Therefore, this measure is valuable for route planning in hazard scenarios compared to other accessibility-based measures [287]. Additionally, it is valuable compared to methods that rely on more complex and often non-available data like traffic data (e.g., [277, 297]). However, due to the higher number of paths to be calculated one drawback of the ARAA is the longer calculation time.

Overall, the measures focus on different attributes of a network, e.g., connection function of a node or reachability to any other node. Furthermore, they consider different scenarios, e.g., general accessibility or evacuation scenarios. A direct comparison of outcomes from these measures is unfeasible, given their distinct definitions of *accessibility* stemming from divergent attributes and application uses. As a result, their comparability needs to be improved. Nevertheless, the measures complement each other by providing divergent perspectives on road network accessibility. These contribute to a more comprehensive understanding of the accessibility dynamics within the road network during natural hazards and enable a nuanced evaluation of the network's vulnerabilities in hazard management.

However, for the evaluation of the developed network accessibility analysis, the comparison to more detailed network analysis models, for example, for a defined hazard where traffic information is available, would be favorable. For example, including road capacity data in congestion scenarios using detailed modeling [300, 301] can give more detailed insights into network accessibility. The complexity of modeled parameters concerning network accessibility could be increased to a high degree according to the desired accuracy and detailing of accessibility analysis. Furthermore, a straightforward model for evacuation scenarios is used in this case: we assume that people are evacuated to two shelters. In reality, evacuation scenarios are much more complex, incorporating, e.g., scenarios where people choose their evacuation destination or where roads are blocked to regulate traffic [302]. Such scenarios are defined, e.g., in the *Sea to Sky Multimodal Evacuation Plan* developed by the District of Squamish and the Resort Municipality of Whistler [303]. However, in our framework, the choice of destinations can easily be adapted according to necessities and each authorities' evacuation plans.

4.6 Conclusion and Integration in Framework

For a flood application scenario, it is demonstrated how the presence of hazard impacts affects road conditions and overall accessibility within the network. The analysis of hazard impacts on road networks is based on overlaying impact zones onto road network datasets (Section 4.3.1), revealing the locations where road functionality may be compromised (Section 4.3.2). Additionally, directly extracted road impacts are considered (Section 3.3). Overlapping the road network with the hazard impacts and subtracting roads that are marked as impacted from the intact road network proves to be an effective approach creating a *degraded* road network. In the following, the degraded network serves as the basis for the accessibility analyses.

Different measures of accessibility change are employed to assess the network's performance before and during the hazard, all of which are valid for road network impact analysis (see Section 4.5). Two standard accessibility measures ([294, 296]) are benchmarks for evaluating and contrasting our developed approaches. Specifically, we introduced an alternative routing assumption accessibility measure that considers anticipated congestion scenarios. All employed measures achieve the objective of estimating road network accessibility without using additional traffic data. Therefore, they are all suitable for road network accessibility analysis independently of restricted global data availability on hazard-induced road network impacts. In total, the use of each measure is justified, as each measure could demonstrate the accessibility change due to the degradation of the network. However, their combination and comparison give valuable insights. In summary, this framework offers a quick and straightforward assessment of natural hazard impact on road networks. It serves as an initial step for disaster risk management planning shortly after a hazard event. The proposed approaches are particularly valuable due to their applicability using only degraded road network information without any additional data sources.

While this section focuses explicitly on a flood hazard, it contributes to the broader framework for the evaluation of road accessibility under natural hazard impacts. Demonstrating how the presence of hazard impacts affects road accessibility in a road network, the developed methodology can easily be transferred to analyze of road networks impacted by various other hazards.

4.7 Synthesis on the Second Module

The **Module II** represents the second step in a framework for assessing the impact of natural hazards on road infrastructure. This module analyzes the effects of natural hazards impacts on road infrastructure. It builds upon the direct road impacts extracted in Chapter 3 and, in the selected application scenario, on the flood impact zone from a 100/500-year flood hazard map. The analysis of hazard impacts on road networks is based on overlaying

the employed impact zones and direct impacts onto road network datasets. The *degraded* road network is created, overlapping the road network with the hazard impact (zones). Then, the degraded network serves as the basis for the accessibility analyses. This module employs various methods to analyze accessibility changes due to hazard impacts. These methods include established theoretical measures on the one hand. These are betweenness centrality and closeness centrality, which are rooted in graph theory. On the other hand, it utilizes a free-flow assumption accessibility index and a congested-flow assumption accessibility measure. For a flood hazard, all of them are valuable for road network impact analysis.

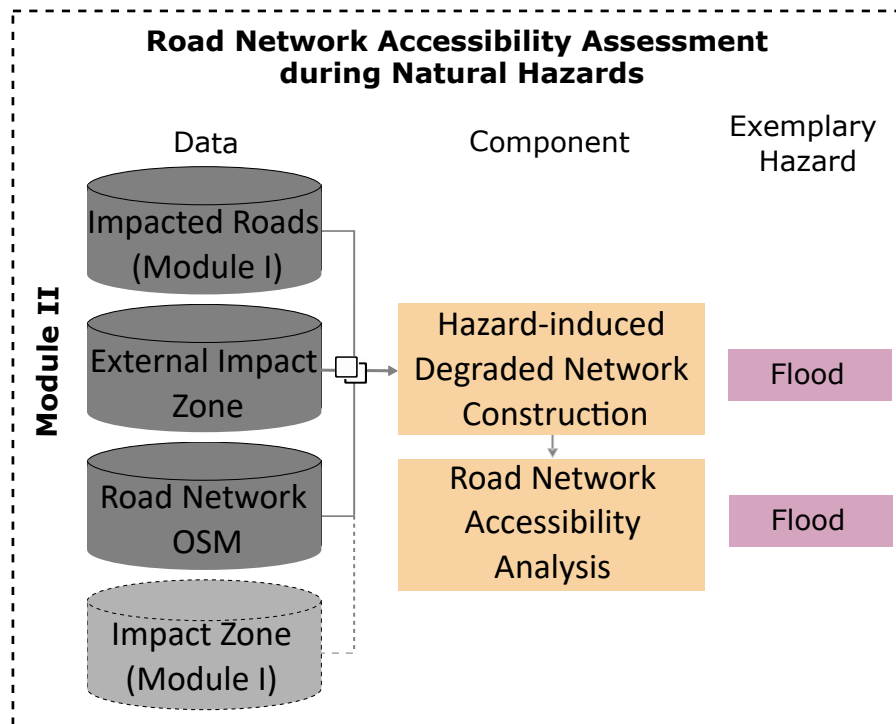


Figure 4.5.: Visualization of Module II for the road network accessibility assessment during natural hazards. The degraded network construction is based in the information of the impacted roads as extracted in Module I and the External impact zone overlapped with Open Street Map (OSM) road network data. Impact zones estimated in Module I could be employed. The road network accessibility analysis is based on the constructed network.

Figure 4.5 displays the components developed in **Module II** to assess road network accessibility during natural hazards. The Module is subdivided into the hazard-induced degraded network construction based on the overlaying of impacts and road network data and the road network accessibility analysis. The developed **Module II** is designed to be easily transferable to different hazard types affecting other road networks (see Chapter 5). The components (hazard-induced degraded network construction and road network accessibility analysis) could also be applied independently. More details are discussed in Section 5.4.2).

Like [Module I](#), [Module II](#) relies exclusively on openly available data, namely OSM data and the impacts as extracted from openly available geoinformation data. All accessibility measures achieve the objective to estimate road network accessibility without using additional traffic data. Therefore, the framework can tackle the challenge of restricted global data availability on road network impacts due to hazard occurrence. The impact zones for the **Oakland** floods have not been extracted using the methodology developed in [Module I](#) (Section 3.1, Section 3.2), yet. However, the developed methodology could be used in its entirety for the estimation of hazard impact zones for the further use in [Module II](#). Using only the impact (zones) determined in [Module I](#), before applying the [Module II](#), a complete framework for assessing the impact of natural hazards on road infrastructure can be constructed (see Chapter 5).

Complete Framework: Application to Bobcat Wildfire

This chapter includes elements from

[43] J. Florath, J. Chanussot, and S. Keller. “Utilizing Volunteered Geographic Information for Real-Time Analysis of Fire Hazards: Investigating the Potential of Twitter Data in Assessing the Impacted Areas”. In: *Fire* 7.1 (2023), p. 6

marked with an [orange line](#). This chapter also includes elements from

[1] J. Florath, J. Chanussot, and S. Keller. “Road Accessibility during Natural Hazards Based on Volunteered Geographic Information Data and Network Analysis”. In: *ISPRS International Journal of Geo-Information* 13.4 (2024), p. 107

marked with a [green line](#).

The developed methodology for the assessment of natural hazards impacts on road infrastructure comprising of [Module I](#) and [Module II](#) is applied exemplary for the application scenario of the **Bobcat (XI)** wildfire hazard. This chapter summarizes the entire process for the assessment of natural hazards’ impacts on road infrastructure. It includes all the steps as presented in [Module I](#) (Chapter 3) and [Module II](#) (Chapter 4). It begins with the presentation of the study region in Section 5.1, followed by the results applying the methods of [Module I](#), the determination of hazard impact zone and road impact extraction in Section 5.2. Then, the results applying the methods of [Module II](#), the road network accessibility analysis, are presented in Section 5.3. Finally, the total framework for the assessment of natural hazards impacts on road infrastructure for the application scenario is discussed Section 5.4.

5.1 Application Scenario

The developed methodology for the assessment of natural hazards impacts on road infrastructure is applied exemplary for the application scenario of the **Bobcat** wildfire hazard (XI). The **Bobcat** wildfire occurred in 2020 in the Angeles National Forest, CA, US. Figure 5.1 visualizes the location of the fire. The **Bobcat** wildfire started in early September

2020 in the Angeles National Forest, a large mountainous area situated near Los Angeles. It predominantly stroke in the central area of the San Gabriel Mountains, which include the Angeles National Forest. Due to a combination of dry vegetation, strong winds, and challenging firefighting conditions, the wildfire escalated quickly in size and intensity. The fire stands out as one of the most extensive wildfires documented in the history of Los Angeles County. It was fully contained only on December 18. The fire initially spread out in a southern direction, which lead to evacuation directives for inhabitants in Sierra Madre, Monrovia, Bradbury, and Duarte. Additionally, evacuation alerts were provided for residents in Arcadia, Pasadena, and Altadena. Table 5.1 shows the different characteristics concerning the fire as well as tweet information for this hazard.

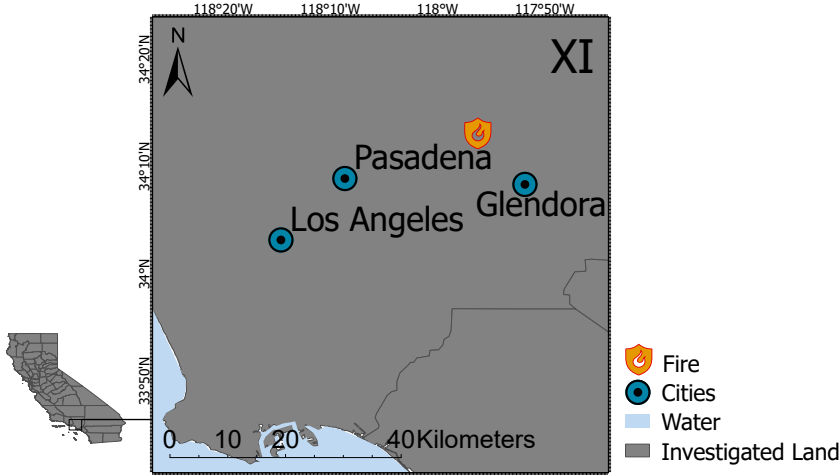


Figure 5.1.: Overview of the cases study hazard location for the **Bobcat (XI)** fire. Data basis: © 2018 GADM. Projection: WGS84.

Table 5.1.: Overview of fire characteristics and characteristics influencing tweet data for the Bobcat Fire. Adapted from [1].

Location	Bobcat Fire
Fire Starting Date	06/09/2020
Fire Duration	-19/10/2020 (43 days)
Total Fire Area	~ 469km ²
Fire Behaviour	98km ² within 4 days, +/- constant spreading
Landcover	Forest/shrub landcover, mountainous, no population
Population Density/ Distribution	High density, irregular distribution around possible fire area
Tweet Behavior	More tweets, less place information in text
Agencies (Fire/Road)	Using twitter
First Available Remote Sensing Data	4 days after fire start (10/09/2020)

5.2 Module 1

In the following, the three developed methodologies of [Module I - Natural Hazard Impact Determination with Geoinformation Data](#) are applied to the **Bobcat (XI)** application scenario. These methodologies are: the natural hazard impact zone estimation using RS data (Section 5.2.1) and VGI data (Section 5.2.2) and the road impact extraction from VGI (Section 5.2.3).

5.2.1 Natural Hazard Impact Zone Estimation with Remote Sensing Data

As documented in Table 5.1 the first Sentinel-2 high resolution RS image is available four days after the fires ignition on 10/09/2020. A combined fire and burned area detection approach using the supervised ML model 1D-CNN is applied for the natural hazard impact zone estimation with Sentinel-2 satellite images (compare Section 3.1). Figure 5.2 shows the extracted burned and fire areas. The methodology extracts the areas that are burned and the areas affected from currently burning fires in a very detailed 10 m resolution. Burning fires occur on the edges of the already burned area, where they develop towards

newly burnable materials. These areas are comparatively small compared to the already burned area.

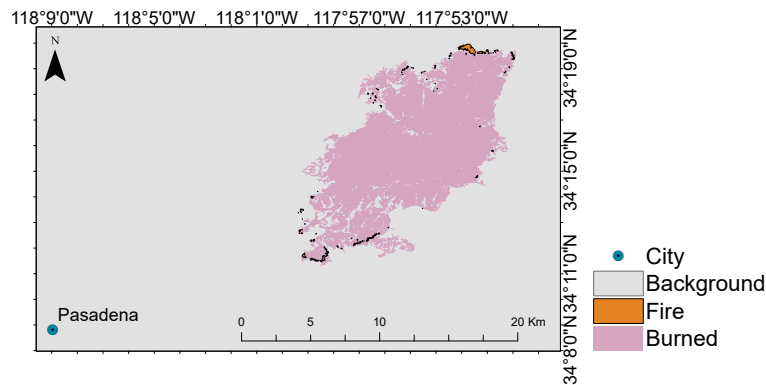


Figure 5.2.: Visualization of the results of the hazard impact extraction (burned area and fire area) from remote sensing data for the selected natural hazard, the **Bobcat** wildfire (XI). Data basis: © 2018 GADM. Projection: WGS84. Adapted from [43].

5.2.2 Natural Hazard Impact Zone Estimation with Volunteered Geographic Information Data

There is a time gap of four days until high-resolution RS data becomes available after the fire. VGI data can be used to estimate the natural hazard impact area (Section 3.2) of the **Bobcat** (XI) fire for the days of 06/09 to 10/09 [304]. Tweet text and location data for these specific dates are extracted to subsequently apply the methodology for natural hazard impact zones estimation using VGI data to the **Bobcat** fire. Figure 5.3 shows the results of the hazard impact zone estimation using VGI data for the **Bobcat** wildfire. By visual inspection, it can be verified that the estimated hazard impact zone agrees with the extent of the impact zones estimated by RS data on a coarse level, while differences are observed on a finer level. The barycenter lies within the fire impact zone estimated by RS data (Figure 5.3 A) and corresponds with a distance of approximately 3 km to the pseudo-reference's center. The estimated fire impact zones using LVA (Figure 5.3 B) and buffer approaches (Figure 5.3 C) coincidences with the southern part of fire zone estimated by RS data. Consequently a similar picture is observed for the combined approach (Figure 5.3 D). The center of the VGI estimated area and the RS estimated area vary by approximately 6 km. The results show that the fire location can be approximately estimated using VGI data and indicate where people are majorly affected by the hazard.

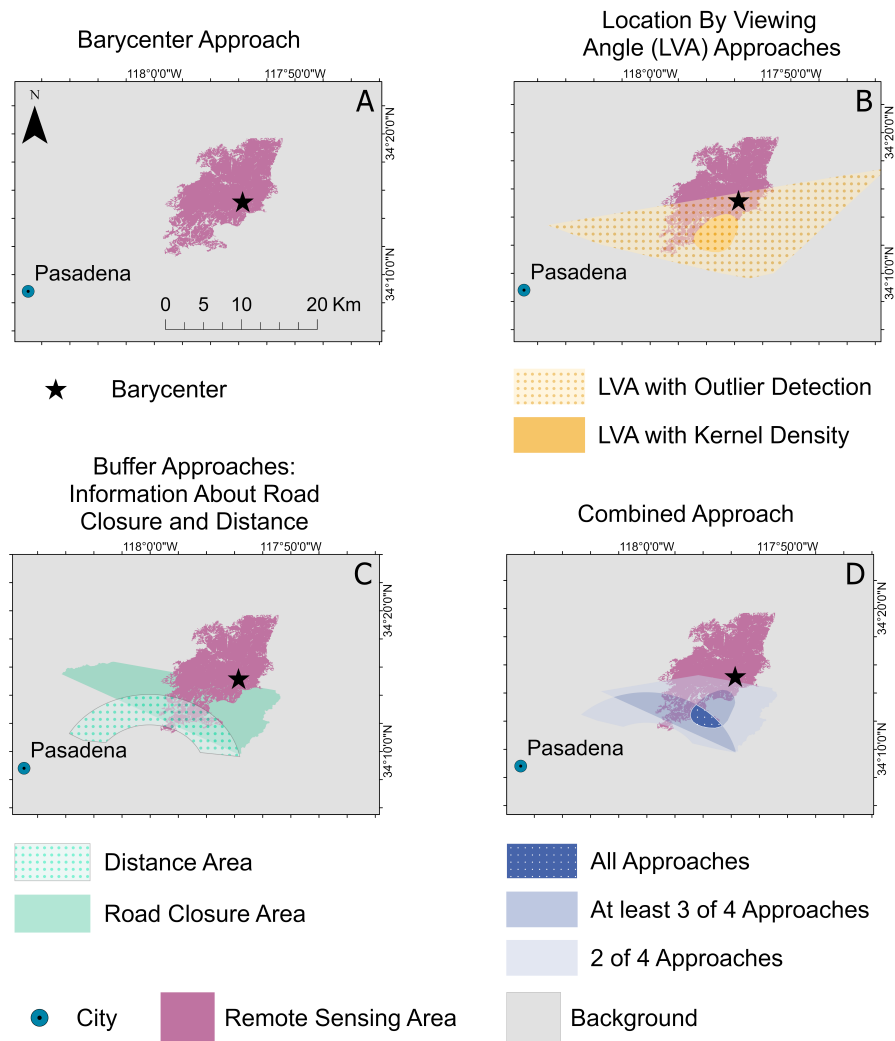


Figure 5.3.: Visualization of the results of the hazard impact extraction from Volunteered Geographic Information (VGI) data for the selected natural hazard, the **Bobcat** wildfire (XI). Data basis: © 2018 GADM. Projection: WGS84. Adapted from [43].

5.2.3 Road Impact Extraction from Volunteered Geographic Information Data

In the context of road network analysis one significant application of VGI is the extraction of road impact information and its geolocalisation in addition to hazard impact zone estimation. Extracting tweet texts corresponding to the time of natural hazard events, scanning the text data for road impact information, and geocoding (Section 3.3) allows the extraction of roads degraded by the hazards' impacts. For the **Bobcat** (XI) wildfire, we obtain a total of 303 messages that contain road location information. However, most texts contain road information that does not consider degradation from the investigated fire but, e.g., general road closures. Since we want to concentrate on roads degraded from

hazard impact, we choose only texts associated with fire. Furthermore, the degradation of the same road is reported several times if the hazard lasts several days. After removing messages with identical information, we retain two messages associated with the **Bobcat** fire. From these two messages, road extraction is possible. Figure 5.4 displays the different extracted roads for the application scenario. We observe that we obtained road segments and corresponding intersection locations for the text information data. For the wildfire, only a few non-identical closed or damaged roads are mentioned in tweet texts, and therefore, the number of extracted road segments is low. Furthermore, we observe that significant roads are mainly extracted as they are talked about in tweets from road agencies and hence extracted as degraded.

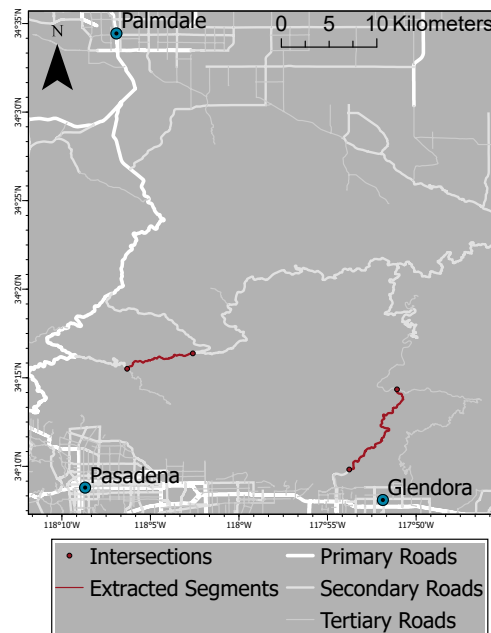


Figure 5.4.: Visualization of degraded roads extracted from Volunteered Geographic Information (VGI) text information for the **Bobcat** fire (XI). Data basis: © 2018 GADM. Projection: WGS84. Adapted from [1].

5.3 Module 2

In this section, [Module II - Road Network Accessibility Assessment during Natural Hazards](#), the second part of the framework for the assessment of natural hazards' impact on road infrastructure, is applied to the **Bobcat** (XI) application scenario. The module considers the impacts caused by the **Bobcat** (XI) wildfire as determined in [Module I](#) (Section 5.2). The module consists of the introduction of the road network data for the **Bobcat** wildfire (Section 5.3.1) and the construction of the degraded network (Section 5.3.2) from the impacts of the hazard extracted in Section 5.2. Finally, the network accessibility under the hazard impacts is evaluated (Section 5.3.3).

5.3.1 Road Network Data

A reasonable region of interest is selected for the application scenario. The OSM network graph's nodes and edges within this region are extracted with the OSMnx [184] python package (compare Section 4.3.1). For the **Bobcat (XI)** scenario the selected region is the region within the bounding box of 118,2063881°W 34,5815616°N (top left corner) and 117,6357117°W 34,1330156°N (bottom right corner). This selection covers the Angeles National Forest as well as the surrounding urban areas (North: Palmdale, South: Arcadia, Azusa, parts of Pasadena). The reason for these selections is the availability of a reasonable number of emergency shelters (two) that can be reached in this region, which is essential for our network accessibility measures. Table 5.2 displays the selected shelter information and the number of edges and nodes.

The road network of this selected area has a high number of nodes and edges compared to the **Oakland (X)** flood application scenario (Table 4.1 in Section 4.3.1). Some preprocessing steps are necessary to deal with this high number of edges and nodes. As each node would serve as a starting point for the measures of accessibility calculation, the calculation would require too much computation time. Therefore, we preprocess the network data and thin the node data used as starting points. We consider only nodes from roads of high hierarchy levels, not including nodes of residential roads as starting points. This technique aims to reduce the density of data points, allowing for a more manageable dataset while preserving crucial spatial information. Note that the accessibility calculation does consider all nodes and edges to find the shortest paths; only the amount of starting points is reduced.

Table 5.2.: Overview of network analysis data for the **Bobcat** wildfire (XI). Adapted from [1].

Shelter locations	N° Edges	N° Nodes
Palmdale High School, Santa Anita Park	36.634	14.319

5.3.2 Degraded Road Network Construction based on Hazard-Induced Impact

This section links **Module I**: the determination of natural hazard impacts, and **Module II**: the road network analysis. The road network degradation is a result of the hazard-induced impacts. The degraded road network is constructed (compare Section 4.3.2) by overlaying the hazard impacts on the intact road network of the study region. Hazard impacts are described by hazard impact zones estimated using RS data (Section 5.2.1) and VGI data (Section 5.2.2) and degraded roads extracted from VGI data (Section 5.2.3).

Figure 5.5 shows the overlay process for the **Bobcat (XI)** wildfire application scenario. Figure 5.5, top left, shows the hazard impact zones as estimated using Sentinel-2 RS data

(Section 5.2.1) and Twitter VGI data (Section 5.2.2). Figure 5.5, top right, shows the degraded road segments as extracted from VGI data (Section 5.2.3). Combining the determined hazard impacts and overlapping them with the road network, the degraded road edges and nodes anticipated for being at risk for hazard impact are obtained in Figure 5.5, bottom. Note, that the entire road segment is designated as *degraded* even in cases where only one end node is situated within the hazard impact area.

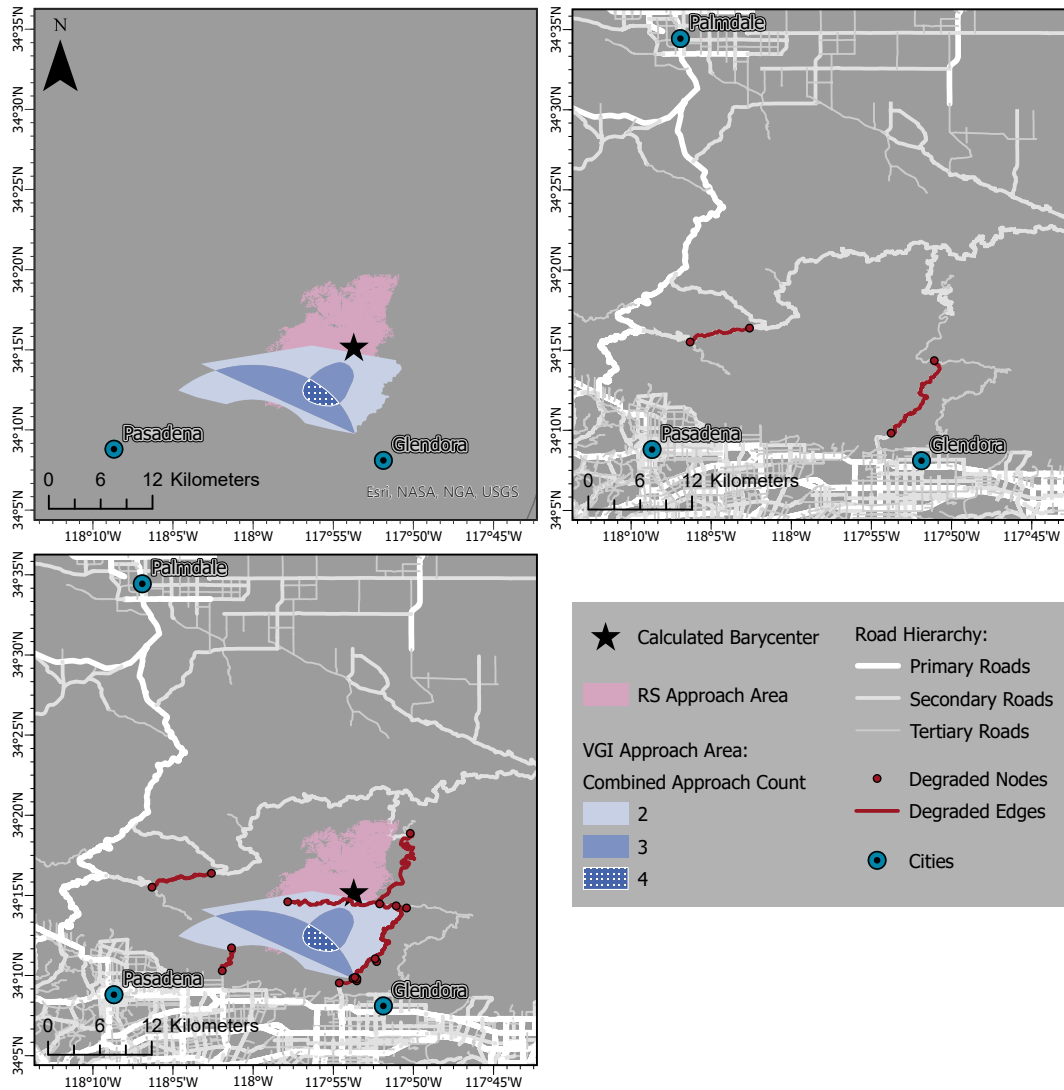


Figure 5.5.: Visualization of the hazard impact zones as estimated using remote sensing (RS) data and Volunteered Geographic Information (VGI) data (top left) for the **Bobcat** wildfire application scenario (XI). The barycenter and the results of the combined approach, giving count numbers of how many distinct VGI approaches overlap, are displayed. The degraded roads extracted from VGI data (top right) and the degraded road edges and nodes at risk for hazard impact constructed by overlaying (bottom) are displayed. The road network is limited to primary to tertiary roads for visualization purposes. Data basis: © 2018 GADM. Projection: WGS84. Adapted from [1].

5.3.3 Road Network Accessibility Analysis

The road network accessibility analysis methodology (compare Section 4.3.3) is applied to the intact and degraded network depicting the roads in the region where the **Bobcat (XI)** wildfire happened. In the following, we will present the results of the four measures applied to the intact Angeles National Forest road network before the fire and the degraded road network affected by the fire. Furthermore, the change in network accessibility from before and during the fire is subsequently presented for the four measures. Accessibility and impact value visualization are conducted as described in Section 4.4.

Figure 5.6, row 1, shows the results for the betweenness accessibility measure for the road network before and during/after the hazard ($Q_{0.2}$: 0.0003, $Q_{0.4}$: 0.0008, $Q_{0.6}$: 0.0021, $Q_{0.8}$: 0.0081) and the accessibility change due to the hazard impact ($Q_{0.2}$: 0.00022, $Q_{0.4}$: 0.00064, $Q_{0.6}$: 0.00120, $Q_{0.8}$: 0.00330, range [0, 0.002]) for the application scenario. Similar to the Oakland application scenario results, the **Bobcat (XI)** application scenario results reveal that this metric highlights major traffic arteries as having high accessibility. On the other hand, roads within residential neighborhoods and rural mountainous regions, which do not serve as significant city connectors, exhibit lower accessibility levels. The wildfire event does not significantly affect the condition of the road network. However, three road segments on both sides of the degraded segment of the Angeles Crest Highway (Hwy) (Point A) experience degradation, resulting in decreased accessibility. A minor alteration in accessibility is observed for a few road segments situated in the southern part of the Angeles National Forest (around San Gabriel Canyon Road, Point B) and the urban area close to degraded edges.

Figure 5.6, row 2, shows the results for the closeness accessibility measure for the road network before and during/after the hazard ($Q_{0.2}$: 0.63, $Q_{0.4}$: 0.67, $Q_{0.6}$: 0.76, $Q_{0.8}$: 0.80) and the accessibility change due to the hazard impact ($Q_{0.2}$: 0.000010, $Q_{0.4}$: 0.000025, $Q_{0.6}$: 0.000059, $Q_{0.8}$: 0.00027, range [0, 0.00042]) for the application scenario. For the intact road network, a cluster characterized by high accessibility is situated in the southwest region. In contrast, the accessibility in the northern region is comparatively lower according to this metric. The accessibility of connecting road segments between the south and north regions is moderate, depending on the road's proximity to the respective clusters. In the degraded network, for road segments crossing the Angeles National Forest and linked to degraded segments, a decrease in accessibility exists. Looking at the change, the Angeles Crest Hwy (Point A) and connecting edges in the Angeles National Forest are significantly affected along its length. A few connecting road segments leading to the Angeles Crest Hwy and a few mountain roads connected to the San Gabriel Canyon Road (Point B) are also impacted.

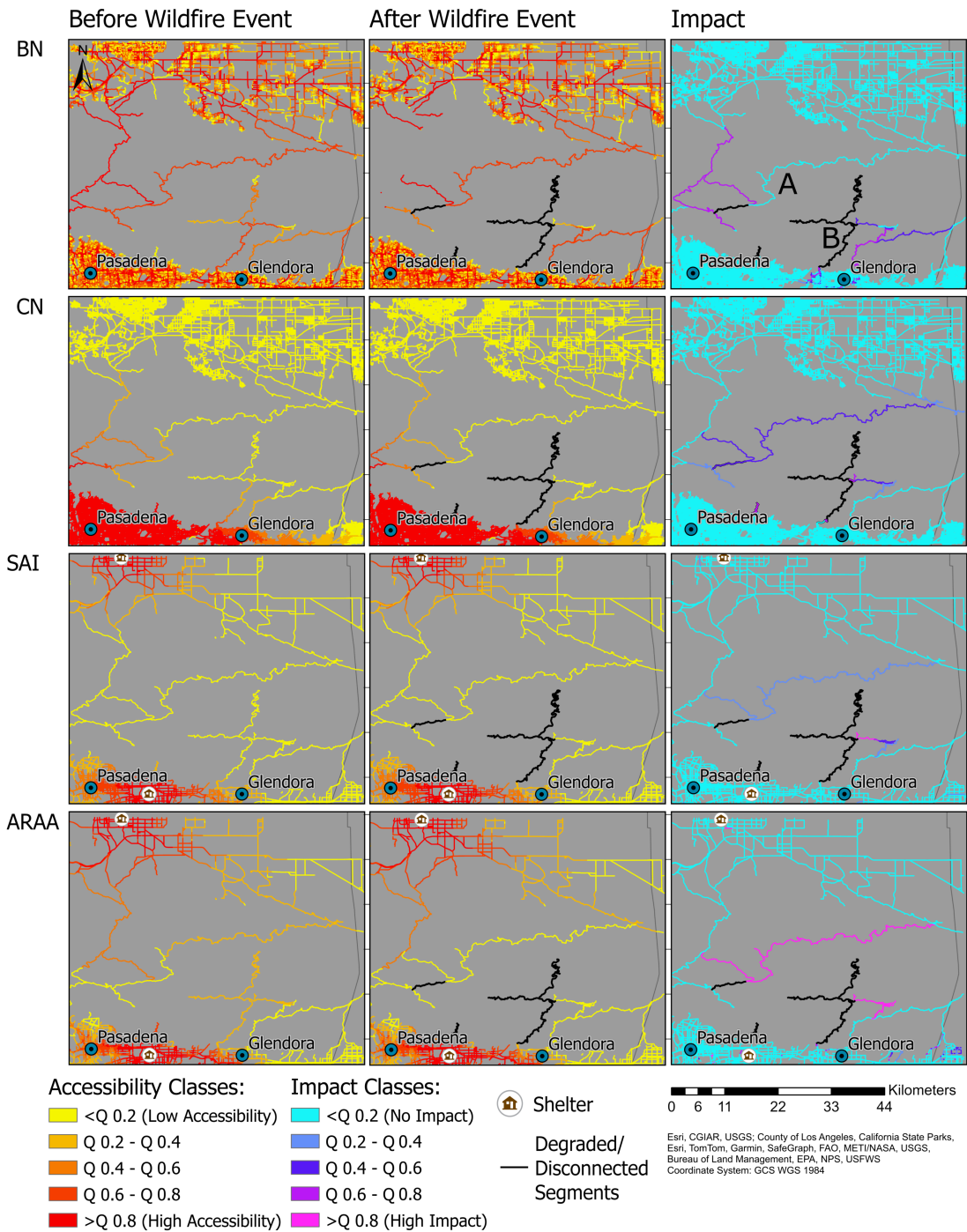


Figure 5.6.: Visualization of the betweenness centrality (BN), row 1, closeness centrality (CN), row 2, Shelter Accessibility Index (SAI), row 3, and Alternative Routing Assumption Accessibility (ARAA), row 4, measure for the **Bobcat** wildfire (**XI**) displayed for the intact network before the hazard, the degraded network during/after the hazard and the change in accessibility between the two for the network edges. Quintiles for each measure are given in the text. Note that the SAI impact values are visualized with different intervals (interval boundaries I1: 0.1, I2: 0.58, I3: 0.93, I4: 1.27). Data basis: © 2018 GADM. Projection: WGS84. Reprinted from [1].

Figure 5.6, row 3, shows the results for the SAI measure for the road network before, during, and after the hazard ($Q_{0.2}$: 1.49, $Q_{0.4}$: 1.03, $Q_{0.6}$: 0.81, $Q_{0.8}$: 0.53, range [0, 4.79]) and the accessibility change due to the hazard impact ($Q_{0.2}$: 0.0012, $Q_{0.4}$: 0.0018, $Q_{0.6}$: 0.0023, $Q_{0.8}$: 0.0033, range [0, 1.63]) for the application scenario. Note that for this measure the value range is inverted. A high SAI value represents low accessibility and a low SAI value represents high accessibility. For this measure, we rely on the thinned node data (as described in Section 5.3.1), which does not include residential roads' nodes and edges as starting points. Residential neighborhood roads in the northeastern study area are not displayed. Using the shelters as destination points for this measure, we see significantly higher accessibility of the edges near these shelter locations. For the intact road network, edges in a relatively large radius around the shelters exhibit notably high accessibility levels. The accessibility levels decline as one moves farther away from these shelter points, particularly in the mountainous areas. For the degraded network, the analysis reveals no visualized fluctuations in accessibility. Nonetheless, when assessing the visual representation of the change based on the suitable tailored intervals "no change" (interval boundary I1: 0.1) and equal intervals on the remaining values (I2: 0.58, I3: 0.93, I4: 1.27) (explanation see Section 4.4), it becomes apparent that there is a marginal decrease in accessibility along the Angeles Crest Hwy (Point A) and its connecting edges. Moreover, the connecting route to the San Gabriel Canyon Road (Point B) in the Angeles National Forest exhibits a substantial decrease in accessibility.

Figure 5.6, row 4, shows the results for the ARAA measure for the road network before, during, and after the hazard ($Q_{0.2}$: 4.44, $Q_{0.4}$: 5.92, $Q_{0.6}$: 7.20, $Q_{0.8}$: 9.34, range [0, 91]) and the accessibility change due to the hazard impact ($Q_{0.2}$: 0.000001, $Q_{0.4}$: 0.039, $Q_{0.6}$: 0.045, $Q_{0.8}$: 0.267, range [0, 2.31]) for the application scenario. For this measure, we also rely on the thinned node data, which does not include residential roads' nodes and edges as starting points and are, therefore, not displayed. Using the shelters as destination points for this measure, we see significantly higher accessibility of the edges near these shelter locations. Edges in the mountainous areas still have comparatively high accessibility values as more alternative routes to shelters can be found here, moving towards both valley sides. In contrast, urban areas, e.g., in the South-East, mostly connected to only one shelter without alternative routes, are least accessible. For the degraded network, it is again challenging to visualize the slight accessibility decrease effectively. The impact visualization shows that the Angeles Crest Hwy (Point A) and connecting edges to degraded edges overall are highly affected.

5.4 Discussion

In this section, the applicability of the developed framework for the assessment of the natural hazard's impact on road infrastructure on the **Bobcat** application scenario hazard (Section 5.4.1) and the transferability of the framework (Section 5.4.2) are discussed.

5.4.1 Applicability of Framework on Bobcat Fire

In the **Bobcat (XI)** application scenario example, the estimation of the hazard impact zones using both RS and VGI data sources is demonstrated. RS data, provide a high level of accuracy for the precise estimation of the fire and burned areas within the Angeles National Forest near Los Angeles. The applied 1D-CNN is suitable for the task and estimates very detailed burned and fire areas, similar to the estimation on the independent dataset of **central Spain (III)** in Section 3.1. Fire areas are a lot smaller and located around the borders of the burned area, as the RS imagery captures only one point in time which depicts the current flames progress. At the moment of capture, the fire spreads primarily towards the North and the South. RS data were only accessible four days after the wildfire's start, a similar time range to the RS data investigated in Section 3.2. The VGI-based methodology proves valuable to extract hazard impact zones in the meantime. Using this technique for the **Bobcat** fire, the barycenter lies well within the RS area, due to a distribution of VGI data mainly influenced by population density, whose effects we removed by weighting. Nevertheless, the impact zone estimated by VGI data lies to the south of the RS area. This can have several reasons, like the significantly higher population density in the city of Los Angeles, where people are more affected by the hazard. These results are similar to the investigated **Landiras fire (V)** (Section 3.2). Additionally, due to the mountainous regions of the Angeles National Forest in the northern area, less VGI data are available in this part. Finally, the fire developed from the south to the north, spreading in the days until RS imagery was obtained a few days later.

Moreover, the developed methodology enables the extraction of the direct impacts on road infrastructure for the **Bobcat** wildfire application scenario. In this application scenario, a more limited amount of non-repeating text information about road conditions during the hazard is available compared to the investigation on the **San Francisco Bay Area (IX)** (Section 3.3) flood application scenario. However, the methodology can correctly extract and geoparse all road segments mentioned in tweets. The extracted road data primarily consists of major roads because these were mainly discussed in text messages. The low number of non-repeating texts in this application scenario is explained by the low number of roads in general and the low number of major roads within the impacted area of the Angeles National Forest. Except for the two roads from which information is extracted, mainly local and private roads are located within the impact zone. This situation is very

different from the situation in the **Oakland** application scenario (**X**) (Section 4.4), where the impact zone was located within an urban area.

In the **Bobcat** wildfire application scenario (**XI**) the impact zone is estimated using the methodology developed and described in [Module I](#). This differs from the **Oakland** (**X**) flood application scenario, where the impact zone is derived from a 100/500-year flood map provided by the Association of Bay Area Governments. Overlaying the estimated hazard impact zone ([Module I](#)) with the intact road network for the **Bobcat** wildfire study region reveals eleven road segments at risk to be impacted by the hazard. Additionally, two major roads are directly extracted as impacted by the hazard ([Module I](#)) using VGI information. Applying the developed methodology based on freely available data, like RS, VGI, and OSM data, to the **Bobcat** wildfire, it was possible to determine road segments directly or possibly impacted by the actual hazard. These identified road segments are subsequently removed from the intact road network based on OSM data to construct the actual road network impacted by the wildfire. To handle the large number of nodes and edges in this application scenario network, network preprocessing steps to reduce computational time are necessary.

Considering the network accessibility analysis, we concluded that the road network is not heavily impacted by the wildfire hazard for the **Bobcat** wildfire application scenario. Though significant roads that lead in the Angeles National Forest are impacted, these do not influence the overall network degradation as these are no connecting roads to other major roads. A segment of the Angeles Crest Highway is degraded, but this closure does not cause an overall degradation, as a bypass is available for this segment. The degradation only slightly impacts the total Angeles Crest Highway accessibility. Therefore, the road network accessibility overall changes only slightly compared to the intact and the degraded road network. The overall accessibility remains high due to the numerous connections between cities south and north of the Angeles National Forest that don't necessitate travel through the mountains. Additionally, accessibility within the respective city regions is unaffected.

Comparing the outcomes of accessibility measures applied to the **Bobcat** wildfire study with the **Oakland** (**X**) (Section 4.4) flood application scenario reveals significant differences. In the **Oakland** application scenario context, the developed measures show that the flood hazard heavily impacts the road network overall. Furthermore, the developed measures show divergent results. On the contrary, within the **Bobcat** application scenario, the measures agree mostly. Furthermore, they consistently identify a few edges as the most impacted ones. These results can be linked to the difference in network characteristics (e.g., urban vs regional, rural, crossing mountains) and the quantity and spatial distribution of degraded edges within each network for the two application scenarios. Due to the excellent alignment of the accessibility measures in the **Bobcat** application scenario, the impacted edges can be identified, and the impacts of the hazard on the road infrastructure

can be evaluated with high certainty. Therefore, the developed framework offers valuable insights into road accessibility for first responders in hazard scenario route planning.

5.4.2 Transferability of Framework

The application of the developed modules I and II of the framework for the assessment of road network accessibility to the **Bobcat (XI)** wildfire demonstrates that the transfer of all modules and components is feasible. To adapt the framework for the application to the **Bobcat** wildfire, only the data sources, namely RS, VGI, and OSM data need to be adapted. The developed methods of **Module I** and **Module II** can be transferred to other regions impacted by hazards without further modifications. Furthermore, the framework can be transferred to other hazard types by only updating the data sources and adapting the impact zone estimation approaches. For example, adaptations are necessary for the use of RS data for other types of natural hazards (Section 3.1.6). A variety of methods has been developed using RS data for hazard extent estimation for various hazards, e.g., [85, 55, 64] (Section 2.1.1). These could easily replace the conducted wildfire extent estimation method.

Furthermore, adaptations are necessary for the use of VGI data for other types of natural hazards, as well (Section 3.2.6). Two distinct methodologies for *stationary* and *moving* hazards have been already developed to account for the major difference, the degree of temporal development, between these hazard types. However, different hazard types are characterised by further differences, like propagation pattern, onset speed, and terrain-dependency. Therefore, the developed methodologies still require slight adaptations when being transferred (e.g., [21, 150]). E.g., flood hazard estimation from VGI ([132, 158, 174] Section 2.1.1) could be tackled with the developed *stationary* hazard approximation approach. The developed approach could then profit from the additional incorporation of water depth information [175] extracted from VGI for this hazard type. Additionally, floods might more likely occur in places with lower elevation. The inclusion of weighting factors based on terrain information using Digital Elevation Models [305] could be introduced for barycenter calculation.

Overall, these developed methods (**Module I**, Section 3.1, Section 3.2) constitute a robust foundation for slight adaptations to different hazard types. The methodologies concerning the extraction of directly impacted roads (**Module I**, Section 3.3) and the road network accessibility assessment (**Module II**) do not need adaptation for other hazard types. They can be applied instantly, after changes of data sources.

Additionally, the framework's modular structure and various possibilities for impact assessment (impact zone using RS and VGI data and direct road impact) also allows the flexibility to assemble framework components as needed. For example, external elements can be used. These could be impact zones from other data source, as it has been demonstrated

in the **Oakland (X)** flood application scenario. The impact zone was obtained from a 100/500-year flood hazard map for the San Francisco Bay Area provided by the Association of Bay Area Governments. In the **Oakland** study, the road network accessibility was assessed based on a degraded network using this type of impact zones to determine possibly impacted roads. Vice versa, the determined impact zones of **Module I** could be used as input information for other network analyses (e.g., railroad networks). Additionally, the developed methods for impact (zone) determination could also be used separately or combined with further impact information from other data sources depending on the availability of suitable data. These could be used for general hazard analysis, such as spatial information investigations about trapped people, those at risk of displacement, or cautionary considerations. This flexibility enables the use of the developed framework in a variety of hazard types and possible network analysis scenarios.

5.5 Conclusion

In this chapter, the objective was to demonstrate the applicability and transferability of the developed framework for the assessment of the natural hazard's impact on road infrastructure. It was demonstrated on a specific independent application scenario, which has not been used before for the development of the methodology. It presents the combination and application of both integral components of the complete framework, the **Module I**, the natural hazard impact determination (Chapter 3) and **Module II**, the assessment of road network accessibility (Chapter 4) for the **Bobcat (XI)** wildfire near Los Angeles in 2020.

The combination of RS and VGI data is valuable. It provides very detailed hazard impact zones and larger areas, where people might be affected by the hazards. Additionally, specific information about impacted roads can be gained. For the **Bobcat** wildfire hazard application scenario, it was possible to obtain hazard impact information using the developed methodology of **Module I** of the framework. Furthermore, it was possible to obtain an intact road network using OSM data and to construct a degraded road network using the developed methodology of **Module II** of the framework. Overlaying the impact zones and direct impact on roads results in an actual degraded network illustrating the situation of the road infrastructure during the wildfire in the region of the Angeles National Forest. All accessibility metrics are able to analyze the road network accessibility without the need for additional traffic data for this specific hazard in this application scenario.

In summary, the integration of both **Module I** and **Module II** facilitates a robust assessment of the wildfire's influence on road infrastructure. This assessment is made possible by leveraging diverse freely and openly available geoinformation data sources, including RS and VGI data. The modularity and transferability of the developed framework enable its use in a variety of hazard types and regions and possible network analysis scenarios.

Synopsis and Outlook

This chapter includes elements from

[1] J. Florath, J. Chanussot, and S. Keller. “Road Accessibility during Natural Hazards Based on Volunteered Geographic Information Data and Network Analysis”. In: *ISPRS International Journal of Geo-Information* 13.4 (2024), p. 107

marked with a [green line](#).

The main objective of this thesis was the development of a generic framework for the network accessibility analysis of natural hazards’ impacts on road infrastructure. The first research goal, addressed in [Module I](#) of this thesis, is the natural hazard impact determination using openly available multi-source geoinformation. The second research goal, addressed in [Module II](#) of this thesis, is the subsequent road network accessibility analysis based on the determined hazard impacts of [Module I](#).

The detailed discussions and conclusions for each of the subtopics can be found within their respective chapters (Chapter 3 and Chapter 4) of this thesis. The generic framework for the network accessibility analysis under natural hazards’ impacts on infrastructure results from a combination of both parts as discussed and concluded for an application scenario example in Chapter 5. This chapter gives a synoptical discussion and conclusion on the complete generic framework (Section 6.1). Finally, future improvements for the framework and adaptations for its application potential in disaster management are presented in Section 6.2.

6.1 Synoptical Discussion and Conclusion

Before giving general concluding remarks on the generic framework, which comprises the two independent [Modules I](#) and [II](#), conclusions are drawn for the two modules, separately.

The first module addresses the first research goal of this thesis, the natural hazard impact determination with multi-source geoinformation data. In this module the impact of natural hazards, its location and impact on roads, are determined. The module relies on various geoinformation data: RS and VGI. The assessment of the hazards’ impacts on

road networks requires an approach that distinguishes between two fundamental types of impact: affected areas in general and direct impacts on road infrastructure. Affected areas involve estimating hazard impact zones first. By overlaying these impact zones onto the surveyed area, we can identify regions susceptible to the hazard's impacts. Specifically, when overlapped with the road network, we can extract information about roads that are at risk of being impacted. Furthermore, direct impact extractions focus on the immediate consequences of a hazard's direct influence on road segments.

Overall, geoinformation data like RS and VGI are suitable for the determination of hazard impacts. In contrast to, e.g., other geoinformation data sources, RS and VGI offer distinct advantages. Especially, the combination of RS and VGI results in the enhancement of accuracies and a higher level of detail of hazard impact assessments. It also allows large-scale surveys (RS) and rapid updates (VGI) in response to changing conditions. Moreover, the easy accessibility and open availability of these data sources make them most cost-effective for hazard impact determination.

The second module addresses the second research goal of this thesis, the road network accessibility assessment during natural hazards. The second module focuses on road network analysis, which relies on publicly available OSM data. A degraded network is constructed by overlaying impacts determined in [Module I](#) with a road network. Examining the direct impacts gives a more transparent, immediate picture, but looking at the impact zones gives a broader view of possible impacts. In scenarios where complete data on direct impacts might not be immediately available, the significance of the estimated impact zone becomes evident. Different accessibility measures are calculated to assess the network's performance before, during, or shortly after the hazard. Notably, this study introduces a novel approach that considers anticipated congestion scenarios. All measures achieve the objective of analysing road network accessibility well, without using additional traffic data. They therefore tackle the challenge of restricted global data availability on hazard-induced road network impacts.

The complete generic framework for assessing network accessibility during natural hazard impacts combines both modules. The presented framework addresses the gap in the existing literature related to road network analysis in a natural hazard context. While some studies have considered degraded network scenarios, they often focus on single application scenarios in specific locations, e.g., [8, 10, 11]. This limits their applicability to other hazards and regions. Additionally, access to complex degraded road datasets after a natural hazard is challenging, hindering the transferability of proposed advanced models or simulations, e.g. [34]. The developed framework tackles the significant challenges for a holistic hazard-impacted road network analysis:

1. The framework is complete, from the hazard data acquisition to the road network accessibility analysis. The framework ensures that all necessary steps are integrated by covering the entire process chain, eliminating potential gaps.

2. It uses only freely available data and does not rely on restricted access data or data that might not be accessible during a natural hazard crisis. This is valid for both modules, using RS and VGI data to determine the impact of the natural hazard in [Module I](#) and OSM data as a road network basis in [Module II](#) (Section 2.1).
3. It is applicable in near-real time. One advantage of the used data is that it is primarily available in near-real time during or shortly after a natural hazard event (Section 2.1).
4. The framework profits from the use of multi-source geoinformation data like RS and VGI. Integrating these data sources offers several advantages: High-resolution RS provides comprehensive, objective data of large regions but very detailed. VGI offers localized, real-time insights and information about people's sentiment in affected areas. Furthermore, more specific information content about the hazard can be extracted from VGI texts (Section 2.1.1).
5. It is constructed to be able to consider different hazards that exhibit various hazard characteristics. The framework can be applied, e.g., to hazards of different temporal development speeds (wildfires vs TCs, Section 3.2) and hazards in diverse settings (floods vs wildfires, Chapter 4 and Chapter 5).
6. The framework is easily adaptable, independently of the scale and geographic location of the road network under investigation. It can be transferred across various hazards and network characteristics such as urban or rural, regional or local networks. Only slight adaptations, like data source changes, are necessary when transferring the developed methodologies (Section 5.4.2).
7. Due to the modular structure of the framework, it is very flexible and modules and methodologies can be applied independently from each other. For example, only [Module I](#) can be applied if hazard impact information is needed for other applications than network analysis. Or only [Module II](#) can be applied to conduct road network accessibility analysis based on external road impact information data.

In conclusion, this study successfully addresses the challenges of developing a generic, complete framework from determining a hazard's impact to network analysis independently of scale and characteristics of road network types. The proposed generic framework offers a valuable contribution to road network analysis in a natural hazard context. The exemplary applications in different hazard scenarios demonstrate the framework's versatility and effectiveness in assessing road network performance during hazardous events.

6.2 Outlook

The modules and their respective sub-topics developed in this thesis offer possibilities for future enhancements. In the following, these potential advances are presented for the [Module I](#) and [Module II](#), respectively.

Module I This module comprises various components for the natural hazard impact determination using multi-geoinformation data. Therefore, each sub-topic presents opportunities for advancing the methodology. The first developed methodology to estimate natural hazard impact zones employing RS data primarily focuses on the precise differentiation between burned and active fire area extents as hazard impact zones. For the extension of this methodology to address other natural hazards with RS data, adaptations are necessary. The adaptation to other hazards would need different data sources, such as SAR or InSAR data for flood mapping (e.g., [84, 15]), in contrast to optical data employed for fire mapping. The established supervised methodology can serve as a basis for the estimation of other hazards (e.g., [306]).

In the future, adaptations of the developed methodologies for natural hazard impact zone estimation using VGI data could be explored for various natural hazards. Tweet occurrence patterns exhibit variations across different hazard types and sociodemographic and geographical factors. Therefore, the distribution of tweet data points for other hazards or in other regions may be more favorable for the impact zone extraction methodology (e.g., [21]). Furthermore, instead of tweets, alternative VGI data sources, such as data from other social media platforms [307], could be explored. The integration of volunteered image analysis [177] could improve the assessment of hazard characteristics and contribute to augmenting the overall volume of available data.

Regarding direct road impact extraction from VGI data, further development of the method is possible. Instead of relying solely on tweets, other textual data sources, including rescue service notifications and alternative VGI data, could be employed. The utilization of such information can lead to even greater precision in terms of incident location identification. Moreover, NLP techniques for information retrieval enable the extraction of additional information, such as hazard severity, through text content classification [24].

Module II Potential improvements could be made in various aspects of the second module. OSM data are a valuable source for road networks; however, its utility can be impacted by the voluntary nature of contributions. These can lead to variations in data coverage and accuracy. OSM's global community of contributors continually improves the quality and coverage. Despite the improvements, OSM data may not consistently include comprehensive road information, such as travel speed or maximum number of lanes necessary for network analysis. To address these limitations, techniques (e.g., a fuzzy framework for the estimation of speeds along OSM road segments) outlined in prior work can be applied to enhance the routability of OSM data [12].

To further evaluate and enhance the developed framework's effectiveness, it would be advantageous to conduct comparisons with other, more detailed network analysis models (e.g., cascading failure models [271, 273] or models using travel demand data [270, 277]). Such comparisons can provide valuable insights into the developed framework's strengths and areas for improvement. Additionally, impact data derived from other geoinformation sources, e.g., of detailed traffic data [270, 277], could be included or used for comparison. These data would require the condition of openly and timely availability. The current framework employs a simplified model for evacuation scenarios using only two shelter locations. However, real-world evacuations are more complex and involve factors like destination choice and road blockages [302]. These inclusions could provide more precise assessments of network accessibility especially during congestion.

General Framework In the future, with further developments, the framework could be integrated in a practical application in disaster assessment. The framework's ability to provide a rapid overview of natural hazard impacts on road networks is valuable as an initial step in disaster risk management planning. The integration with natural hazard management strategies of local authorities and relevant stakeholders could be pursued. Practical implementation issues like legal issues for the use of VGI data or multilingualism would need to be considered for a tool for natural hazard management. So far, the framework focuses on the determination of current hazard impacts. Meteorological data, like precipitation and wind speed data (e.g., [188, 189]), could be integrated in the future to include the predictions of areas at risk. Prospective possible hazard extents could be included to directly account for possible hazard developments in hazard management.

Bibliography

- [1] J. Florath, J. Chanussot, and S. Keller. “Road Accessibility during Natural Hazards Based on Volunteered Geographic Information Data and Network Analysis”. In: *ISPRS International Journal of Geo-Information* 13.4 (2024), p. 107.
- [2] P. J. Ward et al. “Natural hazard risk assessments at the global scale”. In: *Natural Hazards and Earth System Sciences* 20.4 (2020), pp. 1069–1096.
- [3] V. Thomas and R. López. “Global increase in climate-related disasters”. In: *Asian Development Bank Economics Working Paper Series* No. 466 (2015).
- [4] Centre for Research on the Epidemiology of Disasters (CRED), part of the University of Louvain (UCLouvain). *Emergency Events Database (EM-DAT)*. 2023. URL: <https://public.emdat.be/data> (visited on 06/12/2023).
- [5] K. Songwathana. “The relationship between natural disaster and economic development: a panel data analysis”. In: *Procedia Engineering* 212 (2018), pp. 1068–1074.
- [6] B. Wisner et al. *At risk: natural hazards, people’s vulnerability and disasters*. Routledge, 2014.
- [7] A. T. Murray and T. Grubestic. *Critical infrastructure: Reliability and vulnerability*. Springer Science & Business Media, 2007.
- [8] G. Hilly et al. “Methodological framework for analysing cascading effects from flood events: The case of Sukhumvit Area, Bangkok, Thailand”. In: *Water* 10.1 (2018), p. 81.
- [9] R. Espada, A. Apan, and K. McDougall. “Vulnerability assessment of urban community and critical infrastructures for integrated flood risk management and climate adaptation strategies”. In: *International Journal of Disaster Resilience in the Built Environment* 8.4 (2017), pp. 375–411.
- [10] I. S. Negi et al. “Cost assessment of losses due to recent reactivation of Kaliasaur landslide on National Highway 58 in Garhwal Himalaya”. In: *Natural Hazards* 68 (2013), pp. 901–914.
- [11] J. Azevedo et al. “Seismic vulnerability of lifelines in the greater Lisbon area”. In: *Bulletin of Earthquake Engineering* 8 (2010), pp. 157–180.
- [12] J. Guth. “Enhancing OpenStreetMap for the Assessment of Critical Road Infrastructure in a Disaster Context”. PhD thesis. Karlsruhe Institute of Technology, 2021.
- [13] E. Dalziell and A. Nicholson. “Risk and impact of natural hazards on a road network”. In: *Journal of Transportation Engineering* 127.2 (2001), pp. 159–166.
- [14] J. Florath and S. Keller. “Supervised Machine Learning Approaches on Multispectral Remote Sensing Data for a Combined Detection of Fire and Burned Area”. In: *Remote Sensing* 14.3 (2022), p. 657.
- [15] A. H. Tanim et al. “Flood detection in urban areas using satellite imagery and machine learning”. In: *Water* 14.7 (2022), p. 1140.

- [16] C. Wang, Z. Li, and X. Huang. “Geospatial assessment of wetness dynamics in the October 2015 SC flood with remote sensing and social media”. In: *Southeastern Geographer* 58.2 (2018), pp. 164–180.
- [17] E. García-Meléndez. “Multisensor data integration and GIS analysis for Natural Hazard mapping in a semiarid area (southeast Spain)”. In: *Advances in Space Research* 21 (1998), pp. 493–499.
- [18] D. Ehrlich et al. “Extracting building stock information from optical satellite imagery for mapping earthquake exposure and its vulnerability”. In: *Natural Hazards* 68 (2013), pp. 79–95.
- [19] W. Jiao. “Multi-sensor remote sensing for drought characterization: current status, opportunities and a roadmap for the future”. In: *Remote Sensing of Environment* 256 (2021), p. 112313.
- [20] A. Dittrich and C. Lucas. “Is this Twitter event a disaster?” In: *AGILE’2014 International Conference on Geographic Information Science, Connecting a Digital Europe through Location and Place*. AGILE Digital Editions, 2014.
- [21] Y. Wang et al. “Using social media for emergency response and urban sustainability: A case study of the 2012 Beijing rainstorm”. In: *Sustainability* 8.1 (2016), p. 25.
- [22] Z. Wang, X. Ye, and M.-H. Tsou. “Spatial, temporal, and content analysis of Twitter for wildfire hazards”. In: *Natural Hazards* 83.1 (2016), pp. 523–540.
- [23] A. Dittrich. “Real-time event analysis and spatial information extraction from text using social media data”. PhD thesis. Karlsruhe Institute of Technology, 2016.
- [24] M. Imran, P. Mitra, and C. Castillo. “Twitter as a lifeline: Human-annotated twitter corpora for NLP of crisis-related messages”. In: *arXiv preprint arXiv:1605.05894* (2016).
- [25] L. Yu and D. Li. “Road-Related Information Mining from Social Media Data: A Joint Relation Extraction and Entity Recognition Approach”. In: *Buildings* 13.1 (2022), p. 104.
- [26] B. Jongman et al. “Early flood detection for rapid humanitarian response: harnessing near real-time satellite and Twitter signals”. In: *ISPRS International Journal of Geo-Information* 4.4 (2015), pp. 2246–2266.
- [27] A. Yute et al. “Supplementing Satellite Imagery With Social Media Data For Remote Reconnaissance: A Case Study Of The 2020 Taal Volcano Eruption”. In: *The International Archives of the Photogrammetry, Remote Sensing and Spatial Information Sciences* 46 (2021), pp. 329–335.
- [28] R. Sadiq et al. “Integrating remote sensing and social sensing for flood mapping”. In: *Remote Sensing Applications: Society and Environment* 25 (2022), p. 100697.
- [29] J. Mast et al. “Linking remote sensing data and online engagement in flood events in Nigeria”. In: *2023 Joint Urban Remote Sensing Event (JURSE)*. IEEE, 2023, pp. 1–4.
- [30] S. Andreadis et al. “Earthquakes: From Twitter detection to EO data processing”. In: *IEEE Geoscience and Remote Sensing Letters* 19 (2022), pp. 1–5.
- [31] S. Marshall. “Line structure representation for road network analysis”. In: *Journal of Transport and Land Use* 9.1 (2016), pp. 29–64.
- [32] K. S. Oberoi et al. “Spatial modeling of urban road traffic using graph theory”. In: *Proceedings of Spatial Analysis and GEOmatics (SAGEO) 2017*. 2017, pp. 264–277.

- [33] T. Sarkar, D. Sarkar, and P. Mondal. "Road network accessibility analysis using graph theory and GIS technology: a study of the villages of English Bazar Block, India". In: *Spatial Information Research* 29.3 (2021), pp. 405–415.
- [34] Y. Wen et al. "Incorporating transportation network modeling tools within transportation economic impact studies of disasters". In: *Journal of Traffic and Transportation Engineering* 1.4 (2014), pp. 247–260.
- [35] V. L. Knoop et al. "Link-level vulnerability indicators for real-world networks". In: *Transportation Research Part A: Policy and Practice* 46.5 (2012), pp. 843–854.
- [36] G. Galiano and L. Moretti. "Consistency of urban roads to manage emergencies: Methodology to identify the minimum network with total connectivity at maximum availability". In: *Sustainability* 13.20 (2021), p. 11151.
- [37] J. K. Shrestha, P. Pudasaini, and L. Mussone. "Rural road network performance and pre-disaster planning: an assessment methodology considering redundancy". In: *Transportation Planning and Technology* 44.7 (2021), pp. 726–743.
- [38] J. M. Diaz. "Economic impacts of wildfire". In: *Southern Fire Exchange* 498 (2012), pp. 2012–7.
- [39] H. Demirel, M. Kompil, and F. Nemry. "A framework to analyze the vulnerability of European road networks due to Sea-Level Rise (SLR) and sea storm surges". In: *Transportation Research Part A: Policy and Practice* 81 (2015), pp. 62–76.
- [40] F. Bono and E. Gutiérrez. "A network-based analysis of the impact of structural damage on urban accessibility following a disaster: the case of the seismically damaged Port Au Prince and Carrefour urban road networks". In: *Journal of Transport Geography* 19.6 (2011), pp. 1443–1455.
- [41] E. D. Vugrin, D. E. Warren, and M. A. Ehlen. "A resilience assessment framework for infrastructure and economic systems: Quantitative and qualitative resilience analysis of petrochemical supply chains to a hurricane". In: *Process Safety Progress* 30.3 (2011), pp. 280–290.
- [42] M. R. Ahmed et al. "Processing of near real time land surface temperature and its application in forecasting forest fire danger conditions". In: *Sensors* 20.4 (2020), p. 984.
- [43] J. Florath, J. Chanussot, and S. Keller. "Utilizing Volunteered Geographic Information for Real-Time Analysis of Fire Hazards: Investigating the Potential of Twitter Data in Assessing the Impacted Areas". In: *Fire* 7.1 (2023), p. 6.
- [44] J. Florath, J. Chanussot, and S. Keller. "Rapid natural hazard extent estimation from twitter data: investigation for hurricane impact areas". In: *Natural Hazards* (2024), pp. 1–22.
- [45] A. Teodoro and L. Duarte. "The role of satellite remote sensing in natural disaster management". In: *Nanotechnology-Based Smart Remote Sensing Networks for Disaster Prevention*. Elsevier, 2022, pp. 189–216.
- [46] R. Le Bivic et al. "Potential and limitation of SPOT-5 ortho-image correlation to investigate the cinematics of landslides: The example of "Mare à Poule d'Eau"(Réunion, France)". In: *Remote Sensing* 9.2 (2017), p. 106.
- [47] D. Golovko et al. "Evaluation of remote-sensing-based landslide inventories for hazard assessment in Southern Kyrgyzstan". In: *Remote Sensing* 9.9 (2017), p. 943.

- [48] L. Nava et al. “Rapid mapping of landslides on SAR data by attention U-Net”. In: *Remote Sensing* 14.6 (2022), p. 1449.
- [49] G. Esposito et al. “A spaceborne SAR-based procedure to support the detection of landslides”. In: *Natural Hazards and Earth System Sciences* 20.9 (2020), pp. 2379–2395.
- [50] V. Singhroy and K. Molch. “Characterizing and monitoring rockslides from SAR techniques”. In: *Advances in Space Research* 33.3 (2004), pp. 290–295.
- [51] J. Wang et al. “Monitoring of large-scale landslides in Zongling, Guizhou, China, with improved distributed scatterer interferometric SAR time series methods”. In: *Landslides* 17 (2020), pp. 1777–1795.
- [52] K. Dai et al. “Interpretation and sensitivity analysis of the InSAR line of sight displacements in landslide measurements”. In: *GIScience & Remote Sensing* 59.1 (2022), pp. 1226–1242.
- [53] H. Rott and T. Nagler. “The contribution of radar interferometry to the assessment of landslide hazards”. In: *Advances in Space Research* 37.4 (2006), pp. 710–719.
- [54] B. Riedel and A. Walther. “InSAR processing for the recognition of landslides”. In: *Advances in Geosciences* 14 (2008), pp. 189–194.
- [55] R. D. Gold et al. “Surface rupture and distributed deformation revealed by optical satellite imagery: The intraplate 2016 Mw 6.0 Petermann Ranges earthquake, Australia”. In: *Geophysical Research Letters* 46.17-18 (2019), pp. 10394–10403.
- [56] M. Chang et al. “Identification and deformation analysis of potential landslides after the Jiuzhaigou earthquake by SBAS-InSAR”. In: *Environmental Science and Pollution Research* 30.13 (2023), pp. 39093–39106.
- [57] J. Cherian. “Determining the amount of earthquake displacement using differential synthetic aperture radar interferometry (D-InSAR) and satellite images of Sentinel-1 A: A case study of Sarpol-e Zahab city”. In: *Advances in Engineering and Intelligence Systems* 1.01 (2022).
- [58] F. Bovenga et al. “Performance analysis of satellite missions for multi-temporal SAR interferometry”. In: *Sensors* 18.5 (2018), p. 1359.
- [59] F. Jing, L. Zhang, and R. P. Singh. “Pronounced Changes in Thermal Signals Associated with the Madoi (China) M 7.3 Earthquake from Passive Microwave and Infrared Satellite Data”. In: *Remote Sensing* 14.11 (2022), p. 2539.
- [60] N. Ahmad et al. “Investigation of spatio-temporal satellite thermal IR anomalies associated with the Awaran earthquake (Sep 24, 2013; M 7.7), Pakistan”. In: *Pure and Applied Geophysics* 176.8 (2019), pp. 3533–3544.
- [61] M. Bouih et al. “Deep mass redistribution prior to the 2010 Mw 8.8 Maule (Chile) Earthquake revealed by GRACE satellite gravity”. In: *Earth and Planetary Science Letters* 584 (2022), p. 117465.
- [62] B. Chao and J. Liau. “Gravity changes due to large earthquakes detected in GRACE satellite data via empirical orthogonal function analysis”. In: *Journal of Geophysical Research: Solid Earth* 124.3 (2019), pp. 3024–3035.
- [63] H.-P. Chan, K. I. Konstantinou, and M. Blackett. “Spatio-temporal surface temperature variations detected by satellite thermal infrared images at Merapi volcano, Indonesia”. In: *Journal of Volcanology and Geothermal Research* 420 (2021), p. 107405.

- [64] D. Coppola et al. “Thermal remote sensing for global volcano monitoring: experiences from the MIROVA system”. In: *Frontiers in Earth Science* 7 (2020), p. 362.
- [65] B. McCormick Kilbride et al. “Temporal variability in gas emissions at Bagana volcano revealed by aerial, ground, and satellite observations”. In: *Geochemistry, Geophysics, Geosystems* 24.6 (2023), e2022GC010786.
- [66] T. Lopez et al. “Evaluation of Redoubt Volcano’s sulfur dioxide emissions by the Ozone Monitoring Instrument”. In: *Journal of Volcanology and Geothermal Research* 259 (2013), pp. 290–307.
- [67] B. McCormick Kilbride et al. “Multi-year satellite observations of sulfur dioxide gas emissions and lava extrusion at Bagana volcano, Papua New Guinea”. In: *Frontiers in Earth Science* 7 (2019), p. 9.
- [68] M. P. Poland. “Synthetic aperture radar volcanic flow maps (SAR VFMs): A simple method for rapid identification and mapping of volcanic mass flows”. In: *Bulletin of Volcanology* 84.3 (2022), p. 32.
- [69] F. Di Traglia et al. “Joint exploitation of space-borne and ground-based multitemporal InSAR measurements for volcano monitoring: The Stromboli volcano case study”. In: *Remote Sensing of Environment* 260 (2021), p. 112441.
- [70] M. J. Bemelmans et al. “High-resolution InSAR reveals localised pre-eruptive deformation inside the crater of Agung volcano, Indonesia.” In: *Journal of Geophysical Research: Solid Earth* 128.5 (2023), e2022JB025669.
- [71] B. G. Dewanto et al. “Study of geothermal and volcanic activity at Mount Awu, the deadliest active volcano in North Sulawesi Province, Indonesia using Optical Satellite Imagery”. In: *Journal of Volcanology and Geothermal Research* 438 (2023), p. 107811.
- [72] E. Amato et al. “Mapping lava flows at Etna Volcano using Google Earth Engine, open-access satellite data, and machine learning”. In: *2021 International Conference on Electrical, Computer, Communications and Mechatronics Engineering (ICECCME)*. IEEE, 2021, pp. 1–6.
- [73] C. Corradino et al. “Classifying major explosions and paroxysms at Stromboli volcano (Italy) from space”. In: *Remote Sensing* 13.20 (2021), p. 4080.
- [74] A. V. Shevchenko et al. “Constructive and destructive processes during the 2018–2019 eruption episode at Shiveluch volcano, Kamchatka, studied from satellite and aerial data”. In: *Frontiers in Earth Science* 9 (2021), p. 680051.
- [75] S. Kloos et al. “Agricultural drought detection with MODIS based vegetation health indices in southeast Germany”. In: *Remote Sensing* 13.19 (2021), p. 3907.
- [76] A. C. Das, R. Noguchi, and T. Ahamed. “An assessment of drought stress in tea estates using optical and thermal remote sensing”. In: *Remote Sensing* 13.14 (2021), p. 2730.
- [77] M. Shorachi, V. Kumar, and S. C. Steele-Dunne. “Sentinel-1 SAR backscatter response to agricultural drought in the Netherlands”. In: *Remote Sensing* 14.10 (2022), p. 2435.
- [78] M. Anderson and W. Kustas. “Thermal remote sensing of drought and evapotranspiration”. In: *Eos, Transactions American Geophysical Union* 89.26 (2008), pp. 233–234.
- [79] H. West, N. Quinn, and M. Horswell. “Remote sensing for drought monitoring & impact assessment: Progress, past challenges and future opportunities”. In: *Remote Sensing of Environment* 232 (2019), p. 111291.

- [80] M. Urban et al. “Surface moisture and vegetation cover analysis for drought monitoring in the southern Kruger National Park using Sentinel-1, Sentinel-2, and Landsat-8”. In: *Remote Sensing* 10.9 (2018), p. 1482.
- [81] Q. Qin et al. “Optical and thermal remote sensing for monitoring agricultural drought”. In: *Remote Sensing* 13.24 (2021), p. 5092.
- [82] S. K. Jain et al. “Delineation of flood-prone areas using remote sensing techniques”. In: *Water Resources Management* 19 (2005), pp. 333–347.
- [83] L. Feng et al. “Assessment of inundation changes of Poyang Lake using MODIS observations between 2000 and 2010”. In: *Remote Sensing of Environment* 121 (2012), pp. 80–92.
- [84] M. Haghghi. “Large-scale mapping of flood using Sentinel-1 radar remote sensing”. In: *The International Archives of the Photogrammetry, Remote Sensing and Spatial Information Sciences* 43 (2022), pp. 1097–1102.
- [85] S. T. Seydi. “Fusion of the Multisource Datasets for Flood Extent Mapping Based on Ensemble Convolutional Neural Network (CNN) Model”. In: *Journal of Sensors* 2022 (2022), pp. 1–20.
- [86] A. Tarpanelli, A. C. Mondini, and S. Camici. “Effectiveness of Sentinel-1 and Sentinel-2 for flood detection assessment in Europe”. In: *Natural Hazards and Earth System Sciences* 22.8 (2022), pp. 2473–2489.
- [87] S. J. Sippel et al. “Determination of inundation area in the Amazon River floodplain using the SMMR 37 GHz polarization difference”. In: *Remote Sensing of Environment* 48.1 (1994), pp. 70–76.
- [88] M. D. Goldberg et al. “Mapping, monitoring, and prediction of floods due to ice jam and snowmelt with operational weather satellites”. In: *Remote Sensing* 12.11 (2020), p. 1865.
- [89] B. Zhang et al. “Estimating tropical cyclone wind structure and intensity from spaceborne radiometer and synthetic aperture radar”. In: *IEEE Journal of Selected Topics in Applied Earth Observations and Remote Sensing* 14 (2021), pp. 4043–4050.
- [90] G. Zhang et al. “Tropical cyclone winds and inflow angle asymmetry from SAR imagery”. In: *Geophysical Research Letters* 48.20 (2021), e2021GL095699.
- [91] S. Shakya, S. Kumar, and M. Goswami. “Deep learning algorithm for satellite imaging based cyclone detection”. In: *IEEE Journal of Selected Topics in Applied Earth Observations and Remote Sensing* 13 (2020), pp. 827–839.
- [92] W. Bai et al. “Applications of GNSS-RO to numerical weather prediction and tropical cyclone forecast”. In: *Atmosphere* 11.11 (2020), p. 1204.
- [93] J. Eyre et al. “Assimilation of satellite data in numerical weather prediction. Part II: Recent years”. In: *Quarterly Journal of the Royal Meteorological Society* 148.743 (2022), pp. 521–556.
- [94] P. Chan et al. “Ground-Space-Sky Observing System Experiment during Tropical Cyclone Mulan in August 2022”. In: *Advances in Atmospheric Sciences* 40 (2023), pp. 194–200.
- [95] Y. Li and M. Momen. “Detection of weather events in optical satellite data using deep convolutional neural networks”. In: *Remote Sensing Letters* 12.12 (2021), pp. 1227–1237.

- [96] F. Wang and Y. J. Xu. “Comparison of remote sensing change detection techniques for assessing hurricane damage to forests”. In: *Environmental Monitoring and Assessment* 162 (2010), pp. 311–326.
- [97] A. K. Bhowmik and P. Cabral. “Cyclone Sidr impacts on the Sundarbans floristic diversity”. In: *Earth Science Research* 2.2 (2013), p. 62.
- [98] P. Mondal et al. “Radar and optical remote sensing for near real-time assessments of cyclone impacts on coastal ecosystems”. In: *Remote Sensing in Ecology and Conservation* 8.4 (2022), pp. 506–520.
- [99] L. Giglio et al. “Active fire detection and characterization with the advanced spaceborne thermal emission and reflection radiometer (ASTER)”. In: *Remote Sensing of Environment* 112.6 (2008), pp. 3055–3063.
- [100] W. Schroeder et al. “The New VIIRS 375 m active fire detection data product: Algorithm description and initial assessment”. In: *Remote Sensing of Environment* 143 (2014), pp. 85–96.
- [101] M. Matson, G. Stephens, and J. Robinson. “Fire detection using data from the NOAA-N satellites”. In: *International Journal of Remote Sensing* 8.7 (1987), pp. 961–970.
- [102] A. Calle, J. Casanova, and A. Romo. “Fire detection and monitoring using MSG Spinning Enhanced Visible and Infrared Imager (SEVIRI) data”. In: *Journal of Geophysical Research: Biogeosciences* 111.4 (2006).
- [103] V. Di Biase and G. Laneve. “Geostationary sensor based forest fire detection and monitoring: An improved version of the SFIDE algorithm”. In: *Remote Sensing* 10.5 (2018), p. 741.
- [104] S. S. Kumar and D. P. Roy. “Global operational land imager Landsat-8 reflectance-based active fire detection algorithm”. In: *International Journal of Digital Earth* 11.2 (2018), pp. 154–178.
- [105] W. Schroeder et al. “Active fire detection using Landsat-8/OLI data”. In: *Remote Sensing of Environment* 185 (2016), pp. 210–220.
- [106] J. Engelbrecht et al. “A simple normalized difference approach to burnt area mapping using multi-polarisation C-Band SAR”. In: *Remote Sensing* 9.8 (2017), p. 764.
- [107] R. Libonati et al. “An algorithm for burned area detection in the Brazilian Cerrado using 4 μm MODIS imagery”. In: *Remote Sensing* 7.11 (2015), pp. 15782–15803.
- [108] A.-C. Grivei, C. Văduva, and M. Datcu. “Assessment of Burned Area Mapping Methods for Smoke Covered Sentinel-2 Data”. In: *2020 13th International Conference on Communications (COMM)*. IEEE, 2020, pp. 189–192.
- [109] L. Knopp et al. “A Deep Learning Approach for Burned Area Segmentation with Sentinel-2 Data”. In: *Remote Sensing* 12.15 (2020), p. 2422.
- [110] M. C. Henry, J. K. Maingi, and J. McCarty. “Fire on the Water Towers: Mapping Burn Scars on Mount Kenya Using Satellite Data to Reconstruct Recent Fire History”. In: *Remote Sensing* 11.2 (2019), p. 104.
- [111] A. C. Axel. “Burned area mapping of an escaped fire into tropical dry forest in Western Madagascar using multi-season Landsat OLI Data”. In: *Remote Sensing* 10.3 (2018), p. 371.

- [112] R. Çömert, D. K. Matci, and U. Avdan. “Object Based Burned Area Mapping with Random Forest Algorithm”. In: *International Journal of Engineering and Geosciences* 4.2 (2019), pp. 78–87.
- [113] A. Barducci et al. “Infrared detection of active fires and burnt areas: theory and observations”. In: *Infrared Physics & Technology* 43.3-5 (2002), pp. 119–125.
- [114] L. Cicala et al. “Landsat-8 and Sentinel-2 for fire monitoring at a local scale: A case study on Vesuvius”. In: *2018 IEEE International Conference on Environmental Engineering (EE)*. IEEE. 2018, pp. 1–6.
- [115] L. Giglio et al. “An enhanced contextual fire detection algorithm for MODIS”. In: *Remote Sensing of Environment* 87.2-3 (2003), pp. 273–282.
- [116] L. Giglio, W. Schroeder, and C. O. Justice. “The collection 6 MODIS active fire detection algorithm and fire products”. In: *Remote Sensing of Environment* 178 (2016), pp. 31–41.
- [117] W. Schroeder et al. “Validation of GOES and MODIS active fire detection products using ASTER and ETM+ data”. In: *Remote Sensing of Environment* 112.5 (2008), pp. 2711–2726.
- [118] G. Mallinis and N. Koutsias. “Comparing ten classification methods for burned area mapping in a Mediterranean environment using Landsat TM satellite data”. In: *International Journal of Remote Sensing* 33.14 (2012), pp. 4408–4433.
- [119] M. Kurum. “C-band SAR backscatter evaluation of 2008 Gallipoli forest fire”. In: *IEEE Geoscience and Remote Sensing Letters* 12.5 (2015), pp. 1091–1095.
- [120] Y. Ban et al. “Near real-time wildfire progression monitoring with Sentinel-1 SAR time series and deep learning”. In: *Scientific reports* 10.1 (2020), pp. 1–15.
- [121] J. Wei et al. “The Automatic Detection of Fire Scar in Alaska using Multi-Temporal PALSAR Polarimetric SAR Data”. In: *Canadian Journal of Remote Sensing* 44.5 (2018), pp. 447–461.
- [122] F. Ofli et al. “A real-time system for detecting landslide reports on social media using artificial intelligence”. In: *International Conference on Web Engineering*. Springer. 2022, pp. 49–65.
- [123] C. Bono et al. “TriggerCit: Early Flood Alerting using Twitter and Geolocation—a comparison with alternative sources”. In: *arXiv preprint arXiv:2202.12014* (2022).
- [124] S. Sabri et al. “Leveraging VGI integrated with 3D spatial technology to support urban intensification in Melbourne, Australia”. In: *Urban Planning* 1.2 (2016), pp. 32–48.
- [125] B. Dienstl and J. Scholz. “A concept for smart transportation user-feedback utilizing volunteered geoinformation approaches”. In: *Data Analytics: Paving the Way to Sustainable Urban Mobility: Proceedings of 4th Conference on Sustainable Urban Mobility (CSUM2018)*. Springer. 2019, pp. 538–545.
- [126] M. Adnan, P. A. Longley, and S. M. Khan. “Social dynamics of twitter usage in London, Paris, and New York City”. In: *First Monday* (2014).
- [127] C. Castillo, M. Mendoza, and B. Poblete. “Information credibility on Twitter”. In: *Proceedings of the 20th International Conference on World Wide Web*. 2011, pp. 675–684.
- [128] F. Benevenuto et al. “Detecting spammers and content promoters in online video social networks”. In: *Proceedings of the 32nd international ACM SIGIR conference on Research and development in information retrieval*. 2009, pp. 620–627.

- [129] J. Ratkiewicz et al. "Truthy: mapping the spread of astroturf in microblog streams". In: *Proceedings of the 20th international conference companion on World wide web*. 2011, pp. 249–252.
- [130] L. Sloan. "Who tweets in the United Kingdom? Profiling the Twitter population using the British social attitudes survey 2015". In: *Social Media+ Society* 3.1 (2017), p. 2056305117698981.
- [131] X. Guan and C. Chen. "Using social media data to understand and assess disasters". In: *Natural Hazards* 74.2 (2014), pp. 837–850.
- [132] P. Ponukumati and S. K. Regonda. "Twitter-a new citizen science solution for urban flood database# urban floods# flood database". In: *ResearchSquare preprint* (2023).
- [133] D. Jurgens et al. "Geolocation prediction in twitter using social networks: A critical analysis and review of current practice". In: *Proceedings of the International AAAI Conference on Web and Social Media*. Vol. 9. 1. 2015, pp. 188–197.
- [134] C. A. Davis et al. "Inferring the location of twitter messages based on user relationships". In: *Transactions in GIS* 15.6 (2011), pp. 735–751.
- [135] A. M. MacEachren et al. "Geo-twitter analytics: Applications in crisis management". In: *25th International Cartographic Conference*. 2011, pp. 3–8.
- [136] F. Laylavi, A. Rajabifard, and M. Kalantari. "A multi-element approach to location inference of twitter: A case for emergency response". In: *ISPRS International Journal of Geo-Information* 5.5 (2016), p. 56.
- [137] C.-Y. Huang et al. "Location Prediction for Tweets". In: *Frontiers in Big Data* 2 (2019), p. 5.
- [138] J. Gelernter and S. Balaji. "An algorithm for local geoparsing of microtext". In: *GeoInformatica* 17 (2013), pp. 635–667.
- [139] S. H. Burton et al. "'Right time, right place' health communication on Twitter: value and accuracy of location information". In: *Journal of Medical Internet Research* 14.6 (2012), e2121.
- [140] B. Huang and K. M. Carley. "A large-scale empirical study of geotagging behavior on twitter". In: *Proceedings of the 2019 IEEE/ACM International Conference on Advances in Social Networks Analysis and Mining*. 2019, pp. 365–373.
- [141] O. Ajao, J. Hong, and W. Liu. "A survey of location inference techniques on Twitter". In: *Journal of Information Science* 41.6 (2015), pp. 855–864.
- [142] M. G. Kim and J. H. Koh. "Recent research trends for geospatial information explored by Twitter data". In: *Spatial Information Research* 24.2 (2016), pp. 65–73.
- [143] G. Fuchs et al. "Tracing the German centennial flood in the stream of tweets: first lessons learned". In: *Proceedings of the second ACM SIGSPATIAL international workshop on crowd-sourced and volunteered geographic information*. 2013, pp. 31–38.
- [144] J. Kersten et al. "Robust filtering of crisis-related tweets". In: *ISCRAM 2019 conference proceedings-16th international conference on information systems for crisis response and management*. 2019.
- [145] F. Ofli et al. "Landslide detection in real-time social media image streams". In: *Neural Computing and Applications* (2023), pp. 1–11.

- [146] T. Sakaki, M. Okazaki, and Y. Matsuo. “Earthquake shakes twitter users: real-time event detection by social sensors”. In: *Proceedings of the 19th International Conference on World Wide Web*. 2010, pp. 851–860.
- [147] E. I. George and C. M. Abraham. “Real-time earthquake detection using Twitter tweets”. In: *AIP Conference Proceedings*. Vol. 2520. 1. AIP Publishing. 2022, pp. 030014–1.
- [148] D. Prabhakar Kaila et al. “An empirical text mining analysis of Fort McMurray wildfire disaster twitter communication using topic model”. In: *Disaster Advances* 9.7 (2016), pp. 1–5.
- [149] X. Shi et al. “Detecting events from the social media through exemplar-enhanced supervised learning”. In: *International Journal of Digital Earth* 12.9 (2019), pp. 1083–1097.
- [150] A. Kumar et al. “A deep multi-modal neural network for informative Twitter content classification during emergencies”. In: *Annals of Operations Research* (2020), pp. 1–32.
- [151] K. Aziz, D. Zaidouni, and M. Bellafkih. “Social Network Analytics: Natural Disaster Analysis Through Twitter”. In: *2019 Third International Conference on Intelligent Computing in Data Sciences (ICDS)*. IEEE. 2019, pp. 1–7.
- [152] A. Kruspe, J. Kersten, and F. Klan. “Detecting event-related tweets by example using few-shot models”. In: *ISCRAM 2019 conference proceedings-16th International Conference on Information Systems for Crisis Response and Management*. 2019, pp. 825–835.
- [153] A. T. Hadgu, S. Abualhaija, and C. Niederée. “Real-time Adaptive Crawler for Tracking Unfolding Events on Twitter”. In: *ISCRAM 2019 conference proceedings-16th International Conference on Information Systems for Crisis Response and Management*. 2019, pp. 923–932.
- [154] C. Loynes, J. Ouenniche, and J. De Smedt. “The detection and location estimation of disasters using Twitter and the identification of Non-Governmental Organisations using crowdsourcing”. In: *Annals of Operations Research* 308 (2022), pp. 339–371.
- [155] A. Kumar, M. Jiang, and Y. Fang. “Where not to go? Detecting road hazards using Twitter”. In: *Proceedings of the 37th international ACM SIGIR conference on Research & Development in Information Retrieval*. 2014, pp. 1223–1226.
- [156] J. Fohringer et al. “Social media as an information source for rapid flood inundation mapping”. In: *Natural Hazards and Earth System Sciences* 15.12 (2015), pp. 2725–2738.
- [157] Y.-T. Lin et al. “Quantifying flood water levels using image-based volunteered geographic information”. In: *Remote Sensing* 12.4 (2020), p. 706.
- [158] J. P. De Albuquerque et al. “A geographic approach for combining social media and authoritative data towards identifying useful information for disaster management”. In: *International Journal of Geographical Information Science* 29.4 (2015), pp. 667–689.
- [159] V. Lorini et al. “Integrating social media into a pan-european flood awareness system: A multilingual approach”. In: *arXiv preprint arXiv:1904.10876* (2019).
- [160] S. Dashti et al. “Supporting disaster reconnaissance with social media data: A design-oriented case study of the 2013 Colorado floods”. In: *ISCRAM 2014 conference proceedings-11th International Conference on Information Systems for Crisis Response and Management*. 2014, pp. 632–641.

- [161] A. T. Chatfield and U. Brajawidagda. "Twitter early tsunami warning system: A case study in Indonesia's natural disaster management". In: *2013 46th Hawaii international conference on system sciences*. IEEE. 2013, pp. 2050–2060.
- [162] Y. Shibuya and H. Tanaka. "Detecting Disaster Recovery Activities via Social Media Communication Topics". In: *ISCRAM 2019 conference proceedings-16th International Conference on Information Systems for Crisis Response and Management*. 2019, pp. 706–718.
- [163] S. Arapostathis. "Social Network Users Create Seismic Intensity Maps: An Automatic Approach of the Methodology". In: *SN Computer Science* 2.5 (2021), pp. 1–11.
- [164] N. Pourebrahim et al. "Understanding communication dynamics on Twitter during natural disasters: A case study of Hurricane Sandy". In: *International Journal of Disaster Risk Reduction* 37 (2019), p. 101176.
- [165] M. Karimiziarani and H. Moradkhani. "Social response and Disaster management: Insights from twitter data Assimilation on Hurricane Ian". In: *International Journal of Disaster Risk Reduction* (2023), p. 103865.
- [166] D. Crawl et al. "Firemap: A dynamic data-driven predictive wildfire modeling and visualization environment". In: *Procedia Computer Science* 108 (2017), pp. 2230–2239.
- [167] H. Waqas and M. Imran. "# CampFireMissing: An Analysis of Tweets About Missing and Found People From California Wildfires". In: *ISCRAM 2019 conference proceedings-16th International Conference on Information Systems for Crisis Response and Management*. 2019.
- [168] S. G. Arapostathis. "Utilising Twitter for disaster management of fire events: steps towards efficient automation". In: *Arabian Journal of Geosciences* 14.8 (2021), pp. 1–16.
- [169] S. G. Arapostathis and M. Karantzia. "Mapping information of fire events, from VGI source (Twitter), for effective disaster management (in Greece); the fire of North-East Attica, August 2017,(Greece) case study". In: *Conference of the Arabian Journal of Geosciences*. Springer. 2018, pp. 257–260.
- [170] I. Ullah et al. "RweetMiner: Automatic identification and categorization of help requests on twitter during disasters". In: *Expert Systems with Applications* 176 (2021), p. 114787.
- [171] H. Zade et al. "From situational awareness to actionability: Towards improving the utility of social media data for crisis response". In: *Proceedings of the ACM on human-computer interaction* 2 (2018), pp. 1–18.
- [172] Y. Feng, X. Huang, and M. Sester. "Extraction and analysis of natural disaster-related VGI from social media: review, opportunities and challenges". In: *International Journal of Geographical Information Science* 36.7 (2022), pp. 1275–1316.
- [173] A. Bhoi et al. "Mining social media text for disaster resource management using a feature selection based on forest optimization". In: *Computers & Industrial Engineering* 169 (2022), p. 108280.
- [174] S. E. Middleton, L. Middleton, and S. Modafferi. "Real-time crisis mapping of natural disasters using social media". In: *IEEE Intelligent Systems* 29.2 (2013), pp. 9–17.
- [175] A. Alyaqout, T. E. Chow, and A. Savelyev. "Assessing The Quality of Water Depth Derived From Volunteered Geographic Information (VGI) For Flood Monitoring. A Case Study of Hurricane Harvey In Harris County, Texas". In: *ResearchSquare preprint* (2021).

- [176] X. Chen et al. “Implementing a real-time Twitter-based system for resource dispatch in disaster management”. In: *GeoJournal* 81 (2016), pp. 863–873.
- [177] G. Panteras et al. “Triangulating social multimedia content for event localization using Flickr and Twitter”. In: *Transactions in GIS* 19.5 (2015), pp. 694–715.
- [178] S. G. Arapostathis and M. Karantzia. “Mapping information of fire events, from VGI source (Twitter), for effective disaster management (in Greece); the fire of North-East Attica, August 2017,(Greece) case study”. In: *Advances in Remote Sensing and Geo Informatics Applications: Proceedings of the 1st Springer Conference of the Arabian Journal of Geosciences (CAJG-1)*. Springer. 2019, pp. 257–260.
- [179] G. Cervone et al. “Using Twitter for tasking remote-sensing data collection and damage assessment: 2013 Boulder flood case study”. In: *International Journal of Remote Sensing* 37.1 (2016), pp. 100–124.
- [180] B. Bischke et al. “Contextual enrichment of remote-sensed events with social media streams”. In: *Proceedings of the 24th ACM international conference on Multimedia*. 2016, pp. 1077–1081.
- [181] C. Boulton, H. Shotton, and H. Williams. “Using social media to detect and locate wildfires”. In: *Proceedings of the international AAAI conference on web and social media*. Vol. 10. 2. 2016, pp. 178–186.
- [182] H. Senaratne et al. “A review of volunteered geographic information quality assessment methods”. In: *International Journal of Geographical Information Science* 31.1 (2017), pp. 139–167.
- [183] R. J. Trudeau. *Introduction to graph theory, 2nd edition*. Dover Publications, Mineola, New York, 1993.
- [184] G. Boeing. “OSMnx: New methods for acquiring, constructing, analyzing, and visualizing complex street networks”. In: *Computers, Environment and Urban Systems* 65 (2017), pp. 126–139.
- [185] G. Boeing. “Street network models and measures for every US City, county, urbanized area, census tract, and zillow-defined neighborhood”. In: *Urban Science* 3.1 (2019), p. 28.
- [186] E. Allen et al. “Sensitivity analysis and uncertainty quantification of a seismic risk model for road networks”. In: *Computer-Aided Civil and Infrastructure Engineering* 37.4 (2022), pp. 516–530.
- [187] Y. Qiang and J. Xu. “Empirical assessment of road network resilience in natural hazards using crowdsourced traffic data”. In: *International Journal of Geographical Information Science* 34.12 (2020), pp. 2434–2450.
- [188] D. Middleton. “Meteorological data from numerical weather prediction or observations for dispersion modelling”. In: *International Journal of Environment and Pollution* 44 (2011), pp. 78–86.
- [189] M. M. Al-Kahlout et al. “Neural network approach to predict forest fires using meteorological data”. In: *International Journal of Academic Engineering Research (IJAER)* 4.9 (2020).
- [190] A. Galderisi et al. “From Global to Local and from Local to Global: Examples of Event Scenarios in Europe”. In: *Inside Risk: A Strategy for Sustainable Risk Mitigation*. Springer, 2011, pp. 245–285.

- [191] D. Deeter et al. *Best practices for road condition reporting systems: Synthesis report*. Tech. rep. United States. Federal Highway Administration, 2014.
- [192] J. J. Sharples et al. “Natural hazards in Australia: extreme bushfire”. In: *Climatic Change* 139.1 (2016), pp. 85–99.
- [193] F. Filippini. “Exploitation of sentinel-2 time series to map burned areas at the national level: A case study on the 2017 Italy wildfires”. In: *Remote Sensing* 11.6 (2019), p. 622.
- [194] S. Ghaffarian et al. “Post-disaster building database updating using automated deep learning: An integration of pre-disaster OpenStreetMap and multi-temporal satellite data”. In: *Remote Sensing* 11.20 (2019), p. 2427.
- [195] J. Guth et al. “Development of a generic concept to analyze the accessibility of emergency facilities in critical road infrastructure for disaster scenarios: exemplary application for the 2017 wildfires in Chile and Portugal”. In: *Natural Hazards* 97.3 (2019), pp. 979–999.
- [196] F. Guindos-Rojas et al. “Evaluation of a Bayesian algorithm to detect Burned Areas in the Canary Islands’ Dry Woodlands and forests ecoregion using MODIS data”. In: *Remote Sensing* 10.5 (2018), p. 789.
- [197] M. A. Crowley et al. “Multi-sensor, multi-scale, Bayesian data synthesis for mapping within-year wildfire progression”. In: *Remote Sensing Letters* 10.3 (2019), pp. 302–311.
- [198] N. Chiaraviglio et al. “Automatic fire perimeter determination using MODIS hotspots information”. In: *2016 IEEE 12th International Conference on e-Science (e-Science)*. IEEE, 2016, pp. 414–423.
- [199] A. A. Pereira et al. “Burned area mapping in the Brazilian Savanna using a one-class support vector machine trained by active fires”. In: *Remote Sensing* 9.11 (2017), p. 1161.
- [200] NASA. *MODIS specifications*. 2021. URL: <https://modis.gsfc.nasa.gov/about/specifications.php> (visited on 07/09/2021).
- [201] P. Oliva and W. Schroeder. “Assessment of VIIRS 375 m active fire detection product for direct burned area mapping”. In: *Remote Sensing of Environment* 160 (2015), pp. 144–155.
- [202] M. Buchhorn et al. “Copernicus Global Land Cover Layers—Collection 2”. In: *Remote Sensing* 12.6 (2020), p. 1044.
- [203] Q. Wu. “geemap: A Python package for interactive mapping with Google Earth Engine”. In: *Journal of Open Source Software* 5.51 (2020), p. 2305.
- [204] State of California. *CAL FIRE*. 2022. URL: <https://frap.fire.ca.gov/mapping/gis-data/> (visited on 01/13/2022).
- [205] D. Rashkovetsky et al. “Wildfire Detection from Multi-sensor Satellite Imagery Using Deep Semantic Segmentation”. In: *IEEE Journal of Selected Topics in Applied Earth Observations and Remote Sensing* (2021), pp. 7001–7016.
- [206] A. Bastarrika et al. “Mapping burned areas in Latin America from Landsat-8 with Google Earth Engine”. In: *Preprints.org* (2018).
- [207] B. Kurnaz, C. Bayik, and S. Abdikan. “Forest Fire Area Detection by Using Landsat-8 and Sentinel-2 Satellite Images: A Case Study in Mugla, Turkey”. In: *Research Square preprint* (2020).

- [208] T. Kattenborn et al. “Review on Convolutional Neural Networks (CNN) in vegetation remote sensing”. In: *ISPRS Journal of Photogrammetry and Remote Sensing* 173 (2021), pp. 24–49.
- [209] X.-Y. Liu, J. Wu, and Z.-H. Zhou. “Exploratory undersampling for class-imbalance learning”. In: *IEEE Transactions on Systems, Man, and Cybernetics, Part B (Cybernetics)* 39.2 (2008), pp. 539–550.
- [210] P. Geurts, D. Ernst, and L. Wehenkel. “Extremely randomized trees”. In: *Machine Learning* 63.1 (2006), pp. 3–42.
- [211] Y. Freund and R. E. Schapire. “A decision-theoretic generalization of on-line learning and an application to boosting”. In: *Journal of Computer and System Sciences* 55.1 (1997), pp. 119–139.
- [212] J. H. Friedman. “Greedy function approximation: a gradient boosting machine”. In: *Annals of Statistics* (2001), pp. 1189–1232.
- [213] G. E. Hinton. “Connectionist learning procedures”. In: *Machine Learning*. Elsevier, 1990, pp. 555–610.
- [214] F. M. Riese, S. Keller, and S. Hinz. “Supervised and semi-supervised self-organizing maps for regression and classification focusing on hyperspectral data”. In: *Remote Sensing* 12.1 (2020), p. 7.
- [215] F. M. Riese and S. Keller. “Supervised, Semi-Supervised, and Unsupervised Learning for Hyperspectral Regression”. In: *Hyperspectral Image Analysis*. Springer, 2020, pp. 187–232.
- [216] F. M. Riese and S. Keller. “Introducing a framework of self-organizing maps for regression of soil moisture with hyperspectral data”. In: *IGARSS 2018 IEEE International Geoscience and Remote Sensing Symposium*. IEEE. 2018, pp. 6151–6154.
- [217] T. Kohonen. “The self-organizing map”. In: *Proceedings of the IEEE* 78.9 (1990), pp. 1464–1480.
- [218] H.-C. Kim et al. “Support vector machine ensemble with bagging”. In: *International Workshop on Support Vector Machines*. Springer. 2002, pp. 397–408.
- [219] F. M. Riese and S. Keller. “Soil texture classification with 1D convolutional neural networks based on hyperspectral data”. In: *ISPRS Annals of the Photogrammetry, Remote Sensing and Spatial Information Sciences IV-2/W5.9* (2019), pp. 615–621.
- [220] M. C. Hansen et al. “Global land cover classification at 1 km spatial resolution using a classification tree approach”. In: *International Journal of Remote Sensing* 21.6-7 (2000), pp. 1331–1364.
- [221] A. Brand and A. Manandhar. “Semantic Segmentation of Burned Areas in Satellite Images Using a U-Net Convolutional Neural Network”. In: *ISPRS-International Archives of the Photogrammetry, Remote Sensing and Spatial Information Sciences* 43 (2021), pp. 47–53.
- [222] F. M. Riese. *SuSi: Supervised Self-Organizing Maps in Python*. 2019. URL: <https://doi.org/10.5281/zenodo.2609130> (visited on 12/06/2023).
- [223] F. Pedregosa et al. “Scikit-learn: Machine Learning in Python”. In: *Journal of Machine Learning Research* 12 (2011), pp. 2825–2830.
- [224] F. Rosenblatt. “The perceptron: a probabilistic model for information storage and organization in the brain.” In: *Psychological Review* 65.6 (1958), p. 386.

- [225] L. Liu, M. Ji, and M. Buchroithner. “Transfer learning for soil spectroscopy based on convolutional neural networks and its application in soil clay content mapping using hyperspectral imagery”. In: *Sensors* 18.9 (2018), p. 3169.
- [226] W. Hu et al. “Deep convolutional neural networks for hyperspectral image classification”. In: *Journal of Sensors* 2015 (2015), pp. 1–12.
- [227] L. Li et al. “Hyperband: A novel bandit-based approach to hyperparameter optimization”. In: *The Journal of Machine Learning Research* 18.1 (2017), pp. 6765–6816.
- [228] A. Koltunov et al. “The development and first validation of the GOES Early Fire Detection (GOES-EFD) algorithm”. In: *Remote Sensing of Environment* 184 (2016), pp. 436–453.
- [229] R. Ramo and E. Chuvieco. “Developing a random forest algorithm for MODIS global burned area classification”. In: *Remote Sensing* 9.11 (2017), p. 1193.
- [230] NOAA National Centers for Environmental Information (NCEI). *U.S. Billion-Dollar Weather and Climate Disasters*. 2022. URL: <https://www.ncei.noaa.gov/access/monitoring/billions/> (visited on 05/09/2022).
- [231] A. M. Forati and R. Ghose. “Examining Community Vulnerabilities through multi-scale geospatial analysis of social media activity during Hurricane Irma”. In: *International Journal of Disaster Risk Reduction* 68 (2022), p. 102701.
- [232] R. Arthur and H. T. Williams. “Scaling laws in geo-located Twitter data”. In: *PloS one* 14.7 (2019), e0218454.
- [233] ESRI. *ArcGIS Pro*. Version 2.6.1. 2022. URL: <https://www.esri.com/en-us/arcgis/products/arcgis-pro/overview> (visited on 03/19/2022).
- [234] R. Gallardo. *Digital Divide Index*. 2020. URL: <http://pcrd.purdue.edu/ddi> (visited on 03/21/2022).
- [235] Y. Jiang, Z. Li, and X. Ye. “Understanding demographic and socioeconomic biases of geotagged Twitter users at the county level”. In: *Cartography and Geographic Information Science* 46.3 (2019), pp. 228–242.
- [236] worldpop.org. *Worldpop*. 2022. URL: <https://www.worldpop.org> (visited on 03/21/2022).
- [237] R. Hijmans. *DIVA-GIS*. 2022. URL: <https://www.diva-gis.org> (visited on 03/21/2022).
- [238] K. R. Knapp et al. “The international best track archive for climate stewardship (IBTrACS) unifying tropical cyclone data”. In: *Bulletin of the American Meteorological Society* 91.3 (2010), pp. 363–376.
- [239] National Hurricane Center. *Tropical Cyclone Advisory Archive*. 2022. URL: <https://www.nhc.noaa.gov/data/#advisories> (visited on 03/31/2022).
- [240] A. Agarwal and D. Toshniwal. “Face off: Travel habits, road conditions and traffic city characteristics bared using twitter”. In: *IEEE Access* 7 (2019), pp. 66536–66552.
- [241] M. N. Y. Utomo, T. B. Adji, and I. Ardiyanto. “Geolocation prediction in social media data using text analysis: A review”. In: *2018 International Conference on Information and Communications Technology (ICOIACT)*. IEEE. 2018, pp. 84–89.
- [242] N. J. F. Martínez and C. Perrián-Pascual. “Knowledge-based rules for the extraction of complex, fine-grained locative references from tweets”. In: *RAEL: revista electrónica de lingüística aplicada* 19.1 (2020), pp. 136–163.

- [243] Explosion.ai. *spaCy - Industrial-Strength Natural Language Processing*. 2023. URL: <https://spacy.io/> (visited on 11/15/2023).
- [244] C. Brunson, A. S. Fotheringham, and M. E. Charlton. “Geographically weighted regression: a method for exploring spatial nonstationarity”. In: *Geographical Analysis* 28.4 (1996), pp. 281–298.
- [245] J. P. Cangialosi. *National Hurricane Center Forecast pdfs report: 2017 hurricane season*. 2017. URL: https://www.nhc.noaa.gov/pdfs/pdfs/pdfs_2017.pdf (visited on 08/17/2022).
- [246] M. Bilskie et al. “Real-time simulated storm surge predictions during Hurricane Michael (2018)”. In: *Weather and Forecasting* 37.7 (2022), pp. 1085–1102.
- [247] European Centre For Medium-Range Weather Forecasts. *IFS Documentation*. 2021. URL: <https://www.ecmwf.int/en/eLibrary/20195-ifs-documentation-cy47r3-part-i-observations> (visited on 03/18/2022).
- [248] G. E. Birchfield. “Numerical prediction of hurricane movement with the use of a fine grid”. In: *Journal of Atmospheric Sciences* 17.4 (1960), pp. 406–414.
- [249] K. R. Knapp et al. *International best track archive for climate stewardship (IBTrACS) project, version 4*. Tech. rep. NOAA National Centers for Environmental Information, 2018.
- [250] S. Kim et al. “Deep-hurricane-tracker: Tracking and forecasting extreme climate events”. In: *2019 IEEE Winter Conference on Applications of Computer Vision (WACV)*. IEEE. 2019, pp. 1761–1769.
- [251] J. Unger. “Analysis of Hurricane Track Forecast Accuracy During the 2018 Season”. PhD thesis. The University of Tennessee, Knoxville, 2019.
- [252] R. S. Lee and J. N. Liu. “Tropical cyclone identification and tracking system using integrated neural oscillatory elastic graph matching and hybrid RBF network track mining techniques”. In: *IEEE Transactions on Neural Networks* 11.3 (2000), pp. 680–689.
- [253] A. C. Chawan, V. K. Kakade, and J. K. Jadhav. “Automatic detection of flood using remote sensing images”. In: *Journal of Information Technology* 2.01 (2020), pp. 11–26.
- [254] M. Izbicki, V. Papalexakis, and V. Tsotras. “Geolocating Tweets in any Language at any Location”. In: *Proceedings of the 28th ACM International Conference on Information and Knowledge Management*. 2019, pp. 89–98.
- [255] X. Hu et al. “GazPNE2: A general place name extractor for microblogs fusing gazetteers and pretrained transformer models”. In: *IEEE Internet of Things Journal* 9.17 (2022), pp. 16259–16271.
- [256] A. Panasyuk, E. S.-L. Yu, and K. G. Mehrotra. “Improving geocoding for city-level locations”. In: *2019 IEEE 13th International Conference on Semantic Computing (ICSC)*. IEEE. 2019, pp. 416–421.
- [257] W. Zhang and J. Gelernter. “Geocoding location expressions in Twitter messages: A preference learning method”. In: *Journal of Spatial Information Science* 9 (2014), pp. 37–70.
- [258] Y. Gu, Z. S. Qian, and F. Chen. “From Twitter to detector: Real-time traffic incident detection using social media data”. In: *Transportation Research Part C: Emerging Technologies* 67 (2016), pp. 321–342.

- [259] J. Zhang, A. DeLucia, and M. Dredze. “Changes in Tweet Geolocation over Time: A Study with Carmen 2.0”. In: *Proceedings of the Eighth Workshop on Noisy User-generated Text (W-NUT 2022)*. 2022, pp. 1–14.
- [260] S. Milusheva et al. “Applying machine learning and geolocation techniques to social media data (Twitter) to develop a resource for urban planning”. In: *PloS one* 16.2 (2021), p. 80.
- [261] M. Zia et al. “SocialMedia2Traffic: Derivation of Traffic Information from Social Media Data”. In: *ISPRS International Journal of Geo-Information* 11.9 (2022), p. 482.
- [262] P. K. Putra, R. Mahendra, and I. Budi. “Traffic and road conditions monitoring system using extracted information from Twitter”. In: *Journal of Big Data* 9.1 (2022), p. 65.
- [263] T. Sakaki et al. “Real-time event extraction for driving information from social sensors”. In: *2012 IEEE International Conference on Cyber Technology in Automation, Control, and Intelligent Systems (CYBER)*. IEEE. 2012, pp. 221–226.
- [264] A. D. Ünsal. “Detection and description of traffic events using floating car and social media data”. PhD thesis. Middle East Technical University, 2022.
- [265] S. Vallejos et al. “Mining social networks to detect traffic incidents”. In: *Information Systems Frontiers* 23.1 (2021), pp. 115–134.
- [266] P. Bruneau et al. “Measuring the Impact of Natural Hazards with Citizen Science: The Case of Flooded Area Estimation Using Twitter”. In: *Remote Sensing* 13.6 (2021), p. 1153.
- [267] N. H. Di Cara et al. “Methodologies for monitoring mental health on Twitter: systematic review”. In: *Journal of Medical Internet Research* 25 (2023), e42734.
- [268] K. Müller and C. Schwarz. “From hashtag to hate crime: Twitter and antiminority sentiment”. In: *American Economic Journal: Applied Economics* 15.3 (2023), pp. 270–312.
- [269] W. Yu et al. “Road network generalization considering traffic flow patterns”. In: *International Journal of Geographical Information Science* 34.1 (2020), pp. 119–149.
- [270] A. Chen et al. “Capacity reliability of a road network: an assessment methodology and numerical results”. In: *Transportation Research Part B: Methodological* 36.3 (2002), pp. 225–252.
- [271] Z. Liu et al. “Exploring the resilience assessment framework of urban road network for sustainable cities”. In: *Physica A: Statistical Mechanics and its Applications* 586 (2022), p. 126465.
- [272] S. Ientile et al. “Measuring road network resilience by loss of serviceability index for critical road links”. In: *Proceedings of the Institution of Civil Engineers-Bridge Engineering*. Vol. 175. 3. 2022, pp. 160–171.
- [273] A. A. H. Redzuan et al. “Road Network Vulnerability Based on Diversion Routes to Reconnect Disrupted Road Segments”. In: *Sustainability* 14.4 (2022), p. 2244.
- [274] K. Rebello et al. “Testing a criticality framework for road networks in Auckland, New Zealand”. In: *International Journal of Disaster Resilience in the Built Environment* (2019), pp. 36–51.
- [275] S. Gibbons et al. “New road infrastructure: the effects on firms”. In: *Journal of Urban Economics* 110 (2019), pp. 35–50.

- [276] J. D. Glover and S. K. Tennant. *Remote areas statistical geography in Australia: notes on the Accessibility/Remoteness Index for Australia (ARIA+ version)*. Public Health Information Development Unit, The University of Adelaide, 2003.
- [277] S. Dong et al. “Characterizing resilience of flood-disrupted dynamic transportation network through the lens of link reliability and stability”. In: *Reliability Engineering & System Safety* 232 (2023), p. 109071.
- [278] Y. Liao. “Feasibility of estimating travel demand using geolocations of social media data”. In: *Transportation* 49 (2021), pp. 137–161.
- [279] S. Ghader. “A copula-based continuous cross-nested logit model for tour scheduling in activity-based travel demand models”. In: *Transportation Research Part B: Methodological* 145 (2021), pp. 324–341.
- [280] R. Kondo, Y. Shiomi, and N. Uno. “Network evaluation based on connectivity reliability and accessibility”. In: *Network Reliability in Practice: Selected Papers from the Fourth International Symposium on Transportation Network Reliability*. Springer. 2011, pp. 131–149.
- [281] C. B. Daniel, S. Saravanan, and S. Mathew. “Gis based road connectivity evaluation using graph theory”. In: *Transportation Research: Proceedings of CTRG 2017*. Springer. 2020, pp. 213–226.
- [282] A. Erath, M. Löchl, and K. W. Axhausen. “Graph-theoretical analysis of the Swiss road and railway networks over time”. In: *Networks and Spatial Economics* 9 (2009), pp. 379–400.
- [283] K. Park and A. Yilmaz. “A social network analysis approach to analyze road networks”. In: *ASPRS Annual Conference*. 2010, pp. 1–6.
- [284] C. Kanyou, E. Kouokam, and Y. Emvudu. “Structural network analysis: Correlation between centrality measures”. In: *Revue Africaine de la Recherche en Informatique et Mathématiques Appliquées* (2022), pp. 1–8.
- [285] A. Antunes, A. Seco, and N. Pinto. “An accessibility–maximization approach to road network planning”. In: *Computer-Aided Civil and Infrastructure Engineering* 18.3 (2003), pp. 224–240.
- [286] B. F. Santos, A. P. Antunes, and E. J. Miller. “Interurban road network planning model with accessibility and robustness objectives”. In: *Transportation Planning and Technology* 33.3 (2010), pp. 297–313.
- [287] A. Chen et al. “Network-based accessibility measures for vulnerability analysis of degradable transportation networks”. In: *Networks and Spatial Economics* 7 (2007), pp. 241–256.
- [288] E. W. Dijkstra. “A note on two problems in connexion with graphs”. In: *Edsger Wybe Dijkstra: His Life, Work, and Legacy*. 2022, pp. 287–290.
- [289] X. Li, J. Zhou, and W. Pedrycz. “Linking granular computing, big data and decision making: a case study in urban path planning”. In: *Soft Computing* 24 (2020), pp. 7435–7450.
- [290] R. Bader et al. “Alternative route graphs in road networks”. In: *Theory and Practice of Algorithms in (Computer) Systems: First International ICST Conference, TAPAS 2011, Proceedings*. Springer. 2011, pp. 21–32.

- [291] L. Li et al. “Comparing alternative route planning techniques: A comparative user study on Melbourne, Dhaka and Copenhagen road networks”. In: *IEEE Transactions on Knowledge and Data Engineering* 34.11 (2021), pp. 5552–5557.
- [292] T. Chondrogiannis et al. “Finding k-shortest paths with limited overlap”. In: *The VLDB Journal* 29.5 (2020), pp. 1023–1047.
- [293] D. R. White and S. P. Borgatti. “Betweenness centrality measures for directed graphs”. In: *Social Networks* 16.4 (1994), pp. 335–346.
- [294] L. C. Freeman. “A set of measures of centrality based on betweenness”. In: *Sociometry* (1977), pp. 35–41.
- [295] U. Brandes. “A faster algorithm for betweenness centrality”. In: *Journal of Mathematical Sociology* 25.2 (2001), pp. 163–177.
- [296] L. C. Freeman et al. “Centrality in social networks: Conceptual clarification”. In: *Social Networks* 1 (2002), pp. 238–263.
- [297] D. Li, Y. Tang, and Q. Chen. “Multi-Mode Traffic Demand Analysis Based on Multi-Source Transportation Data”. In: *IEEE Access* 8 (2020), pp. 65005–65019.
- [298] M. Moradi, S. Roche, and M. Mostafavi. “Exploring five indicators for the quality of OpenStreetMap road networks: a case study of Québec, Canada”. In: *Geomatica* (2022).
- [299] M. Brovelli, M. Minghini, and M. Molinari. “An Automated Grass-Based Procedure to Assess the Geometrical Accuracy of the Openstreetmap Paris Road Network”. In: *ISPRS - International Archives of the Photogrammetry, Remote Sensing and Spatial Information Sciences* (2016), pp. 919–925.
- [300] V. Knoop, H. van Zuylen, and S. Hoogendoorn. “The influence of spillback modelling when assessing consequences of blockings in a road network”. In: *European Journal of Transport and Infrastructure Research* 8.4 (2008), pp. 287–300.
- [301] M. Du, X. Jiang, and A. Chen. “Identifying critical links using network capacity-based indicator in multi-modal transportation networks”. In: *Transportmetrica B: Transport Dynamics* 10.1 (2022), pp. 1126–1150.
- [302] L. Vespaziani. *Best Practices in Wildfire Mass Evacuation Planning*. University of British Columbia, Graduating Project. 2019.
- [303] District of Squamish and Resort Municipality of Whistler. *Sea to Sky Evacuation Plan*. 2019. URL: <https://www.whistler.ca/services/emergency/evacuating-whistler/sea-sky-evacuation-plan/> (visited on 09/07/2023).
- [304] J. Florath, J. Chanussot, and S. Keller. “Investigation of Volunteered Geographic Information Data for Near-Real-Time Spatial Analysis of Fire Hazards”. 9th International Conference on Geographical Information Systems Theory, Applications and Management GISTAM. 2023. URL: <https://gistam.scitevents.org/Abstract.aspx?idEvent=/y0hGuPKvGA=>.
- [305] J. Li, J. Li, and K. Yao. “Inundation analysis of reservoir flood based on computer aided design (CAD) and digital elevation model (DEM)”. In: *Water* 10.4 (2018), p. 530.
- [306] D. Tian. “Mapping, Modeling, and Predicting Extreme Flood Events with Cloud Computing”. PhD thesis. Louisiana State University and Agricultural and Mechanical College, 2023.

- [307] Y. Xiao, B. Li, and Z. Gong. “Real-time identification of urban rainstorm waterlogging disasters based on Weibo big data”. In: *Natural Hazards* 94.2 (2018), pp. 833–842.
- [308] M. Abadi et al. “Tensorflow: A system for large-scale machine learning”. In: *12th symposium on operating systems design and implementation*. 2016, pp. 265–283.

List of Figures

1.1	Structure of this thesis.	5
2.1	Overview of the advantages (+) and disadvantages (-) of Volunteered Geographic Information (VGI) data and remote sensing (RS) data by relevant aspects for spatial analysis of natural hazards.	10
2.2	Overview of cases study hazard locations in this thesis.	22
3.1	Visualization of Module I, the natural hazard impact determination with geoinformation data.	24
3.2	Visualization of the combined classification framework of fires and burned areas. Reprinted from [14].	28
3.3	Overview of fire cases study hazard locations. Adapted from [14].	29
3.4	Visualization of Steps 1 to 4 of the reference generation. Reprinted from [14].	30
3.5	Flow diagram summarizing the dataset preparation with the ML process example illustrated for Uset 1. Reprinted from [14].	34
3.6	Flowchart of the one-dimensional (1D) Convolutional Neural Network (CNN) architecture. Adapted from [14].	36
3.7	Exemplary feature importances for Extremely Randomized Tree (ET) (top) and Gradient Boosting (GradientBoost) (bottom). Reprinted from [14]. . . .	38
3.8	Visualization of the classification results of the Extremely Randomized Tree (ET) and the one-dimensional Convolutional Neural Network (1D-CNN). Reprinted from [14].	39
3.9	Visualization of the framework for natural hazard impact zone estimation from Volunteered Geographic Information (VGI) for <i>stationary</i> hazards, representatively for wildfire scenarios.	44
3.10	Visualization of the regression framework for natural hazard impact zone estimation from Volunteered Geographic Information (VGI) for <i>moving</i> hazards, representatively for tropical cyclone (TC) scenarios. Adapted from [44]. . .	45
3.11	Overview of cases study hazard locations and respective hazard types	48
3.12	Methodology overview for approximating fire-affected areas based on Twitter data. Reprinted from [43].	51
3.13	Exemplary tweet text snippets from which information about approximate areal locations of natural hazards can be extracted. Reprinted from [43]. . .	53
3.14	Methodology overview for approximating tropical cyclone (TC)-affected areas based on Twitter data.	56

3.15	Visualization of the fire impact zone estimation using Volunteered Geographic Information (VGI). Reprinted from [43].	59
3.16	Visualization of the estimated distances of test datapoints to the tropical cyclone tracks. Adapted from [44].	62
3.17	Overview of the cases study hazard location for the San Francisco Bay Area (IX) flood.	69
3.18	Visualization of the impacted road extraction framework during natural hazards from Twitter data. Reprinted from [1].	71
3.19	Visualization of extracted impacted roads from Volunteered Geographic Information (VGI) text information data for the flood in the San Francisco Bay Area (IX) . Reprinted from [1].	73
3.20	Visualization of the synthesis of Module I, the natural hazard impact determination with geoinformation data.	75
4.1	Visualization of Module II, the road network accessibility assessment during natural hazards using input from Module I.	78
4.2	Overview of the cases study hazard location for the Oakland (X) flood.	80
4.3	Visualization of the impact zone, direct impacts on the road network and degraded roads for the Oakland (X) flood application scenario. Adapted from [1].	86
4.4	Visualization of the results of betweenness centrality (BN), closeness centrality (CN), Shelter Accessibility Index (SAI), and Alternative Routing Assumption Accessibility (ARAA) for the flood in Oakland . Reprinted from [1].	88
4.5	Visualization of the synthesis of Module II for the road network accessibility assessment during natural hazards.	95
5.1	Overview of the cases study hazard location for the Bobcat (XI) fire.	98
5.2	Visualization of the results of the hazard impact extraction (burned area and fire area) from remote sensing data for the selected natural hazard, the Bobcat wildfire (XI). Adapted from [43].	100
5.3	Visualization of the results of the hazard impact extraction from Volunteered Geographic Information (VGI) data for the selected natural hazard, the Bobcat wildfire (XI). Adapted from [43].	101
5.4	Visualization of degraded roads extracted from Volunteered Geographic Information (VGI) text information for the Bobcat fire (XI). Adapted from [1].	102
5.5	Visualization of the impact zone, direct impacts on the road network and degraded roads for the Bobcat wildfire application scenario (XI). Adapted from [1].	104
5.6	Visualization of the results of betweenness centrality (BN), closeness centrality (CN), Shelter Accessibility Index (SAI), and Alternative Routing Assumption Accessibility (ARAA) for the Bobcat wildfire (XI). Reprinted from [1].	106

A.1	Normalized confusion matrices for the applied ML models for fire area estimation using remote sensing data. Reprinted from [14].	150
A.2	Visualization of the Shelter Accessibility Index (SAI) measure for the flood in Oakland for network nodes and edges.	152

List of Tables

2.1	Overview of the related work concerning natural hazard investigations with satellite remote sensing (RS) sensors.	13
2.2	Overview of the related work concerning the use of Volunteered Geographic Information (VGI) and Twitter data during natural hazard scenarios.	17
2.3	Overview of the related work concerning the use of Volunteered Geographic Information (VGI) data in combination with remote sensing (RS) data during natural hazard scenarios.	18
3.1	Classification metrics in % of all machine learning (ML) models trained on the Uset 3. Reprinted from [14].	37
3.2	Classification results of the four selected models on different training and test data subsets. Reprinted from [14].	38
3.3	Classification metrics of Extremely Randomized Tree (ET) and the one-dimensional Convolutional Neural Network (1D-CNN) for comparison on the independent regional dataset of central Spain (III) in %. Reprinted from [14].	39
3.4	Overview of fire characteristics and characteristics influencing VGI data regarding the three scenario areas for fire impact estimation. Adapted from [1].	47
3.5	Overview of numbers (#) of extracted tweet data for <i>stationary</i> and <i>moving</i> hazards.	49
3.6	Supplementary data with their sources and years of creation. Reprinted from [44].	50
3.7	Deviances in km for the wildfire hazard approximation methods	60
3.8	Regression metrics in of all tropical cyclone approximation estimation models predicted on the test dataset and compared to the reference data. Adapted from [44].	61
4.1	Overview of network analysis data for the Oakland (X) flood. Adapted from [1].	81
4.2	Advantages and disadvantages of different accessibility measures. Reprinted from [1].	91
5.1	Overview of fire characteristics and characteristics influencing tweet data for the Bobcat Fire. Adapted from [1].	99
5.2	Overview of network analysis data for the Bobcat wildfire (XI). Adapted from [1].	103

A.1	Hyperparameter setup for the classification approaches for fire area estimation using remote sensing data. Reprinted from [14].	149
A.2	Hyperparameter setup for the Machine Learning models for the tropical cyclone track estimation. Adapted from [44].	151
A.3	Evaluation metrics for regression approaches for the tropical cyclone track estimation.	151

List of Abbreviations

R^2 Coefficient of Determination

1D one-dimensional

AA Average Accuracy

ABI Advanced Baseline Imager

ANN Artificial Neural Network

API Application Programming Interface

ARAA Alternative Routing Assumption Accessibility

ARIA Accessibility and Remoteness Index of Australia

ASTER Advanced Spaceborne Thermal Emission and Reflection Radiometer

AVHRR Advanced Very High Resolution Radiometer

BA Balanced Accuracy

BN Betweenness Centrality

BS baseline

CA California

CN Closeness Centrality

CNN Convolutional Neural Network

DDI Digital Divide Index

EFAI Emergency Facility Accessibility Index

EO Earth Observing

ERS European Remote Sensing Satellite

ET Extremely Randomized Tree

FY FengYun

GADM Global Administrative Areas Database

GCOM Global Change Observation Mission

GFDS Global Flood Detection System

GFM Global Flood Monitoring

GIS Geographic Information System

GOES Geostationary Operational Environmental Satellite

GPS Global Positioning System

GRACE Gravity Recovery And Climate Experiment

GradientBoost Gradient Boosting

GWR Geographically Weighted Regression

InSAR Interferometric Synthetic Aperture Radar

IRS Indian Remote Sensing

LVA Location by Viewing Angle

MAE Mean Absolute Error

ME Maximum Error

MetOp Meteorological Operational Satellite

MIVIS Multispectral Infrared and Visible Imaging Spectrometer

ML Machine Learning

MLP Multi-Layer Perceptron

MODIS Moderate-resolution Imaging Spectroradiometer

NER Named Entity Recognition

NHC National Hurricane Center

NIR Near InfraRed

NLP Natural Language Processing

NOAA National Oceanic and Atmospheric Administration

NPP National Polar-orbiting Partnership

OA Overall Accuracy

OSM Open Street Map

RegEx Regular Expressions

RMSE Root Mean Squared Error

RS Remote Sensing

RSAT2 RADARSAT-2

S Sentinel

SAI Shelter Accessibility Index

SAR Synthetic Aperture Radar

SE south-east

SEVIRI Spinning Enhanced Visible and InfraRed Imager

SMD Social Media Data

SMMR Scanning Multichannel Microwave Radiometer

SOM Self-Organizing Map

SPOT Satellite Pour l'Observation de la Terre

SRTM Shuttle Radar Topography Mission

SVM Support Vector Machines

SWIR Short-Wavelength InfraRed

TC tropical cyclone

TCPA Tropical Cyclone Public Advisories

TN temporal-non-stationary

TRMM Tropical Rainfall Measuring Mission

US United States of America

UTM Universal Transverse Mercator

VGI Volunteered Geographic Information

VIIRS Visible Infrared Imaging Radiometer Suite

WGS84 World Geodetic System 1984

A Supplementary Material of Natural Hazard Impact Zone Estimation with Remote Sensing Data

A.1 Hyperparameters

Table A.1.: Hyperparameter setup for the classification approaches. The approaches are implemented mostly in `scikit-learn` [223] and `TensorFlow` [308], while the SOM is implemented according to Riese et al. [215]. The following abbreviations are used: ET - Extremely Randomized Tree; GradientBoost - Gradient Boosting; MLP - Multi-Layer Perceptron; SOM - Self-Organizing Map; SVM - Support Vector Machines; 1D-CNN - one-dimensional Convolutional Neural Network. Reprinted from [14].

Model	Package	Hyperparameter setup
ET [210]	<code>scikit-learn</code>	<code>n_estimators = 200; max_depth = 100</code>
AdaBoost [211]	<code>scikit-learn</code>	<code>n_estimators = 100; learning_rate = 1.0</code>
GradientBoost [212]	<code>scikit-learn</code>	<code>learning_rate = 0.1; loss = "deviance"; n_estimators = 100; max_depth = 3</code>
MLP [213]	<code>scikit-learn</code>	<code>hidden_layer_sizes = (5, 2); solver = "adam"; activation = "relu"</code>
BaggingSVM [218]	<code>scikit-learn</code>	<code>base_estimator = "SVC"; C = 0.7; gamma = "auto"</code>
SOM [217, 216, 215]	other	SOM size = 100×100 ; $N_{It, Input} = 1000$; learning rates $\alpha_{start} = 0.1$
1D-CNN [219]	<code>TensorFlow</code>	Keras sequential model: <code>epochs = 80;</code> <code>batch_size = 50;</code> 2 convolutional layers <code>{64, 32}</code> ; 1 dense layer 100 neurons; <code>activation = "relu"</code>

A.2 Confusion Matrices

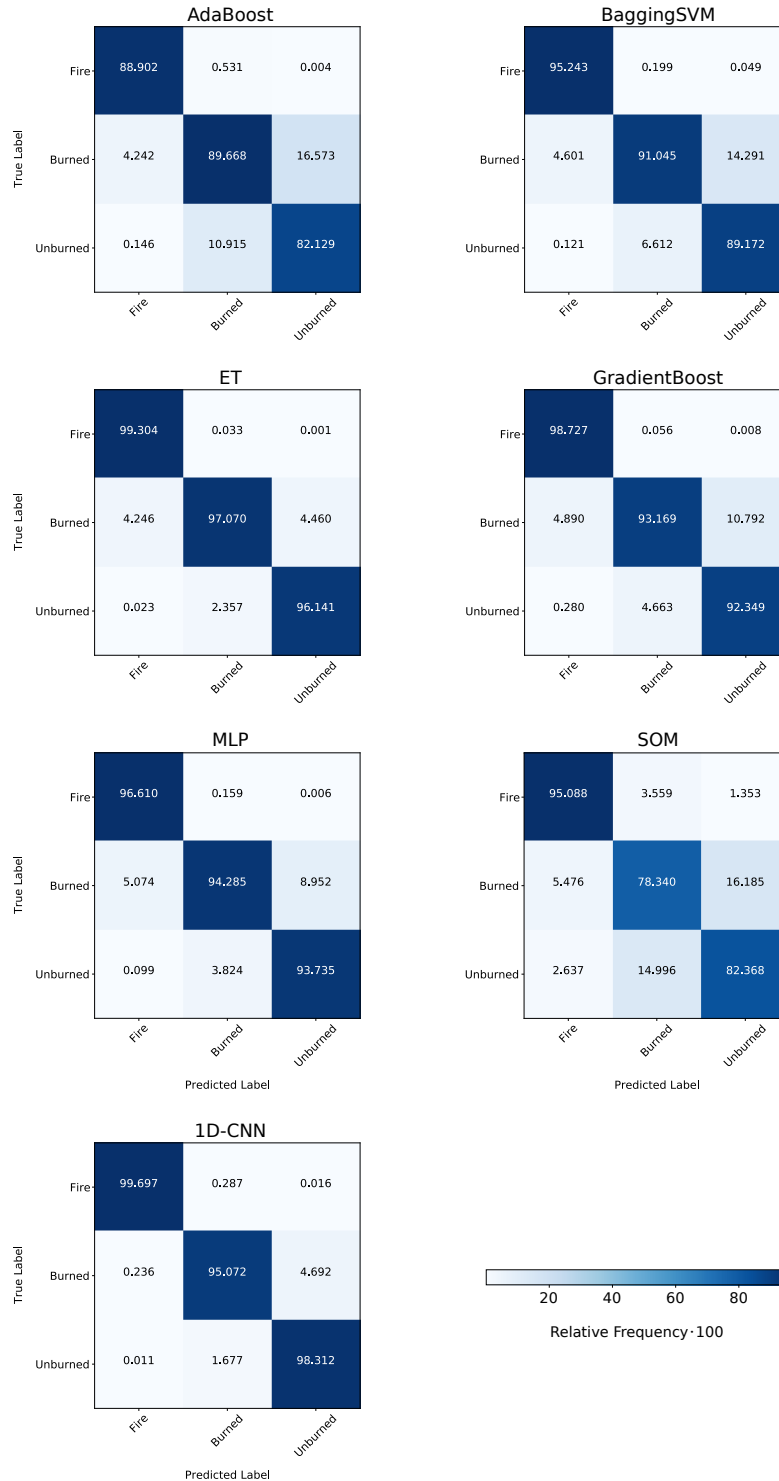


Figure A.1.: Normalized confusion matrices for the applied ML models. The prediction is performed on Subset 2 and compared to the reference data. The ML models have been trained on Uset 3. The following abbreviations are used: ET - Extremely Randomized Tree; GradientBoost - Gradient Boosting; MLP - Multi-Layer Perceptron; SOM - Self-Organizing Map; SVM - Support Vector Machines; 1D-CNN - one-dimensional Convolutional Neural Network. Reprinted from [14].

B Supplementary Material of Natural Hazard Impact Zone Estimation with Volunteered Geographic Information Data - Moving Hazards

B.1 Hyperparameters

Table A.2.: Hyperparameter setup for the ML models. The models are implemented in `scikit-learn` [223] and ArcGIS. The following abbreviations are used: BS - baseline; ET - Extremely Randomized Tree; GWR - Geographically Weighted Regression; TN - temporally non-stationary. Adapted from [44].

Model	Split	Package	Hyperparameter setup
ET [210]	BS	scikit-learn	<code>n_estimators = 100;max_depth = 12;</code> <code>min_samples_leaf = 1;min_samples_split = 2</code>
GWR [244]	BS	ArcGIS	<code>number_of_neighbours = 30</code>
ET [210]	TN	scikit-learn	<code>n_estimators = 5;max_depth = 5;</code> <code>min_samples_leaf = 1;min_samples_split = 6</code>

B.2 Evaluation Metrics

Table A.3.: Evaluation metrics for regression approaches. i represents a respective datapoint, y_i is the true label and \hat{y}_i is the estimated label of the i -th datapoint. \bar{y} is the mean of the observed data and n is the number of estimated datapoints. (R^2 : coefficient of determination, RMSE: root mean squared error, MAE: mean absolute error, ME: maximum error).

Metric	Formula	Description
R^2	$R^2 = 1 - \frac{\sum(y_i - \hat{y}_i)^2}{\sum(y_i - \bar{y})^2}$	Represents the proportion of variance that has been explained by the independent variables in the model.
RMSE	$RMSE = \sqrt{\frac{\sum(\hat{y}_i - y_i)^2}{n}}$	The square root of the mean squared error (MSE) measures in the same units as the response variable, in contrast to the MSE.
MAE	$MAE = \frac{\sum y_i - \hat{y}_i }{n}$	The average of the absolute differences between the predicted values and the actual values in a dataset.
ME	$ME = \text{Max}(y_i - \hat{y}_i)$	It is the worst case error between the predicted values and the actual values in a dataset.

C Supplementary Material of Network Accessibility Assessment during Natural Hazards

C.1 Result Presentation Rationale

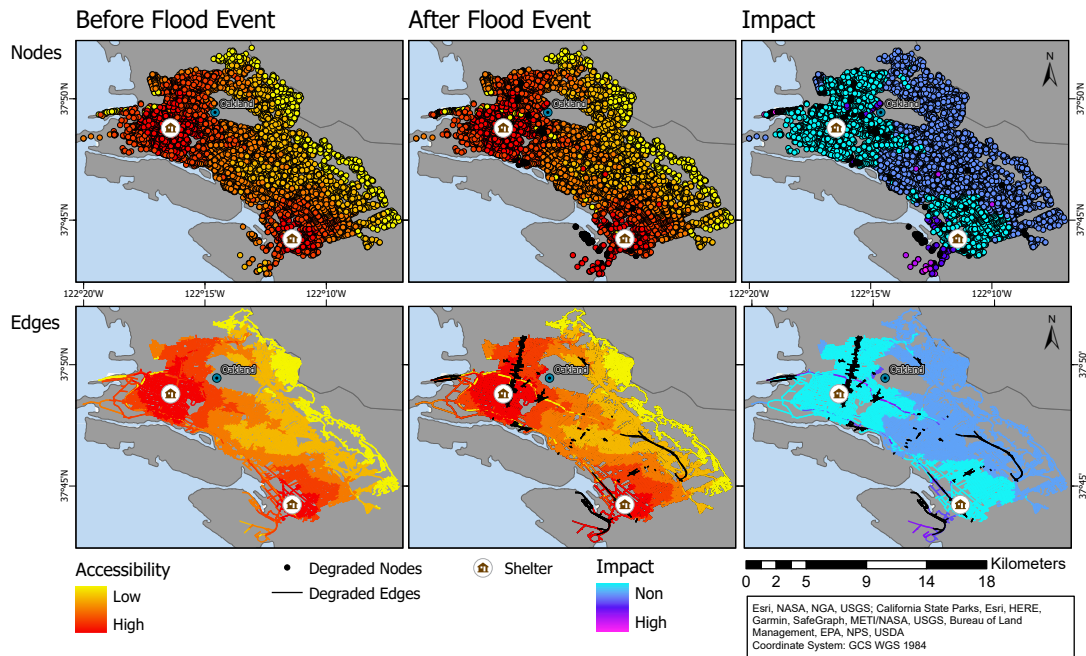


Figure A.2.: Visualization of the Shelter Accessibility Index (SAI) measure for the flood in **Oakland** displayed for the intact network before the hazard, the degraded network during/after the hazard and the change in accessibility between the two for the network nodes (row 1) and the network edges (row 2), respectively. Data basis: © 2018 GADM. Projection: WGS84.

Colophon

This thesis was typeset with \LaTeX 2 ϵ . It uses the *Clean Thesis* style developed by Ricardo Langner. The design of the *Clean Thesis* style is inspired by user guide documents from Apple Inc.

Download the *Clean Thesis* style at <http://cleanthesis.der-ric.de/>.